Theses and Dissertations

Fall 2009

Experimental investigation of free dendritic growth of succinonitrile-acetone alloys

Antonio Jose Melendez Ramirez
University of Iowa

Recommended Citation

EXPERIMENTAL INVESTIGATION OF FREE DENDRITIC GROWTH OF

SUCCINONITRILE-ACETONE ALLOYS

by

Antonio Jose Melendez Ramirez

An Abstract

Of a thesis submitted in partial fulfillment
of the requirements for the Doctor of
Philosophy degree in Mechanical Engineering
in the Graduate College of
The University of Iowa

December 2009

Thesis Supervisor: Professor Christoph Beckermann

ABSTRACT

Measurements are carried out for dendrite tip growth of succinonitrile-acetone alloys solidifying freely in an undercooled melt. The current experimental investigation is conducted using the equiaxed dendritic solidification experiment (EDSE). This setup allows for precise measurements of the dendrite tip velocity, radius and shape for a range of undercoolings and solute concentrations. The collected data are compared to available theories of free dendritic growth, such as the Lipton-Glicksman-Kurz and Li-Beckermann models. It is found that for dilute succinonitrile-acetone alloys, the measured dendrite tip Péclet numbers agree well with previous theories of free dendritic growth, if the effects of melt convection are taken into account. The tip selection parameter deviates significantly from the pure succinonitrile value and is inversely related to the applied undercooling. Besides, the selection parameter shows no dependence on the solute concentration. These results are consistent with phase-field simulations and preceding experimental investigations. In addition, scaling relationships for the sidebranching shape were obtained in terms of the dendritic envelope, projection area and contour length. These new scaling relations agree well with previous measurements in pure succinonitrile dendrites by Li and Beckermann

Abstract Approved: _____

                    Thesis Supervisor

                    _____

                    Title and Department

                    _____

                    Date

EXPERIMENTAL INVESTIGATION OF FREE DENDRITIC GROWTH OF

SUCCINONITRILE-ACETONE ALLOYS

by

Antonio Jose Melendez Ramirez

A thesis submitted in partial fulfillment
of the requirements for the Doctor of
Philosophy degree in Mechanical Engineering
in the Graduate College of
The University of Iowa

December 2009

Thesis Supervisor: Professor Christoph Beckermann

Graduate College
The University of Iowa
Iowa City, Iowa

CERTIFICATE OF APPROVAL

_____

PH.D. THESIS

_____

This is to certify that the Ph.D. thesis of

Antonio Jose Melendez Ramirez

has been approved by the Examining Committee
for the thesis requirement for the Doctor of Philosophy
degree in Mechanical Engineering at the December 2009 graduation.

Thesis Committee: _____
                    Christoph Beckermann, Thesis Supervisor

                  _____
                    H. S. Udaykumar

                  _____
                    Albert Ratner

                  _____
                    James Buchholz

                  _____
                    David Rethwisch

ABSTRACT

Measurements are carried out for dendrite tip growth of succinonitrile-acetone alloys solidifying freely in an undercooled melt. The current experimental investigation is conducted using the equiaxed dendritic solidification experiment (EDSE). This setup allows for precise measurements of the dendrite tip velocity, radius and shape for a range of undercoolings and solute concentrations. The collected data are compared to available theories of free dendritic growth, such as the Lipton-Glicksman-Kurz and Li-Beckermann models. It is found that for dilute succinonitrile-acetone alloys, the measured dendrite tip Péclet numbers agree well with previous theories of free dendritic growth, if the effects of melt convection are taken into account. The tip selection parameter deviates significantly from the pure succinonitrile value and is inversely related to the applied undercooling. Besides, the selection parameter shows no dependence on the solute concentration. These results are consistent with phase-field simulations and preceding experimental investigations. In addition, scaling relationships for the sidebranching shape were obtained in terms of the dendritic envelope, projection area and contour length. These new scaling relations agree well with previous measurements in pure succinonitrile dendrites by Li and Beckermann.

TABLE OF CONTENTS

LIST OF TABLES

Table

LIST OF FIGURES

Figure

CHAPTER I

INTRODUCTION

1.1 Background and Motivation

Dendrites are the most abundant micro-structural feature in metal castings. These crystals resemble trees with different levels of branching (Figure 1.1), which facilitate the transport of latent heat and solute from the solid to the undercooled liquid. Since the redistribution of latent heat and solute determines the formation of the microstructure, which directly affects the physical and chemical properties of casting material a thorough understanding of free dendritic growth is necessary. Moreover, the state of the art in microstructure simulation involves modeling the interplay of two very complex physical phenomena: the phase transformation kinetics and the macro-transport of energy and species [109]. The understanding of free dendritic growth plays a key role in modeling both. On one hand, most deterministic models of phase transformation kinetic are based on dendritic growth laws. On the other hand, the permeability of the solidifying metal, which affects the formation of macrosegregation features during solidification, is determined by the dendritic sidebranching or arm-spacing. Consequently, free dendritic growth remains an important research topic in physics, metallurgy, materials science and engineering.

Most deterministic theories and models for free dendritic growth are related in some way to the Ivantsov's solution [53]. This Russian scientist solved analytically the solidification problem for pure materials around a paraboloid of revolution in the absence of capillary and kinetics effects. Because of that, the transport solution of Ivantsov can only predict the product of dendrite tip velocity and radius, or Peclet number, for a specified undercooling. In reality, dendrites are far from being branchless (Figure 1.1) and they select unique values of tip velocity and radius for every given undercooling.

Additionally, dendritic crystals grow along preferential directions. All these characteristic features are caused by the anisotropy of the free surface energy.

Numerous research initiatives have been undertaken in order to consider capillary effects during dendritic solidification. Such efforts have resulted in selection criteria that uniquely determine tip velocity (V) and radius (ρ). Most proposed criteria are based on the selection parameter $\left(\sigma^* \propto 1/\left(V\rho^2\right)\right)$, which accounts for the competition between heat diffusion and capillary effects. The microscopic solvability theory (MST) proposed by Brener [16-17] considers that the selection parameter is a material-dependent constant. Furthermore, the selection constant is determined exclusively by the anisotropy's strength of the free surface energy. The MST also quantifies the deviation of the dendrite tip from Ivantsov paraboloid through a harmonics expansion. The coefficient corresponding to the first non-axisymmetric harmonic (A_4) is considered as a measure of the anisotropy of the dendrite tip shape, and it is expected to be a universal constant. Experimental studies with pure succinonitrile by Glicksman and coworkers [69] validate partially the MST (Figure 1.2). These authors found a weak dependence between the selection parameter and the undercooling. In the case of A_4, the measured values were about half of theoretical predictions. Numerical simulations, such as those by Karma et al. [59-60] using the phase field method, also show that the dendrite's shape is universal and support the MST.

During free dendritic growth of alloys, both latent heat release and solute rejection tend to destabilize the interface. On one hand, these combined effects reduce the tip radius and increase the tip velocity. On the other hand, the much smaller diffusion rate of solute compared to heat retards the growth. The competition between heat and solute transport causes a maximum in the dendrite velocity at small solute concentrations. A model for stationary free dendritic growth of alloys was proposed by Lipton, Glicksman and Kurz [87-89]. In the LGK model, the total undercooling results from the superposition of the thermal, solutal and capillary contributions. In addition, dendrites are considered paraboloids of revolution or branchless needle crystals, and the Ivantsov

solution is employed to account for both heat and mass transport. The marginal stability theory is used to determine the operating tip velocity and radius. Currently, the LGK model is extensively used to study free dendritic growth of alloys.

Li and Beckermann [84] modified the LGK model in order to consider the effects of thermosolutal convection. They compared the predictions of their new LB model and the LGK theory to experimental data of Chopra et al. [23]. Such experiments were performed on a succinonitrile-acetone (SCN-ACE) transparent alloy system. These authors [84] found reasonable agreement between Chopra's experiments [23] and the studied models for solute concentrations below 0.1% mol. Above 0.1% mol, none of the models were completely validated. Furthermore, the selection parameter is not constant along the entire range of studied undercoolings (Figure 1.3). Li and Beckermann [84] concluded that convection cannot cause these disagreements because the observed trends are independent of the undercooling and they are not mitigated by increments in the solute concentration. These findings question both the models of free dendritic growth for alloys and the consistency of the experimental data reported by Chopra and coworkers [23].

Recently, Rebow and Browne [104] studied the influence of the selection constant on the models of columnar-dendritic growth solidification and the criteria of columnar to equiaxed transition. They concluded that these models have a strong dependence on the selection parameter. Similarly, Kraft et al. [70] showed that microsegregation predictions for alloys with small freezing range rely greatly on the selection constant. In addition, the selection constant plays a key role in models of solidification such as cellular-automaton, front-tracking methods and multiphase volume-averaging formulations. Consequently, it is worthwhile to further validate the existing models for free dendritic growth of alloys or to develop new models. In order to achieve that goal, new experimental benchmarks for free dendritic growth of alloys are required.

1.2 Aim of the Current Research

The goal of the present research is to provide new experimental benchmarks for succinonitrile-acetone alloys. These new data will be helpful for development of new theoretical models and for validating the existing models and numerical simulations of free dendritic growth in alloys. Specifically, new and more complete benchmarks will allow further investigation and development of the MST and dendritic growth theories for alloys.
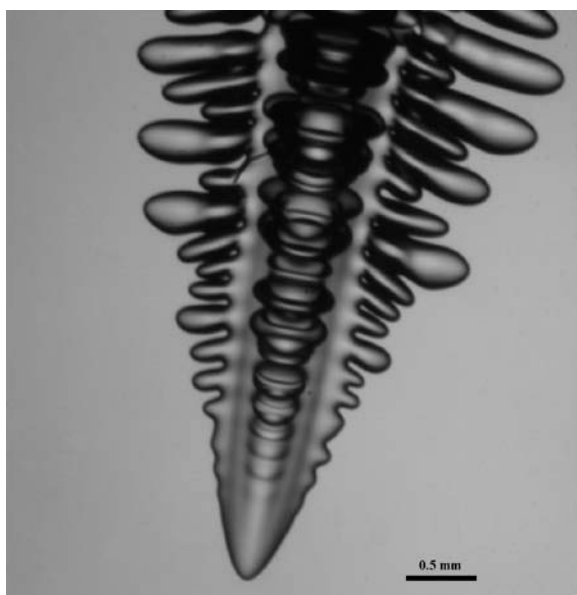
(a)
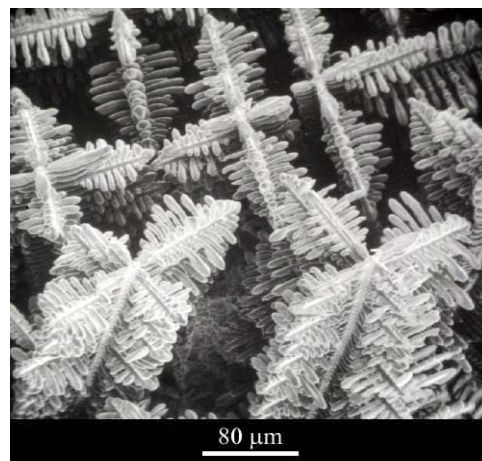
(b)

Figure 1.1: Micrographs of dendrites
     (a) Pure succinonitrile.
     (b) Cobalt-Samarium-Copper alloy [39]
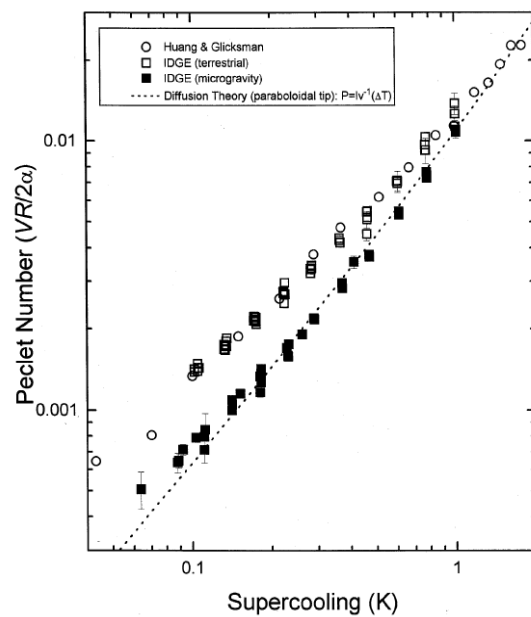
(a)
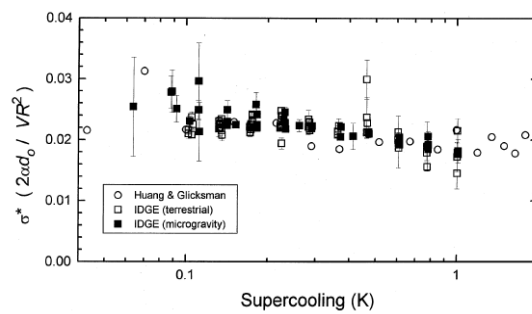
(b)

Figure 1.2: Validation of the theories of dendritic growth for pure substances [69].
    (a) Verification of the transport model.
    (b) Verification of the selection criterion.

(a)

(b)
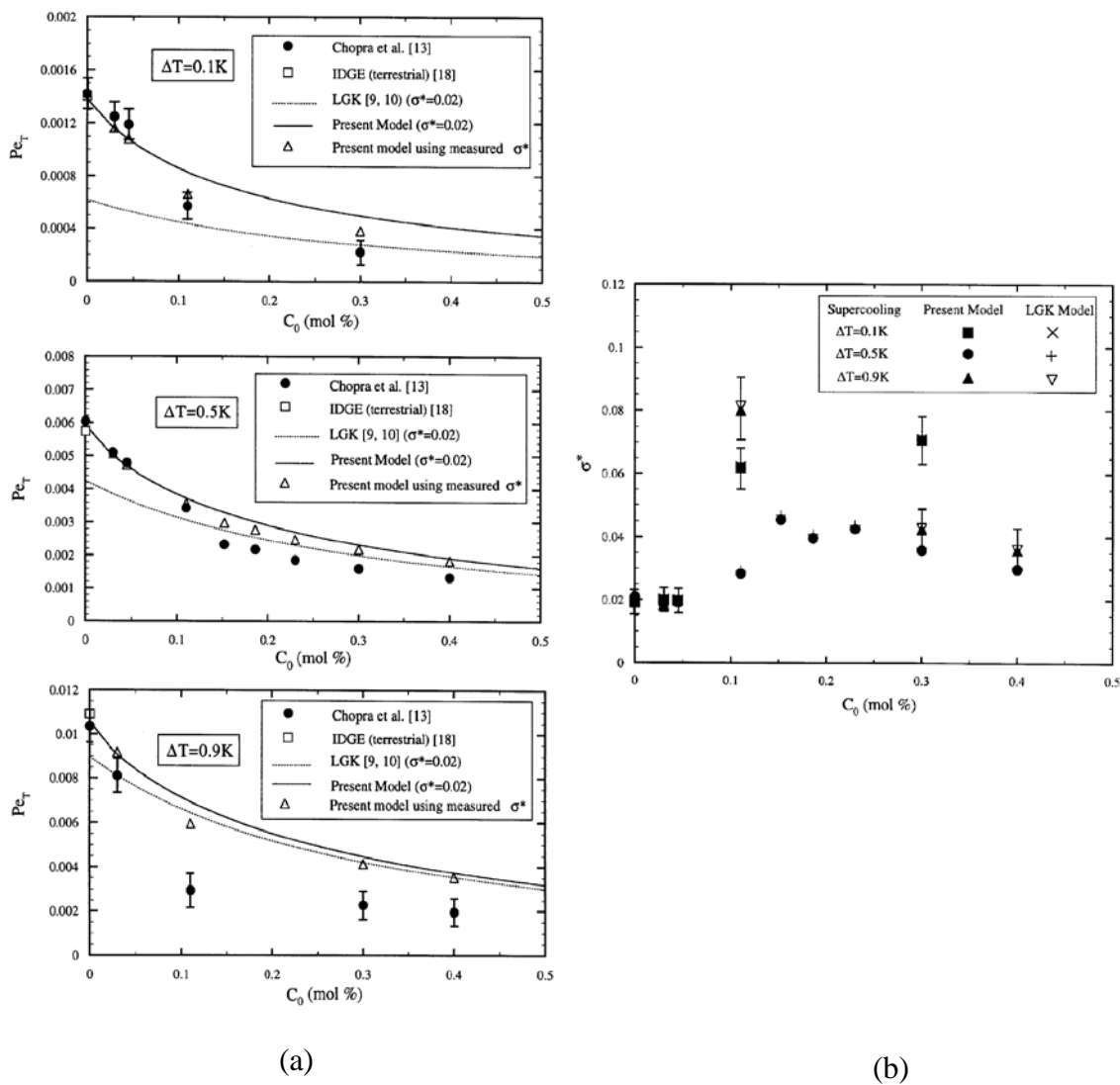
Figure 1.3: Validation of the theories for dendritic growth in alloys by Chopra et al. [23].
(a) Verification of the transport model.
(b) Verification of the selection criterion.

CHAPTER II

LITERATURE REVIEW

2.1 Introduction

Dendrites are the predominant microstructure in metal castings. Their characteristic length scales, such as tip radius, and primary and secondary arm spacings, determine the properties of the casting materials. Consequently, extensive research has been devoted to dendritic growth during the last sixty years. Important contributions have been made through theoretical, numerical, and experimental studies. Historically, dendritic growth has been considered as a coupling of steady-state movement of the tip and transient formation of sidebranches behind the tip. Each of these mechanisms has been studied separately and most investigations have been aimed at the stationary propagation of the dendrite tip. The following sections provide a brief overview of the literature concerning theoretical, experimental, and numeric investigations of the steady-state propagation of the dendrite tip.

Dendritic growth can occur in two different scenarios, depending on how the latent heat of fusion is removed from the interface. If the latent heat is dissipated through the liquid, the growth is considered free. Conversely, the latent heat is evacuated across the solid during constrained growth. This review will be focused on free dendritic growth.

2.2 Free dendritic growth

When the latent heat flows in the growth direction, the solidification front is unstable under morphological perturbations (Fig. 2.1). Since solid nuclei are surrounded by undercooled liquid, there is no temperature gradient across the solid. Consequently, removal of the latent heat of fusion depends only on the liquid temperature gradient at the interface. Any perturbation makes the liquid temperature gradient steeper on the interface

peaks. The opposite behavior is observed on the interface valleys. Therefore, interface peaks can release more latent heat and grow faster. This condition favors the formation of equiaxed dendrites.

2.2.1 Mathematical formulation

Free dendritic growth can be described by solving transport equations for mass, momentum, energy, and species for both liquid and solid phases. Interfacial phenomena are considered through the boundary conditions. Depending on the solving approach, the governing equations are modified or simplified accordingly. The discussion of each solving methodology is beyond the scope of this review. Instead, some general and simple formulations for alloys are presented here. Governing equations for a pure substance can be obtained by simplifying the formulation presented for alloys. Historically, only diffusive phenomena were considered initially in the study of free dendritic growth. However, the importance of convective transport in the liquid phase was recognized and considered in posterior studies. Mathematical formulations for diffusive and diffusive-convective free dendritic growths are presented in the next subsections. Additionally, the Ivantsov solution is discussed in the last subsection because it is the foundation for theories of free dendritic growth.

2.2.1.1 Diffusion-controlled formulation

When there is no flow in the liquid, the free dendritic growth or equiaxed solidification can be described using the transport equations of mass and species for each phase. Assuming the densities of both phases are equal, the following set of equations is obtained:

$$\partial_t T_l = \alpha_l \nabla^2 T_l \tag{2.1}$$

$$\partial_t T_s = \alpha_s \nabla^2 T_s \tag{2.2}$$

$$\partial_t C_l = D_l \nabla^2 C_l \tag{2.3}$$

$$\partial_t C_s = D_s \nabla^2 C_s \tag{2.4}$$

with the corresponding set of boundary conditions:

$$T_l = T_M + mC_l - \Gamma\kappa - V_n / \mu_k \qquad \text{(Gibbs-Thomson condition)} \tag{2.5}$$

$$\rho L_f V_n = k_s \partial_n T_s - k_l \partial_n T_l \qquad \text{(Stefan condition)} \tag{2.6}$$

$$\rho C_l (1 - k) V_n = \rho (D_s \partial_n C_s - D_l \partial_n C_l) \qquad \text{(Species balance at the interface)} \tag{2.7}$$

where α_l is the liquid thermal diffusivity, T_l is the temperature field in the liquid, α_s is the solid thermal diffusivity, T_s is the temperature field in the solid, D_l is the solutal diffusivity in the liquid, C_l is the mole fraction of solute in the liquid, D_s is the solutal diffusivity in the solid, C_s is the mole fraction of solute in the solid, T_M is the melting point of pure solvent, m is the liquidus slope of the dilute alloy phase diagram, Γ is the Gibbs-Thomson coefficient, κ is the local curvature of the interface, V_n is the normal velocity of the interface, μ_k is the kinetic coefficient, ρ is the density of the working material, L_f is the latent heat per unit mass, k_s is the solid thermal conductivity, k_l is the liquid thermal conductivity and k is the partition coefficient.

The Gibbs-Thomson condition requires a closer examination. The formulation presented in Equation (2.5), although correct and well-known, buries the mechanism that causes dendrites formation. Let us consider a more rigorous form of the Gibbs-Thomson condition:

$$T_l = T_M - \frac{T_M}{L_f} \sum_{i=1,2} \left[\gamma(\hat{n}) + \frac{\partial^2 \gamma(\hat{n})}{\partial \theta_i^2} \right] \frac{1}{R_i} + mC_l - \frac{V_n}{\mu_k(\hat{n})} \tag{2.8}$$

where $\gamma(\hat{n})$ is the excess free-energy of the solid-liquid interface, θ_i are the azimuth and elevation angles measured among the normal to the interface $\hat{n}$ and the two principal directions on the interface, R_i are the principal curvature radii, V_n is the normal velocity of the interface, and $\mu_k(\hat{n})$ stands for the kinetic coefficient. The term between

parentheses is called the interface stiffness, and it quantifies the opposition of the interface to be deformed. Both the excess free-energy of the interface and the kinetics coefficient are direction-dependent, or anisotropic, properties. Moreover, the anisotropy in the excess free-energy of the interface tends to maximize the kinetics coefficient while minimizing the interface stiffness. Because of that, the materials grow along preferred directions in order to minimize the area of the interface on those regions with the highest excess free-energy of the interface. Besides, the velocity of the dendrite tip is also determined by the anisotropy of the thermodynamic and kinetic properties.

For rough solid-liquid interfaces, the anisotropy of the excess free-energy has a magnitude around 1-2 %. Despite this small magnitude, the anisotropy of the excess free-energy rules the physical phenomena behind the dendrite formation. Consequently, the anisotropy of the excess free-energy is considered a singular perturbation of the solidification problem. The relationship between the interface stiffness and the interfacial excess energy, the bracket in eqn. 2.8, explains to some degree how the anisotropy of the interfacial excess free-energy has such a strong influence on the solidification problem. The interface stiffness's anisotropy is more than one order of magnitude bigger than the anisotropy in the interfacial excess free-energy [49].

The free dendritic growth remains a challenging research topic because the length scales that control this phenomenon are several orders of magnitude apart. Typically, the dendrite tip radii, observed experimentally, are on the order of microns. The actual interface thickness is on the order of nanometers according to molecular simulations. Finally, the macro-transport of energy and species ahead of the dendrite is controlled by a length scale on the order of hundreds of microns. Consequently, advances in new multiscale theoretical and numerical methods, new experimental techniques and more powerful computer are needed to increase the understanding of the free dendritic growth phenomena.

2.2.1.2 Convective-diffusive formulation

In order to study convective effects, the transport equations of mass, momentum, energy and species need to be solved for the liquid phase. Generally, the liquid is considered incompressible, and the solid is assumed rigid. Consequently, only transport of energy and species are considered in the solid phase. Moreover, diffusion is the only mechanism driving transport of energy and species inside the solid. Under these assumptions, the set of governing equations is reduced as follows:

$$\nabla \cdot \boldsymbol{u}_l = 0 \tag{2.8}$$

$$\partial_t \rho_l \boldsymbol{u}_l + \nabla \cdot \rho_l \boldsymbol{u}_l \boldsymbol{u}_l = -\nabla p_l + \mu_l \nabla^2 \boldsymbol{u}_l \tag{2.9}$$

$$\partial_t T_l + \nabla \cdot \boldsymbol{u}_l T_l = \alpha_l \nabla^2 T_l \tag{2.10}$$

$$\partial_t T_s = \alpha_s \nabla^2 T_s \tag{2.11}$$

$$\partial_t C_l + \nabla \cdot \boldsymbol{u}_l C_l = D_l \nabla^2 C_l \tag{2.12}$$

$$\partial_t C_s = D_s \nabla^2 C_s \tag{2.13}$$

with the corresponding set of boundary conditions:

$$T_l = T_M + mC_l - \Gamma \kappa - V_n / \mu_k \qquad \text{(Gibbs-Thomson condition)} \tag{2.14}$$

$$\rho_s L_f V_n = k_s \partial_n T_s - k_l \partial_n T_l \qquad \text{(Stefan condition)} \tag{2.15}$$

$$\rho_s C_l (1 - k) V_n = \rho_s D_s \partial_n C_s - \rho_l D_l \partial_n C_l \qquad \text{(Species balance at the interface)} \tag{2.16}$$

where $\boldsymbol{u}_l$ is the liquid velocity, ρ_l is the liquid density, p_l is the pressure in the liquid, μ_l is the dynamic viscosity of the liquid, α_l is the liquid thermal diffusivity, T_l is the temperature field in the liquid, α_s is the solid thermal diffusivity, T_s is the temperature field in the solid, D_l is the solutal diffusivity in the liquid, C_l is the mole fraction of solute in the liquid, D_s is the solutal diffusivity in the solid, C_s is the mole fraction of solute in the solid, T_M is the melting point of pure solvent, m is the liquidus slope of the

dilute alloy phase diagram, Γ is the Gibbs-Thomson coefficient, κ is the local curvature of the interface, V_n is the normal velocity of the interface, μ_k is the kinetic coefficient, ρ_s is the solid density, L_f is the latent heat per unit mass, k_s is the solid thermal conductivity, k_l is the liquid thermal conductivity and k is the partition coefficient.

2.2.1.3 Ivantsov solution

In 1935, Papapetrou [99] introduced the notion that dendrites can be approximated by a paraboloid of revolution. Moreover, he proved the existence of solutions for the dendrite problem around this shape. However, the solution itself was found by Ivantsov [53] twelve years later. In 1961, Horvay and Cahn [47] generalized the Ivantsov analysis using separation of variables. Recently, Dantzig and Rappaz [27] reviewed the solidification problem around a paraboloid following the approach of Horvay and Cahn rewriting its solution in terms of the Stefan and Peclet number. This section will describe the Ivantsov solution following roughly the same approach.

The starting point in the Ivantsov analysis is the diffusion-controlled formulation for a pure substance. Assuming the dendrite moves with constant velocity, the governing equations can be rewritten in stationary form using a moving reference frame attached to the dendrite. Such a coordinate system is illustrated in Figure 2.2a. The paraboloid surface in the new coordinate system is described by the following expression:

$$z = \frac{R}{2} - \frac{r^2}{2R} \tag{2.17}$$

where $r = \sqrt{x^2 + y^2}$ and R is the tip radius. Neglecting kinetics and capillary effects at the interface and assuming the melt infinite, the governing equations are simplified as follows:

$$-V\partial_z T_l = \alpha_l \nabla^2 T_l \tag{2.18}$$

$$-V\partial_z T_s = \alpha_s \nabla^2 T_s \tag{2.19}$$

$$T_l = T_s = T_f \qquad \text{(Gibbs-Thomson condition)} \qquad (2.20)$$

$$\rho L_f V = k_s \partial_n T_s - k_l \partial_n T_l \qquad \text{(Stefan condition)} \qquad (2.21)$$

$$T_l = T_\infty \qquad \text{(Far away of the interface)} \qquad (2.22)$$

A uniform temperature field inside the solid ($T_s = T_f$) satisfies Equations (2.18) and (2.19). Now, only the temperature distribution in the liquid is missing. At this point, it is convenient to scale the remaining governing equations. The proposed scaled quantities are:

$$\varsigma = \frac{z}{\rho}; \quad \chi = \frac{r}{\rho}; \quad \theta_l = \frac{T_l - T_\infty}{T_f - T_\infty} \qquad (2.22)$$

The interface is described in terms of the scaled variables by the following expression:

$$\varsigma = \frac{1}{2}\left(1 - \chi^2\right) \qquad (2.23)$$

The governing equations for the liquid are expressed in terms of the scaled variables as follows:

$$-2Pe_T \partial_\varsigma \theta_l = \nabla^2 \theta_l \qquad \text{(In the proximity of the interface)} \qquad (2.24)$$

$$\theta_l = 1 \qquad \text{(At the interface)} \qquad (2.25)$$

$$\theta_l = 0 \qquad \text{(Far away of the interface)} \qquad (2.26)$$

$$\frac{2Pe_T}{Ste} = -\partial_n \theta_l \qquad (2.27)$$

here $Pe_T = V\rho/2\alpha$ and $Ste = c_L(T_f - T_\infty)/L_f$ represent the thermal Peclet and Stefan numbers, respectively. In the definition of the Stefan number, the symbol c_l stands for the specific heat at constant pressure for the liquid.

A transformation to the paraboloidal coordinates (ξ, η) conforming the solid makes all boundary conditions and the final solution independent of η. Such transformation is given by:

$$\varsigma = \xi\eta; \quad \chi = 1/2\left(\xi^2 - \eta^2\right) \tag{2.28}$$

$$\xi^2 = \varsigma + \sqrt{\chi^2 + \varsigma^2}; \quad \eta^2 = -\varsigma + \sqrt{\chi^2 + \varsigma^2} \tag{2.29}$$

The new coordinate system is presented in Figure 2.2a. Finally, the temperature profile in the liquid is given by:

$$\theta_l = \frac{E_1\left[Pe_T \xi^2\right]}{E_1\left[Pe_T\right]} \quad \text{with} \quad \xi \geq 1 \tag{2.30}$$

here E_1 is the exponential integral function defined by:

$$E_1(\xi) = \int_{\xi}^{\infty} z^{-1} e^{-z} dz \tag{2.31}$$

Substituting the temperature of the liquid θ_l on the Stefan condition, using the properties of the exponential integral function and evaluating $\xi = 1$, the Ivantsov solution is obtained:

$$Ste = Pe_T \exp(Pe_T) E_1(Pe_T) \tag{2.32}$$

The right side of Equation 2.32 is called the Ivantsov function ($Iv(\ )$). Equation 2.32 can be presented in terms of the dimensional undercooling:

$$\Delta T = \left(L_f / c_L\right) Iv(Pe_T) = \left(L_f / c_L\right) Pe_T \exp(Pe_T) E_1(Pe_T) \tag{2.33}$$

The set of assumptions proposed by Ivantsov overconstrains the solidification problem by neglecting the surface tension on the boundary conditions. As a result, the transport solution of Ivantsov can only predict the product of dendrite tip velocity (V)

and radius (R) for given undercooling (ΔT). Actually, dendrites choose unique values of tip velocity and radius for a given undercooling. In spite of this drawback, the Ivantsov solution has played a key role in the study of free dendritic growth. It is used to model the heat and mass transport around dendrites in most theories of free dendritic growth.

<div align="center">2.2.2 Theory of dendritic growth for pure substances</div>

Most theories of free dendritic growth have two components. The first part is a model for transport phenomena around dendrites generally based on the Ivantsov solution. The second portion is a selection criterion, which assists the transport model in determining the operation conditions (V and R) of the dendrite tip. Extensive research has been done to develop selection criteria. However, none of the proposed criteria are able to match all experimental observations available. Among the existing selection criteria, the microscopic solvability theory (MST) is the most widely accepted because of its rigorous mathematical foundations and its extensive validation through numerical simulations. The MST proposes that the selection parameter $\left(\sigma^*\right)$ depends uniquely on the anisotropy of the excess free surface energy $\left(\gamma\right)$. Unfortunately, the measurement of the excess free surface energy and its anisotropy has been a very challenging endeavor thus far. For this reason, the experimental validation of the MST is lacking.

2.2.2.1 Microscopic solvability theory (MST)

In order to consider anisotropic capillary effects, Brener [16-17] proposed the three-dimensional MST using the method of asymptotic expansions beyond all orders. In the MST, the singularities of a non-axisymmetric shape deviation from the Ivantsov paraboloid are mapped in the complex plane. Around these singular points, a pseudo boundary layer equation is formulated. The solvability condition for this equation constitutes the selection criterion for the dendrite velocity and shape. So far, the MST has

been focused on materials with fourfold- and sixfold-symmetry. In the three-dimensional case, the surface energy of this type of materials is considered to be given by:

$$\gamma(\theta,\varphi) = 1 + 4\varepsilon\left(\cos^4\theta + \frac{3}{4}\sin^4\theta + \frac{1}{4}\sin^4\theta\cos 4\varphi\right) \tag{2.34}$$

where θ and φ are the Eulerian angles of the interface normal vector, and ε is the strength of the anisotropy. The non-axisymmetric shape (Figure 2.3) studied by Ben Amar and Brener is the following:

$$z = -\underbrace{\frac{r^2}{2}}_{\substack{\text{Ivantsov}\\\text{Paraboloid}}} + \underbrace{\sum A_m r^m \cos(m\phi)}_{\substack{\text{Non-axisymmetric}\\\text{Correction}}} \tag{2.35}$$

where r and ϕ are polar coordinates in the plane perpendicular to the growth direction. Additionally, the axial (z) and radial (r) coordinates have been scaled using the tip radius (R). Equation 2.35 is valid only in the immediate proximity of the tip radius because the harmonics $r^m \cos(m\phi)$ grow faster than the Ivantsov paraboloid. Following the approach proposed by Kessler and Levine [63-64], Ben Amar and Brener [9] considered only the first non-axisymmetric harmonic $r^4 \cos(4\phi)$ and found from the solvability condition that the selection parameter $\sigma*$ and coefficient A_4 are pure numbers given by:

$$\sigma* = \sigma_0 \varepsilon^{7/4} \tag{2.36}$$

$$A_4 = 1/88 \tag{2.37}$$

where σ_0 is an unit constant. Brener and Melnikov [18] revised and extended the MST, considering non-stationary perturbations of the dendrite tip. They found a slightly different value for A_4:

$$A_4 = 1/96 \tag{2.38}$$

The MST also describes the dendrite's tail or sidebranching. Brener [16-17] obtained a model for the tail's shape by considering the two-dimensional, transient movement of the dendrite's cross section. The Laplace equation governs such motion if the tail's cross sectional area is much smaller than the thermal diffusion length. Algrem et al. [1] found the solution for two-dimensional Laplacian problems while studying anisotropic Hele Shaw flow. Using Algrem's findings, Brener proposed the following tail's shape in terms of the sidearms' width (Y_w):

$$\frac{Y_w}{R} = \left(\frac{5}{3}\frac{Z}{R}\right)^{2/5}\left(\frac{\sigma^*}{\sigma_2^*}\right)^{1/5}\left(\frac{X}{X_{act}}\right)^{2/3}\int_{X/X_{act}}^{1}\frac{ds}{s^{2/3}\sqrt{1-s^4}} \tag{2.39}$$

where R represents the tip radius, (X,Y,Z) stand for the reference coordinates (Cartesian), σ^* is the selection parameter for the dendrite's tip, and σ_2^* corresponds to the selection parameter for the tip of active sidebranches. Brener also stated that the distance form the growth axis to the tip of the active sidebranches (X_{act}) is given by:

$$\frac{X_{act}}{R} = \left(\frac{5}{3}\frac{Z}{R}\right)^{3/5}\left(\frac{\sigma^*}{\sigma_2^*}\right)^{1/5} \tag{2.40}$$

In general, the selection parameters (σ^*, σ_2^*) are assumed equal. It is important to note that the tail's shape presented above does not consider the effects of the thermal noise on the sidebranching. Brener and Temkin [20] studied the time-dependent behavior of the sidebranching using the non-axisymmetrical shape of the needle crystal. These authors found that the thermal noise waves generated at the dendrite tip increase their amplitude while they move down the dendrite's sides creating sidebranches. Furthermore, the thermal noise is amplified exponentially as a function of $(Z/R)^{2/5}/(\sigma^*)^{1/2}$. This result shows a better agreement with sidebranching's measurements than predictions based on axisymmetrical shapes. Brener and Temkin also investigated the behavior of the sidearms in the non-linear regime $(1 << Z/R << 1/Pe_T)$, where the sidebranches do not

behave as free dendrites yet. In this region, the competition among the sidearms creates a spacing of the surviving sidebranches (λ_s) that is proportional to their length (l_s). All scaling relations derived by Brener and Temkin can be summarized as follows:

$$\lambda_s(Z/R) \sim l_s(Z/R) \sim s(Z/R) \sim Z/R \tag{2.41}$$

where s stands for the cross sectional area of sidebranching. Such relationships imply that the sidearms inside the non-linear region can be modeled using geometrical, undercooling-independent parameters that can be scaled by the tip radius.

Since the MST theory accounts for the anisotropy of interfacial energy, it addresses the fact that dendrites grow in preferential directions. Consequently, more realistic predictions are expected from this theory. In fact, phase-field simulations [58-60, 101,123] and an experimental investigations [90] agree quantitatively with MST. However, recent atomistic simulations of fcc* metallic materials [46-48] have shown that at least two parameters are required to accurately describe the anisotropy of the free surface area:

$$\gamma(\theta, \varphi) = \gamma_0 \left[1 + \varepsilon_1 K_1(\theta, \varphi) + \varepsilon_2 K_2(\theta, \varphi)\right] \tag{2.42}$$

where θ and φ are the Eulerian angles of the interface normal vector, γ_0 stands for the orientation-averaged interfacial free energy, ε_1 and ε_2 correspond to the strength of the four- and six-folds anisotropy cubic-harmonics $(K_1 \& K_2)$, respectively. Furthermore, new solvability theory calculations and phase field simulations [46] for free dendritic growth indicates that the selection parameter $\sigma*$ depends acutely on both ε_1 and ε_2. In light of these new findings, a re-examination of the microscopic solvability theory for alloys is needed.

---

* Face-centered cubic

2.2.3 Models for dendritic growth for alloys

Since the solids have crystalline structures, they have less internal free space to accommodate solute molecules. Consequently, the solubility of alloys is higher in liquids than in solids (Fig 2.4). During dendritic solidification of alloys, solute and latent heat are rejected from the solid into the liquid. The interplay between latent heat release and solute rejection is very complex, but both phenomena tend to destabilize the interface. On one hand, these combined effects reduce the tip radius and increase the tip velocity in comparison to pure substance at the same undercooling. On the other hand, the much smaller diffusion rate of solute compared to heat retards the growth. The competition between heat and solute transport causes a maximum in the dendrite velocity at small solute concentrations. This behavior is predicted qualitatively by most theories of dendritic growth for alloys. It also was documented in the experimental study of succinonitrile-acetone alloys by Chopra et al. [23].

Most theoretical models for free dendritic growth of alloys predict the steady state tip velocity and radius for a given undercooling and solute concentration. These models consider that the total undercooling (ΔT) results from the superposition of the thermal (Δ_T), solutal (Δ_C) and capillary (Δ_R) contributions (Fig. 2.5). Dendrites are considered paraboloids of revolution or branchless needle crystals in these models. Consequently, the Ivantsov function is employed to account for both heat and mass transfer. The marginal-stability theory is the most frequently used selection criterion. Currently, the Lipton-Glicksman-Kurz (LGK) model [87-88] is the most extensively used for free dendritic growth of alloys. In the next subsections, the most accepted theories of dendritic growth for pure substance are reviewed.

2.2.3.1 Lipton-Glickman-Kurz (LGK) model

The LGK theory assumes that thermal and solutal transport at the tip of the dendrite of a dilute binary alloy occurs with constant partitions coefficient k and a

liquidus line of constant slope m. For tri-dimensional parabolic dendrites, neglecting the kinetic effects, the total imposed undercooling, ΔT is given by

$$\Delta T = \left(\frac{L_f}{c_l}\right)\Delta_T + \frac{k\Delta T_0 \Delta_C}{1-(1-k)\Delta_C} + \frac{2\Gamma}{R} \tag{2.41}$$

where on the right hand side, the three terms represent thermal, solutal, and capillary contributions to the total undercooling respectively, L_f is the latent heat of fusion, c_l is the specific heat of the liquid, $\Delta T_0 = |m|C_\infty(1-k)/k$ is the equilibrium freezing temperature range corresponding to C_∞ and Γ is the Gibbs-Thomson coefficient. R is the tip radius and is based on the assumption that the dendrite has a parabolic shape. One can notice that for a three-dimensional situation, where the dendrite assumes a paraboloid shape, the capillary contribution is given by $2\Gamma/R$. The dimensionless thermal and solutal undercoolings are defined as

$$\Delta_T = \frac{T*-T_\infty}{L_f/c_l} = Iv(Pe_T) \tag{2.42}$$

$$\Delta_C = \frac{C*-C_\infty}{(1-k)C*} = Iv(Pe_C) \tag{2.43}$$

where $T*$ and $C*$ are the temperature and solute concentration in the liquid and at the dendrite tip, respectively. $Pe_T = VR/2\alpha$ and $Pe_C = VR/2D$ are the thermal and solutal Peclet numbers, α is the thermal diffusivity and D is the liquid mass diffusivity. Notice that $T*$ and $C*$ are unknown. The dimensionless undercoolings are calculated from the Ivantsov solutions for the steady state heat and solute diffusion around a parabolic dendrite. Although the Ivantsov function solution assumes an isothermal interface, the capillary effect varies along the curvature of the interface, making it non-isothermal. However, the contribution of the capillary effect can only be considered as a first approximation. A thorough discussion of this issue was published by Trivedi [116-117].

After some algebra, the transport equation for the LGK model is rewritten as follows:

$$\Delta = Iv(Pe_T) + \frac{Mc_\infty Iv(Pe_C)}{1 - (1-k)Iv(Pe_C)} + \Delta_R \qquad (2.44)$$

where $M = -m(1-k)/(L_f/c_l)$ is a scaled liquidus slope, $\Delta_R = 2\Gamma c_l/(\rho L_f) = 2d_0/R$ is the dimensionless capillary undercooling and d_0 is the capillary length.

Equation 2.46 possesses two unknowns, namely the tip radius and velocity. Consequently, it only allows calculating the product RV. For this reason, the marginal-stability criterion is employed to uniquely establish tip velocity and radius. Additionally, the definition of the selection constant is modified to account for thermal and solutal effects:

$$\sigma^* = \frac{d_0}{R\left[Pe_T + 2Pe_C\left(\frac{k\Delta T_0/(L_f/c_l)}{1-(1-k)\Delta_C}\right)\right]} \qquad (2.45)$$

where σ^* is a selection parameter that is supposed to be independent of thermal undercooling and alloy composition [87-88].

2.2.3.2 Lipton-Kurz-Trivedi (LKT) model

The transport portion of this model is identical to its counterpart for the LGK model (Equation 2.44). The selection criterion for the LKT model was modified to account for large Peclet numbers [89]:

$$\sigma^* = \frac{d_0}{R\left[Pe_T\xi_T + 2Pe_C\xi_C\left(\frac{k\Delta T_0/(L_f/c_l)}{1-(1-k)\Delta_C}\right)\right]} \qquad (2.46)$$

where the correction parameters ξ_T and ξ_C are given by:

$$\xi_T = 1 - \frac{1}{\sqrt{1 + \dfrac{1}{\sigma * (Pe)^2}}} \tag{2.47}$$

$$\xi_C = 1 + \frac{2k}{1 - 2k - \sqrt{1 + \dfrac{1}{\sigma * (LePe)^2}}} \tag{2.48}$$

2.2.3.3 Li-Beckermann (LB) model

In order to consider the effects of both thermal and solutal convection, Li and Beckermann [84] modified the transport portion of the LGK model using a stagnant film model. For alloys, both thermal (δ_T) and solutal (δ_C) boundary layer thicknesses need to be included in the stagnant model:

$$\Delta_T = Pe_T \exp(Pe_T)\{E_1(Pe_T) - E_1[Pe_T(1 + 2\delta_T / R)]\} \tag{2.49}$$

$$\Delta_C = Pe_C \exp(Pe_C)\{E_1(Pe_C) - E_1[Pe_C(1 + 2\delta_C / R)]\} \tag{2.50}$$

where Δ_T and Δ_C are the thermal and solutal undercooling, respectively and E_1 is the exponential integral function (Equation 2.31). they estimated the boundary layer thicknesses using correlations for Nusselt (Nu_R) and Sherwood (Sh_R) numbers based on tip radius (R):

$$\delta_T / R = B / Nu_R \tag{2.51}$$

$$\delta_C / R = B / Sh_R \tag{2.52}$$

where B is a common constant for both boundary layers, and it is adopted as $B \approx 2$. Li and Beckemann employed the following correlations for Nusselt and Sherwood:

$$Nu_R = A(Ra_{R,T})^{1/4}\left(1 + \frac{N}{\sqrt{Le}}\right)^{1/4} \tag{2.53}$$

$$Sh_R = A(Ra_{R,C})^{1/4}\left(1 + \frac{\sqrt{Le}}{N}\right)^{1/4} \tag{2.54}$$

here $Le = Sc/Pr = \alpha/D$ is the Lewis number. The buoyancy parameter N (Equation 2.59) ponders interactions between boundary layers. Positive values of N mean cooperation between solutal and thermal effects. On the contrary, negative values of N indicate competition between them. Previous correlations are valid only for alloys with positive buoyancy parameters (N). The constant A is independent of Lewis number Le and N, and it was estimated as $A \approx 0.9$ following a boundary layer analysis. The preceding correlations are applicable for both vertical plates and spheres, and they do not include a diffusion limit for vanishing Raleigh number. Such consideration was done by Li and Beckermann through the modified Ivantsov function.

$$N = \frac{\beta_C\left(C^* - C_\infty\right)}{\beta_T\left(T^* - T_\infty\right)} \tag{2.55}$$

In Equation 2.55, β_C corresponds to solutal expansion coefficient, β_T represents the solutal expansion coefficient, C^* is the solute concentration at the dendrite tip, C_∞ symbolizes the initial or far-field solute concentration, T^* represents the temperature at the dendrite tip, and T_∞ corresponds to the initial or far-field temperature. Finally, Li and Beckermann estimated the boundary layer thicknesses as follows:

$$\frac{\delta_T}{R} = \frac{B}{A}\left(Ra_{R,T}\right)^{-1/4}\left(1 + \frac{N}{\sqrt{Le}}\right)^{-1/4} \tag{2.56}$$

$$\frac{\delta_C}{R} = \frac{B}{A}\left(Ra_{R,C}\right)^{-1/4}\left(1 + \frac{\sqrt{Le}}{N}\right)^{-1/4} \tag{2.57}$$

The ratio $B/A \approx 2.2$ was verified by the authors of the current model comparing the predictions of the model with the earth-based dendritic growth experiments for pure SCN of Huang and Glicksman [50-51].

Finally, Li and Beckermann [84] compared the predictions of their model and the LGK theory with the experimental data of Chopra and co-workers [23]. Such

experiments were performed on a succinonitrile-acetone (SCN-ACE) transparent alloy system. A significant disagreement in the tip radius and velocity was found for melt concentrations $c_\infty > 0.1$ mol %. The selection parameter σ^*, calculated with each pair of measured tip radius R and velocity V, was not constant. It exhibited a strong scatter that has not been explained. Owing to the fact that the LGK model is still used extensively, more experiments and numerical studies are required to validate the existing theories of dendritic growth or to propose new models.

2.2.4 Experimental studies of dendritic growth

Experimental observations play a key role in scientific development. They are useful not only for validation of model but for understanding the physical phenomena studied. In the case of free dendritic growth, experimental observation is rather complicated because metals and other casting material are opaque. The study of transparent analogous materials, such as succinonitrile and pivalic acid, has been the answer to that challenge. Nevertheless, the number of experimental benchmarks for free dendritic growth is very small. Only benchmarks of Koss et al. [69] for succinonitrile and LaCombe et al. [75] for pivalic acid are suitable for validating of dendritic growth theories for pure substances. In the case of alloys, only the data of Chopra et al. [23] is available. In general, experimental data for free dendritic growth validate partially the existing theories and models. Most validation studies indicate that convective and kinetic effects need to be considered in the theories of free dendritic growth. Also, more research is required to address the role of surface tension in free dendritic growth. In the next subsections the most important experimental contributions in the study of free dendritic growth are reviewed.

2.2.4.1 Pure substances studies

Huang and Glicksman [50-51] performed systematic measurements of dendrite tip radius and growth velocity for succinonitrile (SCN) with a purity of 99.99995 %. The

authors tested different dendritic theories under small undercoolings. They concluded that the Ivantsov solution models the heat transport correctly during dendritic growth. The deviations of the tip shape from Ivantsov paraboloid are essentially trivial. The stability criterion $\sigma*$ from the experiment was measured as 0.0195, which is in good agreement with the prediction of the marginal-stability criterion. For low undercoolings, $\sigma*$ rose slowly to about 0.025. This suggests that the natural convection effects play a dominant role at these conditions. The authors also found the ratio of the tip radius R and the marginally stable wavelength λ_s over the full range of undercoolings to be 1.2, which is only 20% above the value assumed by Langer and Müller-Krumbhaar [81-83].

Glicksman and coworkers [38, 40-41, 68-69, 72-75, 101] proposed and conducted the so-called isothermal dendritic growth experiment (IDGE). In this research project, free dendritic growth of pure succinonitrile (SCN) and pivalic acid (PVA) was studied experimentally under microgravity and terrestrial conditions. The set of experiments with SCN was carried out first, and its results agreed reasonably with the Ivantsov solution and the theories of dendritic growth. In Figure 2.6a, the comparison of IDGE microgravity growth data for SCN with terrestrial experiments and diffusion theories is shown. Much better agreements are found between the microgravity results and the theories. However, the microgravity data for undercoolings lower than 0.47K deviate significantly from theory, indicating that even in microgravity conditions, the influence of natural convection is still significant. In addition, a slight dependence of $\sigma*$ on undercooling was found. Also, a good agreement between terrestrial and microgravity $\sigma*$ was observed. Glicksman et al. [69] also reported that the Ivantsov diffusion solution combined with a constant selection parameter fails to consistently predict growth velocity and radius.

The shape of pure SCN dendrites was also studied by Glicksman and coworkers [73]. They used a fourth order polynomial to fit the dendrite contour and to measure A_4. Furthermore, these authors adopted a fitting range of eight radii behind the tip. The

reported datum $\left(A_4 = 0.004\right)$ is roughly half the size of the MST prediction $\left(A_4 = 0.0104\right)$. Surprisingly, the measured A_4 almost matches the prediction obtained from simulations $\left(A_4 = 0.0045\right)$ by Karma et al. [58]. In general, the experiments with pure SCN validate the microscopic solvability theory.

The IDGE data for pivalic acid (PVA), presented by Glicksman et al. [75], show strong disagreements with the theories of dendritic growth for pure substance. PVA dendrites cannot be represented by a paraboloid of revolution. The Peclet number predicted by the Ivantsov solution does not agree with the experimental data collected in microgravity conditions. Finally, the selection parameter shows a strong dependence on the undercooling for both terrestrial and microgravity conditions (Fig. 2.6b). These findings support previous experimental research on PVA done by Rubinstein and Glicksman [105], which also questions the theories of dendritic growth. The relatively high anisotropy ($\approx 2-5\%$) of PVA has been pointed out as the probable cause of the disagreement with theories of dendritic growth.

Muschol et al. [96] measured the strength of the surface tension anisotropy for SCN and PVA. Then, they compared the predictions of the selection parameter by microscopic solvability theory (MST) to the experimental data available in the literature. They concluded that the existing data do not completely validate the MST (Fig. 2.7). They suggested that such disagreement might be caused by kinetic effects on the experiments, competition among dendrites during the experiments or oversimplifications in the model for material with fourfold-symmetry.

2.2.4.2 Alloys studies

As far as the free dendritic growth of binary alloys is concerned, Kahlweit [54] and Chan et al. [22] studied experimentally the dendritic growth of NH_4Cl crystals in aqueous solutions. These works were mainly engaged with the observation that the protrusions or dendrite arms starting from a small spherical crystal along certain

directions were the only ones observable. The observed velocity and tip radius were never reported in these studies.

Only the data of Chopra et al. [23] appears to be available for direct testing of free dendritic growth theory of alloys. At different undercoolings and solute concentrations, these authors measured the tip velocity and tip radius of equiaxed dendrites for two alloy systems, namely SCN-argon and SCN-acetone. The studies with SCN-argon were limited to very dilute cases because the authors were interested in the region in the phase diagram where the liquidus line has a fairly constant slope. The first quantitative description of the SCN-ACE system, including a partial phase diagram in the region of interest, was made by Chopra et al. The authors also found that the equilibrium partition coefficient remains constant at a value of 0.1 for acetone concentrations of up to 25 mol %.

For SCN-acetone alloys, Chopra et al. [23] found that the dependence of tip velocity and radius on the undercooling for alloys, at constant compositions, is analogous to the trend observed for pure SCN dendrites. They also reported two different regimes of operation, one below a critical concentration of acetone (0.1% mol) governed by the heat transfer, and another above the critical concentration controlled by solute diffusion (Figure 2.8). Below the critical concentration the tip velocity increases with concentration. Above the critical concentration the opposite behavior occurs. Chopra et al. [23] also found a minimum for the tip radius at the critical concentration. This last finding contradicts the prediction of the LGK model. Chopra and coworkers argued that the disagreements with the LGK model were caused by lack of resolution in the measurement. Finally, a tip splitting instability was observed for the critical concentration.

As mentioned before, the Chopra's experimental benchmark for SCN-acetone [23] was reexamined by Li and Beckermann [84]. These authors found reasonable agreement between the Chopra's experiments and the LGK and LB models for concentrations below the critical value (0.1% mol). Specifically, the LB model

reproduces the tip velocity and radius data of Chopra (Figure 2.8). The LGK predictions are up to a factor of four lower for the tip velocity and up to factor of two higher for the tip radius. The agreement in terms of the Peclet number and the selection parameter, at concentrations below the critical value, is good for both models. Above the critical concentration (0.1% mol), there are significant differences between both models and the experimental data (Figure 2.9). They [84] reported more important discrepancies for the highest undercooling (0.9 K), where the natural convection effects are supposed to be small. Furthermore, the selection parameter is far from constant along the entire range of studied undercooling. These authors [84] concluded that convection cannot cause these disagreements because the observed trends are independent of the undercooling and they are not mitigated by increments in the solute concentration. Additionally, They [84] suggested that experimental difficulties might be responsible for the discrepancies between theoretical predictions and experiments.

Dougherty and Gollub [30] measured the selection parameter for a 51 wt % solution of ammonium bromide $(\mathrm{NH_4Br})$ in water. This experimental study showed good agreement with the microscopic solvability theory; the reported value for the selection parameter $(\sigma^* = 0.081)$ was close to the theoretical prediction $(\sigma^* = 0.065)$. Maurer and coworkers [93] studied aqueous solutions of ammonium bromide solidifying within a gel. They used few weight percents of a gelifying agent called tetramethoxysilane (TMOS). This agent does not change the mass diffusivity for the concentrations of ammonium bromide studied. Maurer et al. [93] verified the invariability of the mass diffusivity using optical techniques. The selection parameter reported in this investigation $(\sigma^* = 0.114)$ differs from the theoretical prediction of the three-dimensional solvability theory $(\sigma^* = 0.057)$ by a factor of 2. In the case of the coefficient A_4, the measured value $(A_4 = 0.0024)$ is about five times smaller than the solvability prediction $(A_4 = 0.0104)$. Maurer and coworkers [93] did not provide information about the fitting range used to measure the coefficient A_4. Additionally, they claimed that the presence of the gel

reduces convection and boundary effects. Ideally, the absence of such effects should bring the experimental results closer to microscopic solvability predictions. However, the measured selection parameter shows the opposite trend. No explanation was provided about this.

Dougherty and Lahiri [33] studied the morphology of dendrites growing in an aqueous solution of ammonium chloride (36 wt %). For an undercooling of 0.77 K, the shapes of the dendrite were fitted to a fourth order polynomial. The fitting range was extended six tip radiuses behind the tip in order to measure the coefficient A_4. The value obtained $\left(A_4 = 0.004\right)$ matched the measurements by Glicksman and coworkers [73] and simulations by Karma et al. [58-59]. Other kinds of regression, such as parabolic and power law, were also attempted. However none of these performed as well as the fourth-order polynomial. Finally, Dougherty and Numally [34] studied the transient dendritic growth in an aqueous solution of ammonium chloride (38 wt %). They found that the selection parameter remains constant for very smooth changes in temperature. The period of temperature change needs to be larger than the time scale R/V in order to keep the selection parameter constant.

It is important to note that experimental data available for aqueous solutions [29-34] are not as complete as the benchmark by Chopra and coworkers [23]. Nonetheless, the solutions experiments [29-34] indicate a reasonable agreement with the solvability theory, which is really promising. Unfortunately, the universality of the coefficient A_4 cannot be confirmed from the comparison between the measured values for solutions and pure substance because they are not based on the same fitting range.

Pioneer experimental attempts [96] for verifying the MST had been unsuccessful because of the intrinsic difficulties in the measurements of the free surface energy and its anisotropy in metals. However, substantial advances have been recently achieved in order to overcoming such inconveniences [97-98]. Besides, some recent measurements carried

out by Liu et al. [90] using an Al-4%Cu alloy under conditions of diffusion controlled solidification validate the MST.

2.2.5 Numerical simulations

Further analytical advances in the study of free dendritic growth are rather challenging. The inclusion of anisotropic surface energy increases considerably the mathematical complexity of the solidification problem. Under such circumstances, numerical methods are an invaluable tool to study free dendritic growth. In addition, the scarcity of experimental benchmarks increases the need for realistic simulations. Only the multiscale nature of dendritic growth has delayed quantitative studies based on numerical simulations. Fortunately, several breakthroughs in the phase-field methodology have made possible quantitative tests for the theories of dendritic growth. In the next subsections, such advances are briefly reviewed.

2.2.5.1 Phase-field model for pure substances

With the tremendous increase of computer power over the last thirty years, numerical methods have evolved as a reliable means to solve free-boundary problems. The phase-field method has become a powerful numerical method in past decades to model microstructure formation. Its advantage lies in the fact that it avoids the difficulty of tracking a sharp, complex interface by introducing one or more phase-field variables to distinguish different phases. This method was first developed by Fix [37] and Collins and Levine [24] for an isotropic system. Since then, many different phase-field models have been developed to model the solidification of pure melt (Sekerka et al. [107]; Karma and Rappel [58-60]; Kobayashi [67]), binary (Wheeler, Boettinger, and McFadden [122-123]; Caginalp and Xie [21]; Warren and Boettinger [121]), eutectic (Karma [56]; Elder et al. [36]), peritectic (Tiaden et al. [113]) and directional solidification (Grossmann et al. [45])

Karma and Rappel [58-60] developed the thin-interface limit of phase-field equations which has been successfully used in quantitative tests of microsolvability

predictions. A good agreement in terms of the selection parameter has been observed between the simulations and the solvability theory over a wide range of low crystalline anisotropies. However, poor agreement is observed for PVA (Fig 2.10a).

Furthermore, Karma and coworkers [58-60] studied the morphology of three-dimensional dendrites using the phase-field method. These authors found that the coefficient A_4 is almost independent of the surface energy anisotropy strength and the applied undercooling for fitting ranges between eight and ten radii behind the dendrite tip (Figure 2.10b). Moreover, simulation results $(0.004 \leq A_4 \leq 0.005)$ agree quantitatively with experiments by Glicksman et al. [73] $(A_4 = 0.004)$ for a fitting range between four and ten tip radii behind the tip. Conversely, predictions of the phase-field simulations are half of the size of the one corresponding to MST $(A_4 = 0.0104)$. In addition, these authors suggested that the actual tip radius is not measurable, because of the tip distortion for material with fourfold-symmetry. They proposed the curvature radius associated with the best parabolic fitting of the tip as an alternative. Such curvature radius should be equal to the Ivantsov tip radius in most cases except for low undercoolings.

Finally, Lu et al. [92] studied the effects of melt convection on the dendrite morphology using the phase-field method. These simulations show that the dendrite shape remains universal under the studied flow conditions. The predicted values of A_4 were around 0.004 for a fitting range of four radiuses behind the tip. Because of computational limitations, A_4 was not predicted for larger fitting range. However, the trends observed for the reported fitting ranges suggest that A_4 would remain in the vicinity of 0.004 for larger fitting ranges.

2.2.5.2 Phase-field model for alloys

The findings of microscopic solvability theory have been confirmed by phase-field simulations (Karma and Rappel [59]; Provatas et al. [102]). Previous studies with the phase-field method (Warren and Boettinger [121]; Danan et al. [26]; Tiaden et al.

[113], Beckermann et al. [6]; Kim et al. [66]; Suzuki et al. [111]) have not solved the energy equation for binary alloy solidification problems, but have made some suitable assumption for the temperature, that is, isothermal field, temperature constant in space but time-varying, "frozen gradient", etc. Loginova et al. [91] studied non isothermal binary alloy solidification with the phase-field method. However, the authors report the presence of abnormally high solute-trapping and interface thickness-dependent results. Lan et al. [76-77] in their work included this model with an adaptive finite volume mesh that allows for the dendrites to grow without the thermal boundary layer reaching the boundaries. However, with interface thickness and solute-trapping Lan et al. [76-77] reported the lack of convergence of results. Karma [55] effectively addressed the problem of abnormally high solute-trapping in phase-field simulations of alloy solidification, with the introduction of the concept of the solute anti-trapping current. In this regard, a solute flux term is added to the species conservation to counterbalance the spurious solute-trapping effect associated with the sharp variation of solute diffusivity across the interface. This concept was later adopted by Lan and Shih [77] to perform phase-field simulations of non-isothermal free dendritic growth of a binary alloy in a forced flow.

Ramirez and Beckermann [103] used two-dimensional phase-field simulations to test the LGK and LKT models for alloys. They found that the transport heat and species are accurately predicted by these models (Figure 2.11a). Conversely, the selection criterion fails at two respects. First, the computed selection parameter depends strongly on applied undercooling (Figure 2.11b), solute concentration (Figure 2.11c) and Lewis number. Second, a minimum in the selection parameter is observed for the critical concentration, where both thermal and solutal transports are important. Besides, simulated tip velocity does not have a pronounced maximum. Finally, the corrections included in the LKT model to account for high Peclet number were found ineffective.
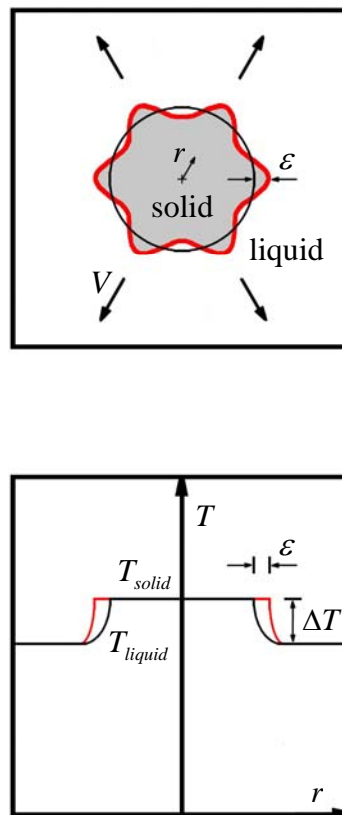
Figure 2.1: Stability of the solid-liquid interface during equiaxed solidification of pure material. Kurz and Fisher [71] argued that the solid-liquid interface is morphological unstable because perturbations make the temperature gradient steeper allowing a higher rejection of latent heat at the interface peaks. These authors reached this conclusion by comparing the temperature profiles for perturbed (red line) and unperturbed (black line) interfaces. This analysis was carried out assuming that there is no temperature gradient in the solid phase.
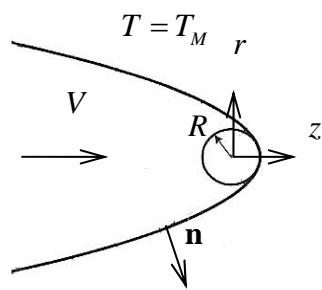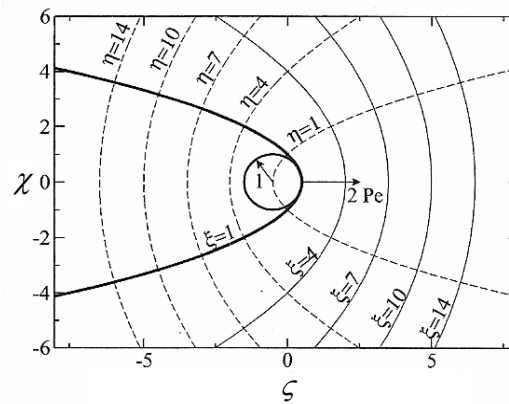
Figure 2.2: Ivantsov paraboloid in several coordinates systems [27].
    (a) Cartesian coordinates
    (b) Paraboloidal coordinates

(a) (b)
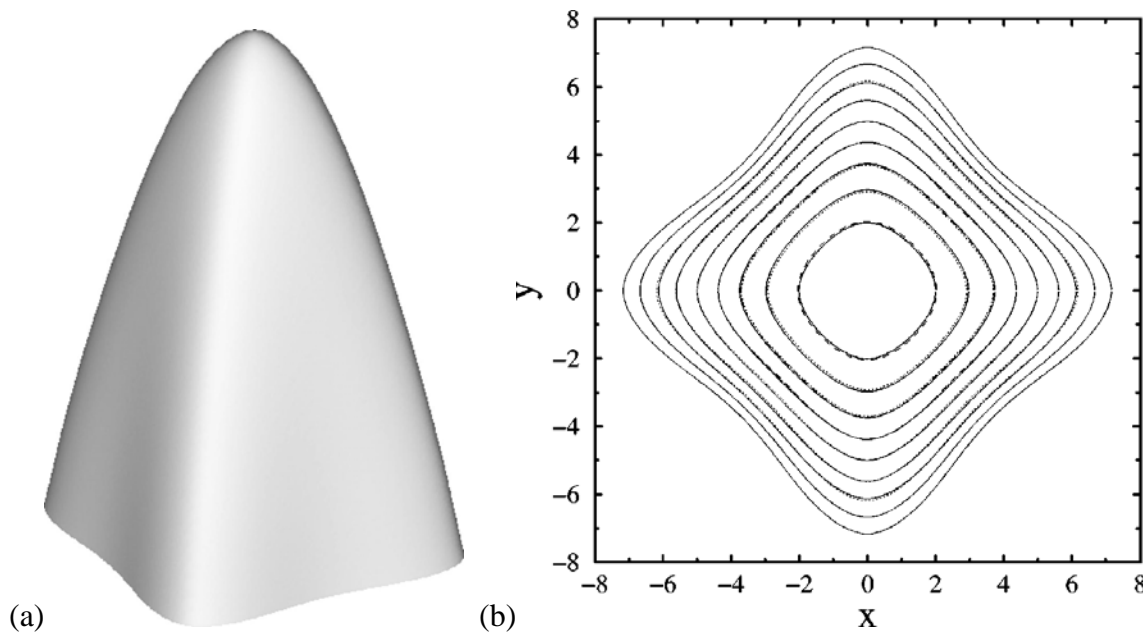
Figure 2.3: Non-axisymmetric needle crystal [58]
    (a) Isometric view
    (b) Level curves
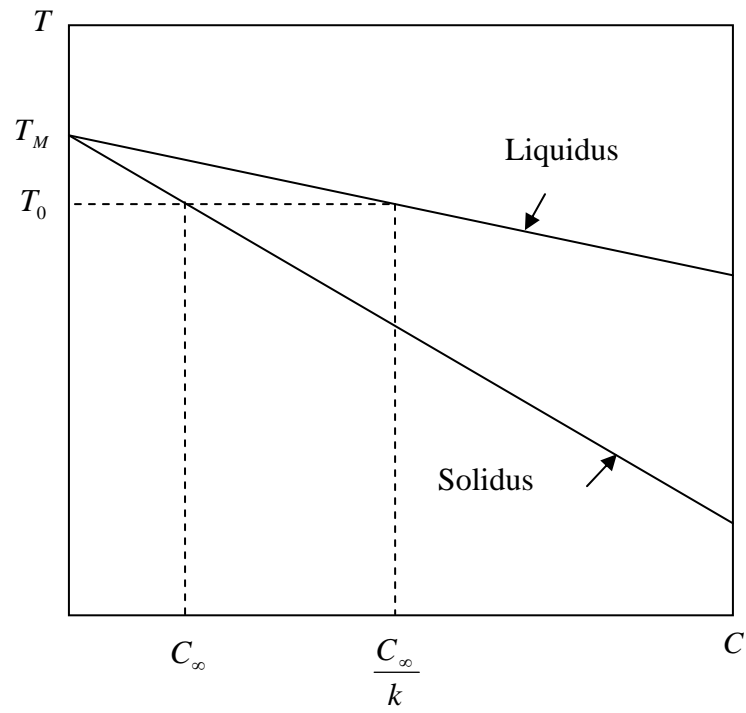
Figure 2.4: Phase diagram for a binary alloy.
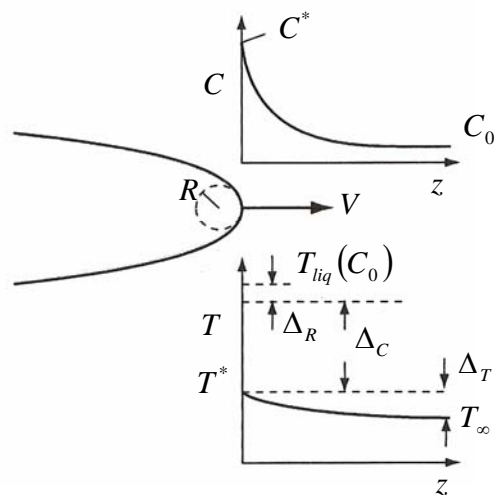
Figure 2.5: Concentration and temperature profiles in the liquid phase according to LGK model [87-88]. The total undercooling in the liquid (ΔT) results from three different contributions: capillary undercooling (Δ_R), solutal undercooling (Δ_C), and thermal undercooling (Δ_T).
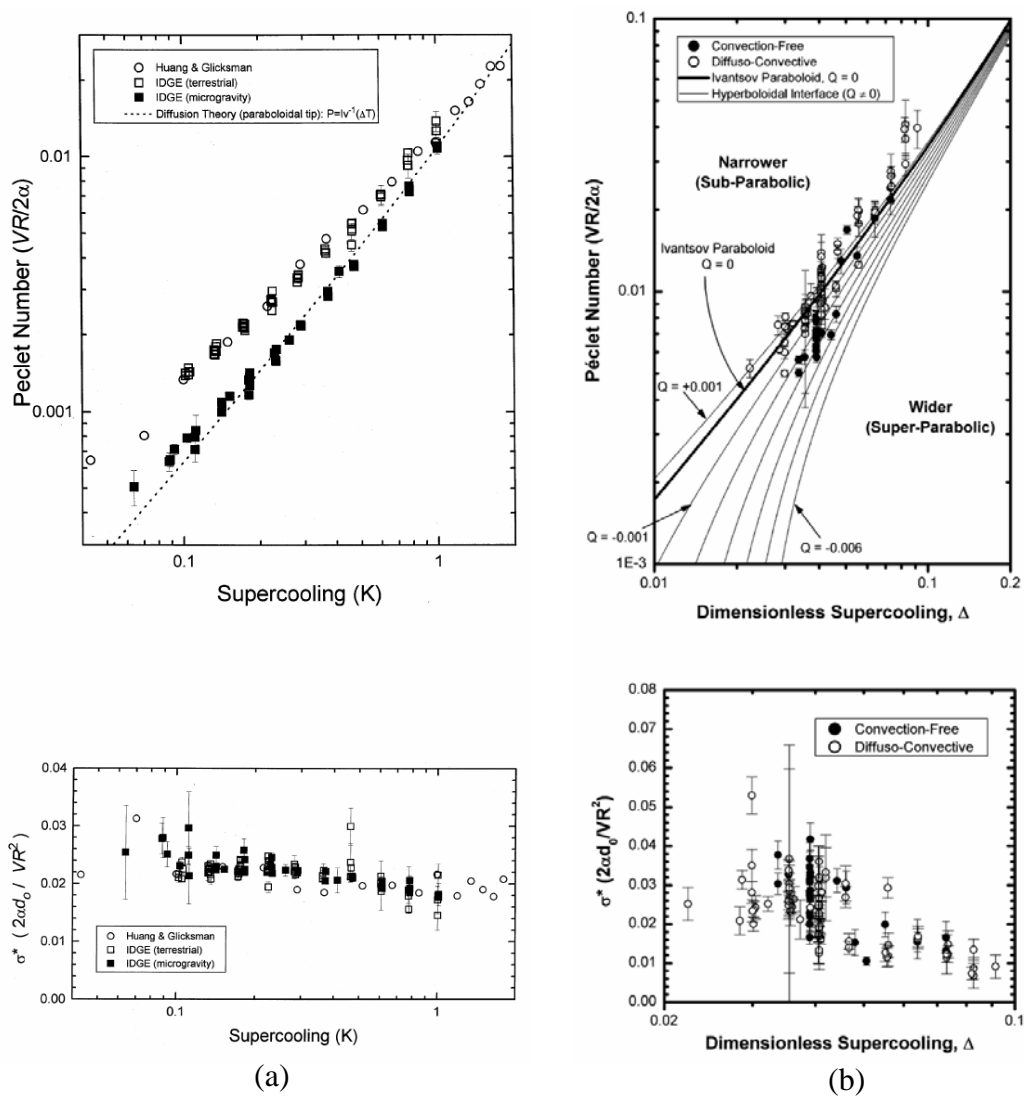
Figure 2.6: Results from the isothermal dendritic growth experiment
    (a) Data for SCN [69].
    (b) Data for PVA [75].
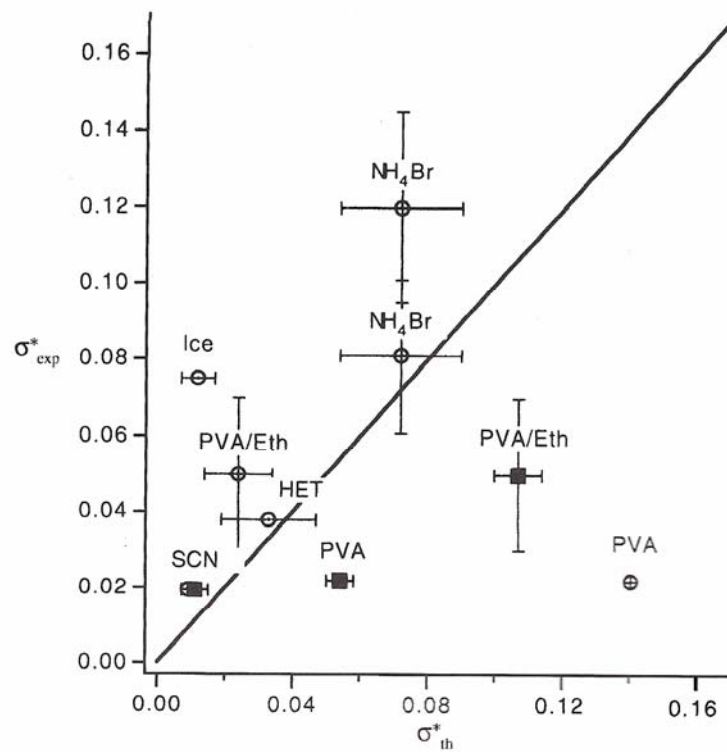
Figure 2.7: Comparison of the MST predictions and experimental benchmarks in terms of the selection parameter [96].
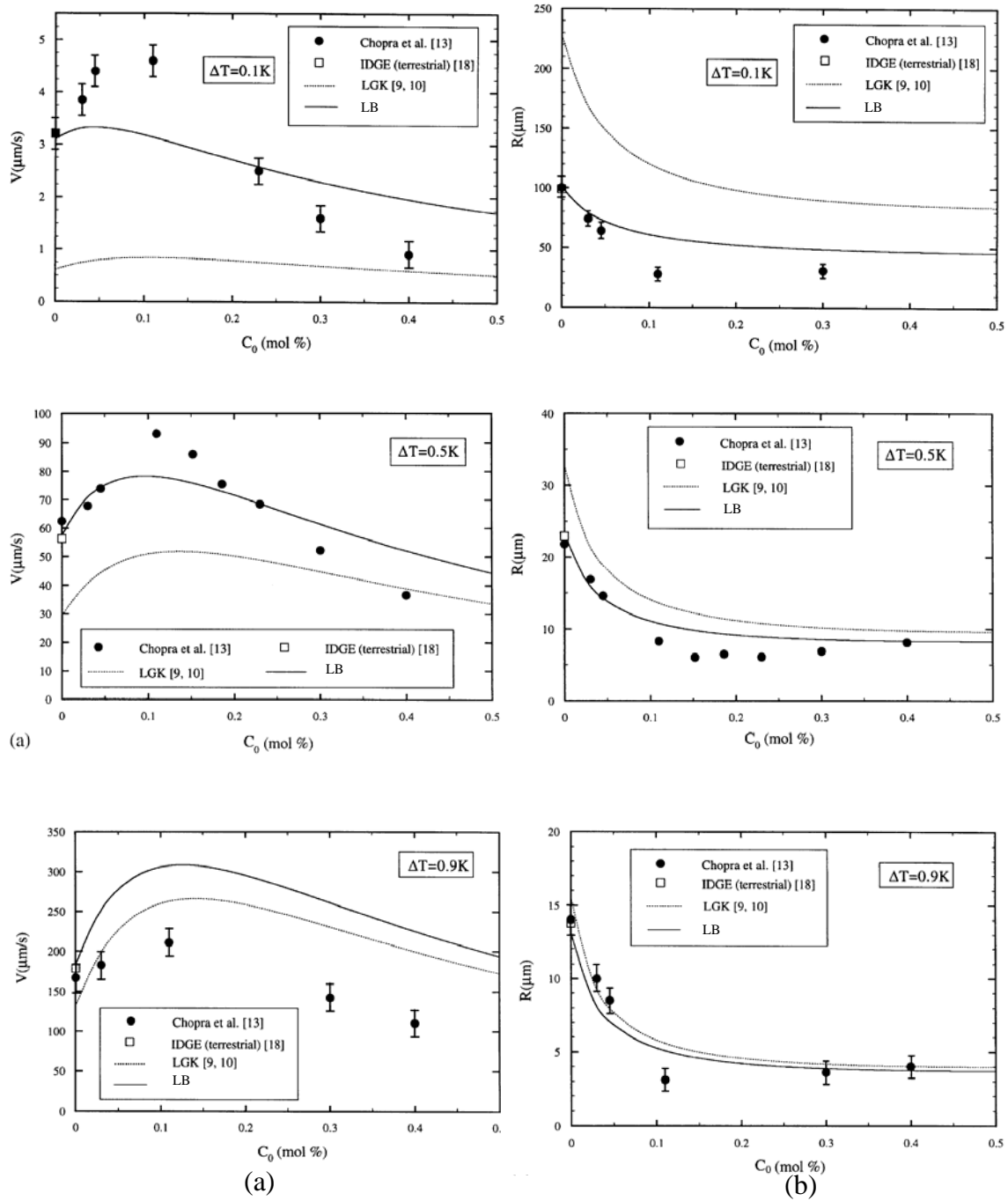
Figure 2.8: Validation of LGK [87-88] and LB [84] models using the experimental data
reported by Chopra et al. in terms of tip velocity and radius [23]
(a) Comparison in terms of tip velocity.
(b) Comparison in terms of tip radius.
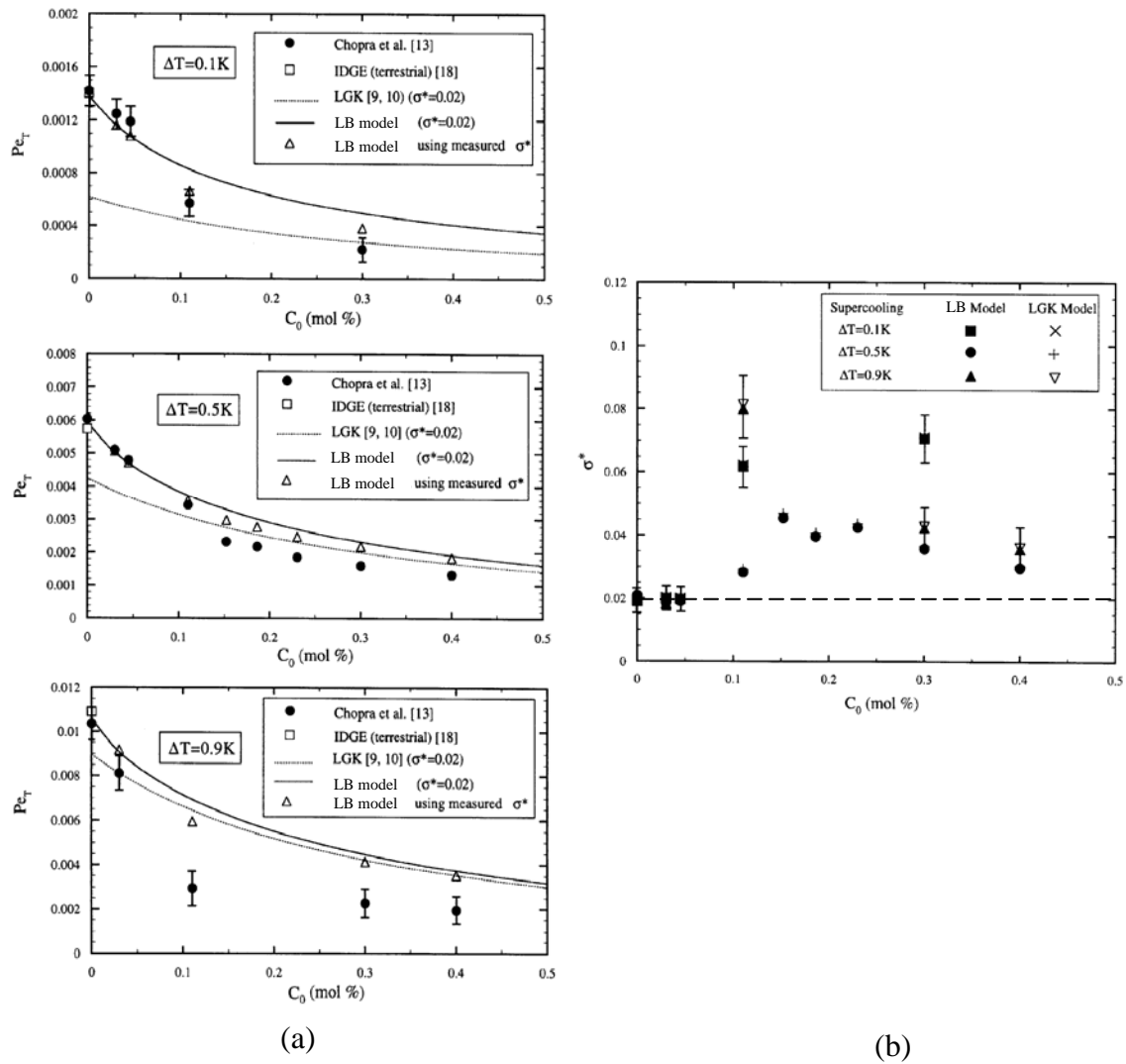
Figure 2.9: Validation of LGK [87-88] and LB [84] models using the data reported by
Chopra et al. in terms of Peclet number and selection parameter [23]
(a) Comparison in terms of Peclet number.
(b) Comparison in terms of the selection parameter.

(a)

(b)

(c)
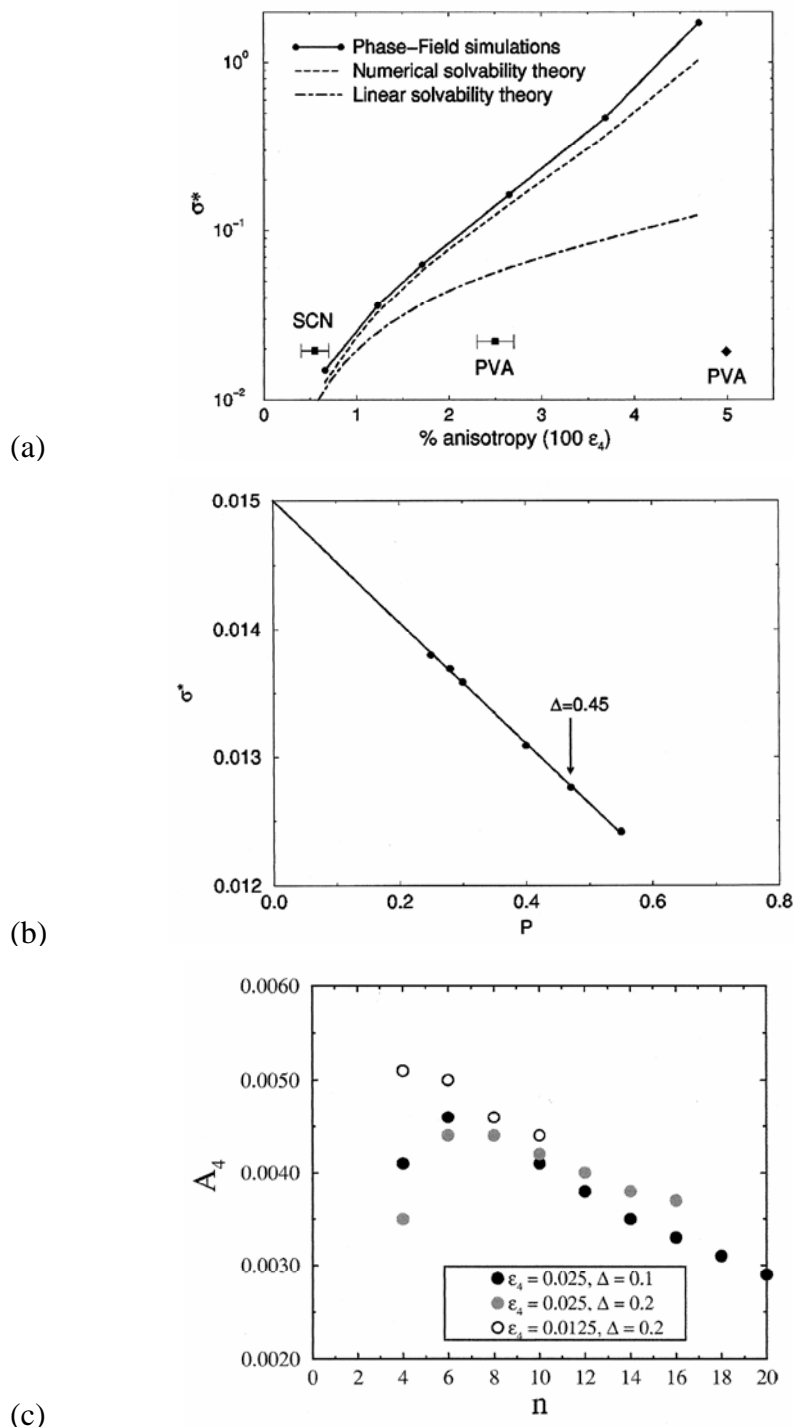
Figure 2.10: Phase-field simulations predictions for free dendritic growth of pure substances
   (a) Selection parameter as a function of the anisotropy strength [60].
   (b) Selection parameter as a function of Peclet number [60].
   (c) Coefficient A_4 as a function of the fitting range [58].

(a)

(b)

(c)
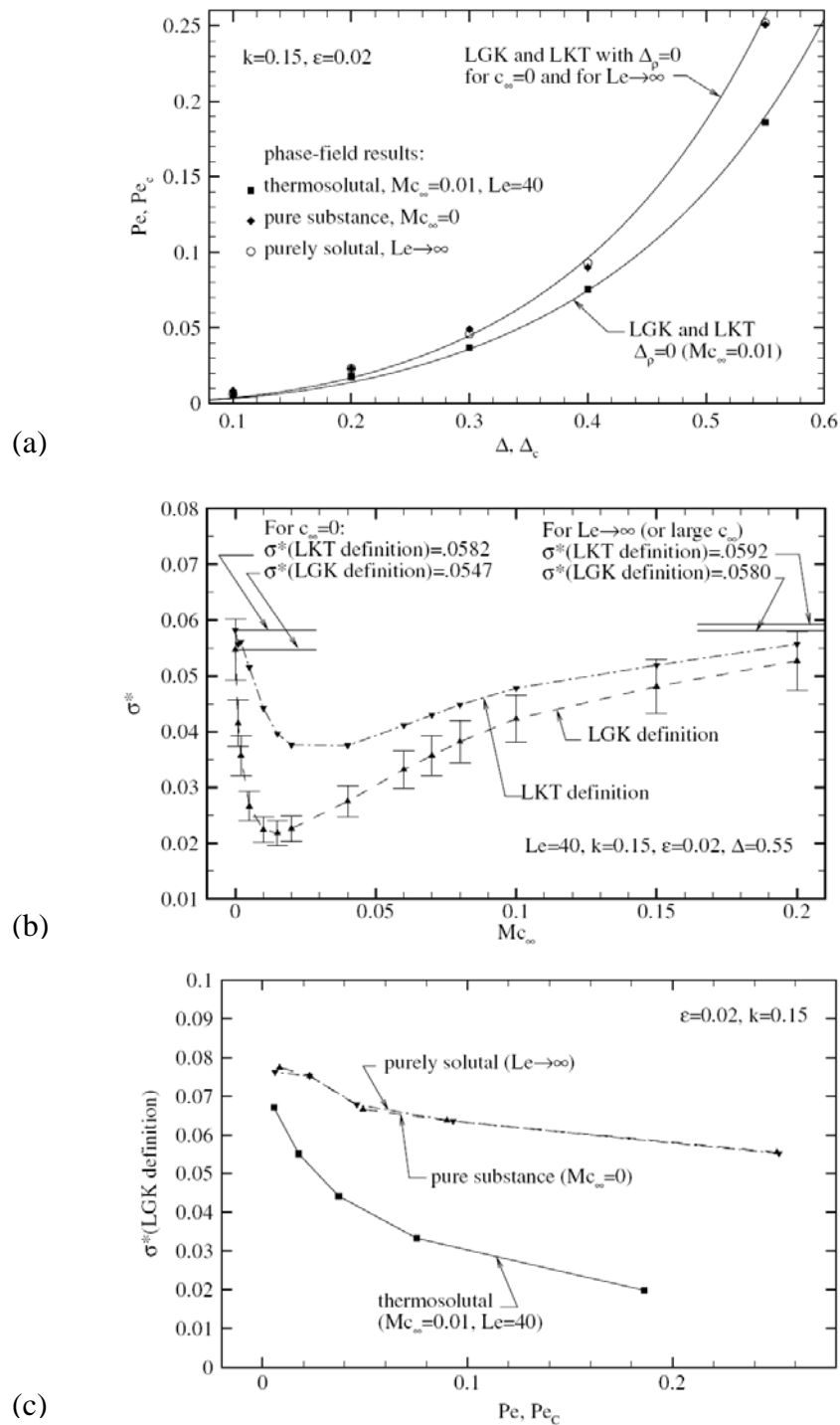
Figure 2.11: Phase-field simulations predictions for free dendritic growth of alloys [103]
    (a) Peclet number as a function of thermal and solutal undercooling.
    (b) Selection parameter as a function of the solutal undercooling.
    (c) Selection parameter as a function of the Peclet numbers.

CHAPTER III

METHODOLOGY

3.1 Introduction

As discussed in Chapter I, a thorough understanding of free dendritic growth is required to prevent internal defects and to improve physical properties of casting parts. Furthermore, the literature review in Chapter II shows that stationary free dendritic growth of alloys is not fully understood yet. Specifically, there are important disagreements between theoretical models and the experimental benchmark of Chopra and coworkers [21], which is the only one available in the literature. The aim of the current research, as stated in Chapter I, is to provide new experimental benchmark for succinonitrile-acetone alloys and to validate the existing models for free dendritic growth for alloys. These transparent materials solidify as body centered cubic metals do. In addition, their refraction index varies substantially during solidification permitting visual examinations of dendrites and other microstructures. The equiaxed dendritic solidification experiment (EDSE) takes advantage of these characteristics, and allows photographing the dendritic growth process in two orthogonal views. Using both sequences of photos, the growth velocity and the dendrite morphology were obtained. In the next sections, the followed research plan, the EDSE setup and the experimental techniques employed in the present research are briefly described.

3.2 Objectives

The main objectives of the present investigation were:

- To validate existing theoretical models of free dendritic growth by studying the dependence of the tip velocity (V), the tip radius (R), the Peclet number (Pe),

the selection parameter ($\sigma*$) and the coefficient A_4 on the undercooling and the solute concentration.

- To characterize the sidebranching of pure succinonitrile and succinonitrile-acetone dendrites in terms of the dendrite envelop, the projection area and contour length

- To compare the new experimental data with previous experimental results for free dendritic growth of pure substances and alloys

- To provide new benchmark experimental data for free dendritic growth of pure substances and alloys, intended for validation of theoretical and numerical models.

3.3 Scope

The present investigation was focused on stationary free dendritic growth. Dilute alloys were studied experimentally. Specifically, succinonitrile-acetone alloys were working materials. Undercoolings ranging from 0.1 K to 1.0 K were studied. The acetone concentration was varied from 0.0086 mol % through 0.4976 mol %.

3.4 Plan of Research

Considering the scope presented above, the current investigation was organized in the following stages:

3.4.1 Experiments with Almost Pure Succinonitrile

This set of experiments was used to evaluate the setup and the methodology employed in this investigation. The specific goal of these experiments was to corroborate the trends reported by Glicksman and coworkers [69] in their terrestrial experiments with pure succinonitrile. Such comparison were carried out in terms of tip velocity, tip radius, Peclet number and selection parameter. Ten different undercoolings between 0.1 K and

1.0 K were studied. The experiments for undercoolings of 0.1 K, 0.5 K, 0.8 K and 1.0 K were duplicated to verify the repeatability of the results.

3.4.2 Experiments for Succinonitrile-Acetone Alloys

A new experimental benchmark for free dendritic growth of succinonitrile-acetone alloys was obtained. Only dilute alloys with solute concentrations less than or equal to 0.4976 mol % were studied. Five different concentrations, including almost pure succinonitrile, were investigated. For each concentration, six different undercoolings were studied. These undecoolings will range between 0.1 K and 0.7 K. Each experiment was repeated between two and five times. The specific objective of this stage was to verify the trends reported by Chopra and coworkers [21]. Again, comparisons were performed in function of tip velocity, tip radius, Peclet number, and selection parameter.

3.4.3 Tests to Models of Dendritic Growth for Alloys

The experimental benchmark for alloys obtained in the previous stages were compared with predictions of the LGK [81-82] and LB [78] models. This validation study was expected to address the discrepancies among Chopra's benchmark [21] and existing model for dendritic growth of alloys. As usual, the validation study were carried out in function of tip velocity, tip radius, Peclet number and selection parameter.

3.5 Experimental Setup

The EDSE setup, portrayed in Figures 3.1 and 3.2, was composed of three major groups of elements: optical equipments, isothermal bath, and growth chamber. The solidification process occurred in the growth chamber, which was located inside of the isothermal bath. Consequently, melting and solidification processes could be controlled by the isothermal bath. During the experiments, dendrite photographs and videos were obtained through the optical equipments. Figure 3.1a illustrates schematically the optical

elements of the EDSE setup. On the other hand, the isothermal bath and the growth chamber are sketched in Figure 3.1b.

Specifically, the optical equipment used consisted of two CCD cameras, a lens array, a lamp and an LED. The CCD cameras had different specifications. One was a high-resolution high-speed (up to 15 fps) monochrome progressive scan CCD camera, and from now on it will be referred as the "high resolution camera." The other was a color video CCD camera, and this will be referred as the "low resolution camera." The dendrite contour was obtained from the high resolution camera. Both cameras provided the angular orientation of the dendrite in their respective planes. The growth direction with respect to gravity was obtained from these two angles. A LED was the light source for the monochrome progressive scan camera, while a tungsten lamp (6.25V / 2.75A) illuminated the low resolution camera. An lens array increased the resolution of the monochrome progressive scan camera to 3.24 µm/pixel.

The main functions of the isothermal bath were melting and undercooling the material inside the growth chamber. The cylindrical wall of the isothermal bath was made of polymethyl-methacrylate. This tank had four optically polished windows, which prevent any optical aberration originated by the curvature of the tank wall in the images registered by the cameras. The fluid filling the tank was mixture of ethylene glycol and water at 70 v/v %. Such mixture was adopted as a working fluid because its refraction index matches the one corresponding to liquid SCN. An electrical heater located in the bottom of the tank was used to increase the temperature of the bath. Four thermistors, with resolution of $\pm$ 0.001 K, were installed inside the tank to monitor the temperature of the working fluid. The thermistor signals were input into a data acquisition system and an on-off controller. This latter device regulated electricity supply of the heater and kept the temperature of the bath around the set point. Finally, a stirrer made uniform the temperature inside the tank. The entire system maintained the temperature of the working fluid within $\pm$ 0.003 K around the set point.

As seen in Figure 3.1b, the growth chamber can be divided into several elements: the spherical compartment, the stinger, the void compensator, the valve and the acetone reservoir. The spherical portion of the chamber contained the studied materials (SCN or SCN-ACE); the solidification process occurred in this region. During the manufacturing of the chamber, the spherical section was filled with 70 cm^3 of almost pure SCN (0.0086 mol. %), and vacuum sealed at an absolute pressure of 0.2 bars. In order to study SCN-ACE alloys, some acetone had been added to the initially pure SCN. The acetone supply came from the cylindrical reservoir shown in Figures 3.1b and 3.2. This reservoir was connected to the chamber through a valve, which controlled the flow of acetone toward the chamber. With the purpose of controlling the location of the dendrites inside the chamber, a capillary tube (the stinger) was inserted inside the spherical portion of the chamber. The external extreme of the stinger was closed, keeping the chamber sealed. Conversely, the internal end of the stinger was open. By means of a thermo-electrical cooler located on the external portion of the stinger, the dendrites started to grow inside the stinger and propagated towards the interior of the chamber through the open end. Finally, the void compensator was an empty portion of the growth chamber, which allowed the expansion of melted material.

3.6 Experimental Procedure

Before each dendritic growth experiment, the isothermal bath temperature ws set up at 58.9 °C. The bath was maintained at this temperature until the SCN or SCN-ACE alloy inside the chamber completely melted and the gradient of solute concentration disappeared. In the case of pure SCN, a period of 2 hours was required to melt the material inside the chamber. For alloys, it took 12 hours for melting the material and the achievement of a uniform solute concentration inside chamber. Once the appropriated waiting period ended, the bath temperature was then reduced to the desired undercooling. It took roughly an hour to reach a uniform temperature inside the chamber. After this

second pause, the thermoelectrical cooler was turned on with the purpose of generating a dendrite inside the stinger. The dendrites grew down the inside of the stinger, until they reached the spherical compartment and started growing freely near the center of the chamber.

Once inside the spherical portion of the chamber, each dendrite underwent a transitory period before reaching the stationary growth velocity, which was maintained until the dendrite thermal field interacted with the chamber walls (Figure 3.3a). The video recording and photograph taking were initiated when the selected dendrite left the stinger, and they were stopped when the tip of the dendrite grew out of the cameras' view. Generally, the crystallographic preferred directions did not coincide with the normal vectors to the camera planes. Because of this misalignment, the actual contour of the dendrite could be registered. This inconvenience was solved by rotating the growth chamber until the crystallographic preferred directions coincide with the normal vectors to the camera planes. Photos collected during the alignment period were discarded.

In the next section, the methodology for analyzing dendrite photos is presented. Note that an additional experimental procedure was required to measure the melting point of the alloy inside the chamber after each increment in the solute concentration. For simplicity, such procedure was omitted in this section. However, the liquidus temperature measurement is discussed in the Appendix A.

3.7 Data Analysis

Digital photographs and video recordings constitute the primary data registered during this experimental investigation. The growth velocity, tip radius, the coefficient A_4, dendrite envelop, projection area and contour length were measured from these photos and videos. Then, the Peclet number and the selection parameter were estimated from the measured tip velocity and radius. These processes of measurement and estimation are described in the next sub-sections.

3.7.1 Measurement of Growth Velocity

The growth velocity as a function of time was obtained from photographs and video recording using the following procedure:

- First, the dendrite's contour was obtained in both cameras' planes applying a Laplacian of the Gaussian filter to the sequences of photos and video snapshots recorded during each experiment. While filtering, the locations of the lowest point in the dendrite's contour were registered as a function of time.

- Next, the coordinates of the lowest point in the dendrite's contour in each plane, (X_α, Z_α) and (X_β, Z_β), were regressed to straight lines:

$$Z_\alpha = m_\alpha X_\alpha + b_\alpha \quad Z_\beta = m_\beta X_\beta + b_\beta \qquad (3.1)$$

- Thereafter, the growth angles in the camera planes (α, β), measured respect the vertical axis, were obtained from the slopes of the regressions obtained in the previous step:

$$\alpha = \tan^{-1}\left(-1/m_\alpha\right) \quad \beta = \tan^{-1}\left(-1/m_\beta\right) \qquad (3.2)$$

- Then, the eulerian growth angle with respect to gravity (θ) was calculated from the growth angles in the camera planes (α, β) as follows:

$$\tan(\theta) = \sqrt{\left(\tan(\alpha)\right)^2 + \left(\tan(\beta)\right)^2} \qquad (3.3)$$

- Subsequently, the dendrite tip position as function of time was determined from the high resolution camera contour.

- After that, the vertical component of the transient growth velocity (V_z) was obtained using the following relationship:

$$V_Z = \Delta Z/\Delta t \qquad (3.4)$$

- Finally, the magnitude of the transient growth velocity (V) was determined from the Eulerian angle (θ) as follows:

$$V = V_Z / \cos(\theta) \tag{3.5}$$

The steady-state growth period for each experiment was determined from the graph of tip velocity as function of time (Figure 3.3a). In fact, the time interval corresponding to the plateau in growth velocity was considered the stationary period. Consequently, the stationary growth velocity corresponded to the average during the stationary period. In Figure 3.3 b, the instantaneous and stationary velocities were compared for a small group of experiments. Lastly, the uncertainty of the velocity measurements was estimated as follows:

$$\Delta V = \sqrt{\Delta V_0{}^2 + S_V{}^2} \tag{3.6}$$

where $\Delta V_0{}^2$ is half of the resolution of the velocity measurement, which was obtained from the specifications of the high resolution camera and the data acquisition system, and S_V is the standard deviation of velocity during the stationary growth period.

3.7.2 Measurement of Tip Radius and A_4

The sequence of photos coming from the high resolution camera was reexamined in order to characterize the dendrite's morphology. First, the photos were rotated and scale up using the growth angles so the full amplitude of the dendrite's ridges could be measured. Then, the dendrite's contours were obtained applying a Laplacian of the Gaussian filter. After that operation, the contours were translated to origin of the reference frame used, and the coordinates of the point in the contours (X, Z) were converted from pixels to microns. Next, these coordinates were regressed to the following fourth order polynomial using the robust fitting method [35]:

$$Z = c_1 X^2 + c_2 X^4 \tag{3.7}$$

where Z and X are the vertical and horizontal coordinates. On the other hand, the dendrite shape predicted by the MST is:

$$z = \frac{r^2}{2} - A_4 r^4 \cos(4\theta)$$
(3.8)

where r, θ and z are radial, azimuthal and vertical dimensionless coordinates. Since the dendrites were rotated during the experiment in such a way that $\theta = 0$, then:

$$z = \frac{r^2}{2} - A_4 r^4$$
(3.9)

Moreover, a further simplification is possible considering that the dendrite contour was aligned with the gravity direction:

$$z = \frac{x^2}{2} - A_4 x^4$$
(3.10)

where x is a horizontal dimensionless coordinate. This equation can be expressed in dimensional form using the tip radius (R) as scaling factor:

$$Z = \frac{1}{2R} X^2 - \frac{A_4}{R^3} X^4$$
(3.11)

Finally, the tip radius and the coefficient A_4 were obtained by comparing the fitting of the dendrite contour (Equation 3.5) to the prediction of the MST (Equation 3.9):

$$R = \frac{1}{2c_1} \text{ and } A_4 = -c_2 R^3$$
(3.12)

The regressions of the points in the dendrite's contours were carried out for fitting ranges between 2 and 11 radii behind the tip. Furthermore, the reported tip radiuses and coefficients A_4 correspond to average values throughout the constant velocity period for a fitting range of 10 radii behind the tip (Figure 3.4). Also, the uncertainty in the radius's

measurements due to the fitting (ΔR) were assessed as the absolute value of the difference between the average radiuses for the fitting ranges of 6 (R_{6R}) and 10 (R_{10R}) radii behind the tip:

$$\Delta R = \left| R_{6R} - R_{10R} \right| \tag{3.13}$$

Limitations in the resolution of our optical equipments motivated the adoption of this criterion. This issue is discussed in detail in Chapter IV. Finally, the standard deviation of the coefficient A_4 during the constant velocity period was reported as the corresponding uncertainty (Figure 3.5).

3.7.3 Calculation of the Peclet Number

The experimental Peclet number as a function of time was calculated substituting the data for tip velocity (V) and radius (R) in the following relationship:

$$Pe_T = VR/2\alpha \tag{3.14}$$

where α represents the thermal diffusivity of the studied material. As in previous analyses, the stationary value of the Peclet number corresponded to the average value during the steady-state period. In Figure 3.6, the transient and stationary Peclet numbers were compared for an individual experiment (Figure 3.6a) and a small subset of experiments (Figure 3.6b). In addition, uncertainty in the Peclet number was estimated from the uncertainties in tip radius and velocity using the sequential perturbation method.

3.7.4 Calculation of the Selection Parameter

The calculation of the selection parameter as a function of time for pure substances was straightforward. It only required substituting the experimental values of the tip velocity (V) and radius (R) in the following expressions:

$$\sigma^* = 2\alpha d_0/VR^2 \tag{3.15}$$

where α stands for the thermal diffusivity, and d_0 represents the capillary length.

In contrast, the estimation of the selection parameter for alloys based on the LB model could be rather complicated. Since modified Ivantsov functions depend implicitly on both temperature and concentration at the interface ($T*$ and $C*$), an iterative procedure is required to determine the selection parameter. This iterative approach was avoided using the regular Ivantsov functions. Several test cases were analyzed using both kinds of Ivantsov functions and the differences observed were negligible. Consequently, the usage of regular Ivantsov function was adopted. The calculation of the selection parameter as a function of time for alloys can be summarized as follows:

- Using the experimental values of tip velocity and radius, the Peclet numbers (Pe_C and Pe_T) were calculated as follows:

$$Pe_T = \frac{VR}{2\alpha} \text{ and } Pe_C = \frac{VR}{2D} \qquad (3.16)$$

- Then, the dimensionless solutal undercooling (Ω_C) was calculated using the regular Ivantsov solution:

$$\Omega_C = Pe_C \exp(Pe_C) E_1(Pe_C) \qquad (3.17)$$

- Finally, the selection parameter $(\sigma*)$ was determined using the approximation for low undercoolings:

$$\sigma* = \frac{d_0}{\rho}\left[2Pe_C\left(\frac{k\Delta T_0/(L_f/c_L)}{1-(1-k)\Omega_C}\right) + Pe_T\right]^{-1} \qquad (3.18)$$

In Figure 3.7, the transient and stationary selection parameters are compared for an individual experiment (Figure 3.7a) and a small subset of experiments (Figure 3.7b). As preceding subsections, the steady-state selection parameter corresponds to the average during the stationary period. Moreover, the selection parameter uncertainty was estimated from the uncertainties in tip radius and velocity using the sequential perturbation method.

3.7.5 Sidebranching Measurements

The sidebranching morphology was characterized using three parameters: the dendrite's envelope, the projection area (F) and the contour length (U). The dendrite's envelope is defined by the loci of the tips of all sidebranches growing actively. The projection area (F) corresponds to one half of the dendrite cross sectional area. The contour length (U) is the distance from the tip to any point of interest along the dendrite's border. All these parameters, shown in Figure 3.8, were measured as functions of the longitudinal distance from tip (z) using the dendrites contour obtained during the examination of the tip's morphology. First, the dendrite envelop was determined locating by hand the tips of all active sidebranches and fitting their coordinates (z and X_{act}) to a power law employing the least square method. Then, the integral parameters (F and U) were measured applying the particles analysis function of the image processing software ImageJ to the dendrite contours obtained from the high resolution camera. Such function is able to calculate the area and the perimeter of any close contour.
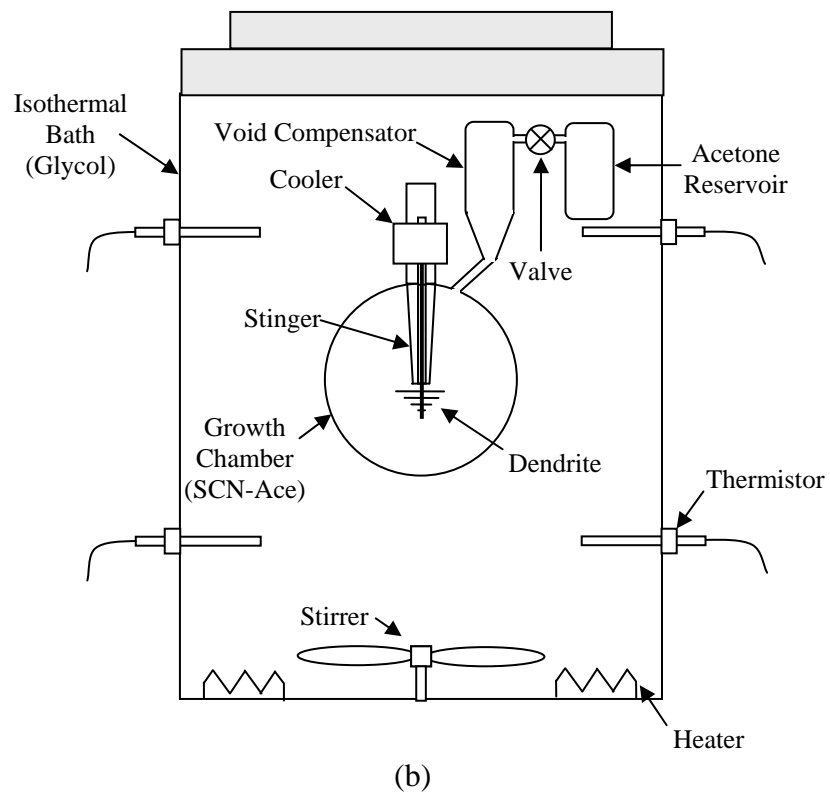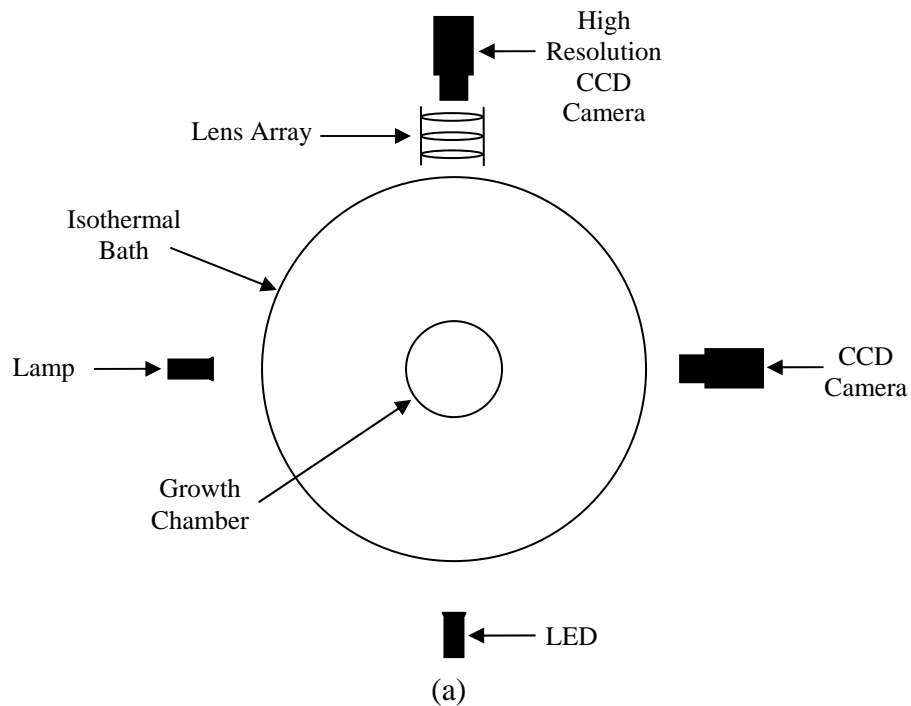
Figure 3.1: Schematic drawings of the Equiaxed Dendritic Solidification Experiment (EDSE) setup.
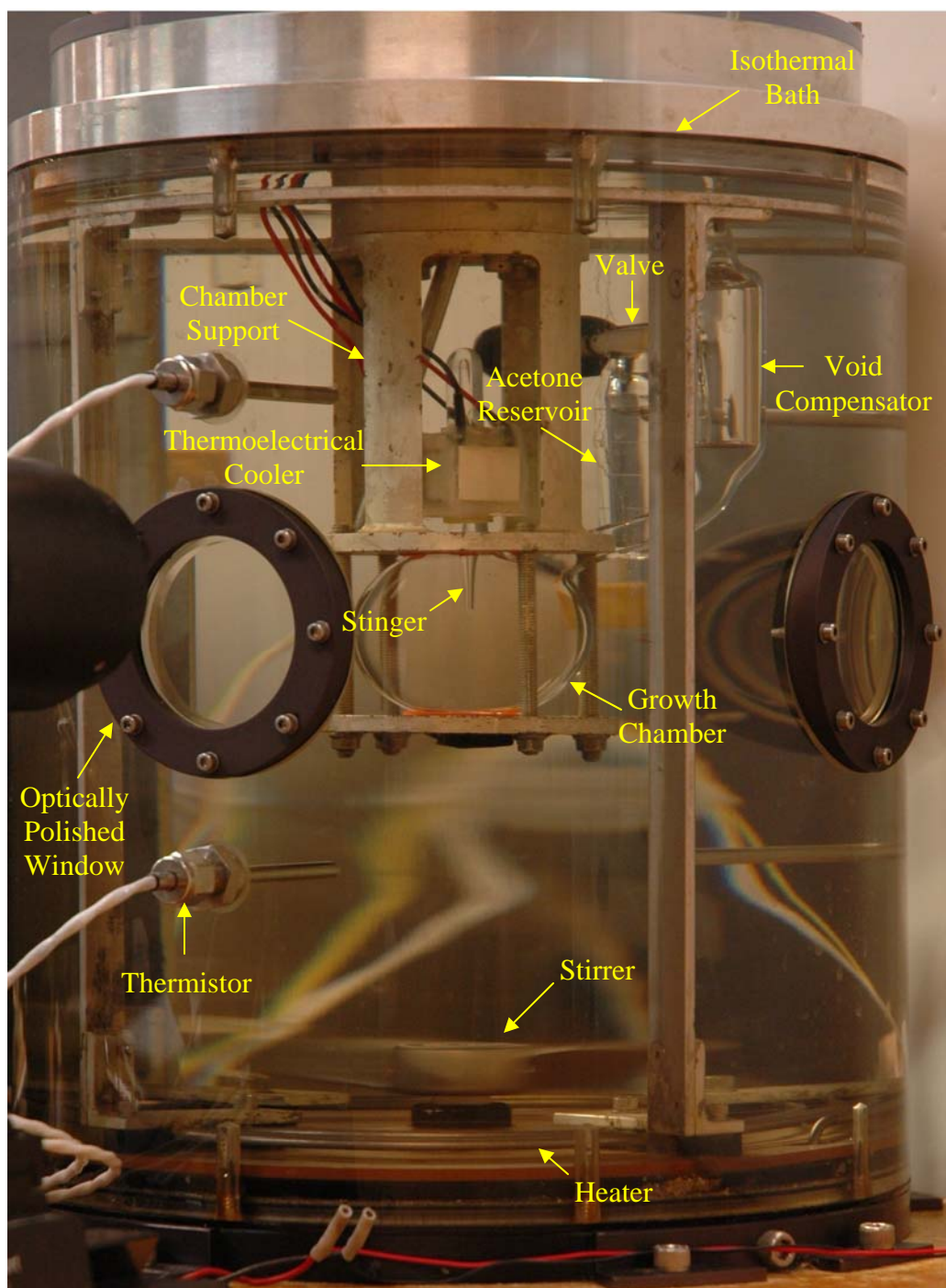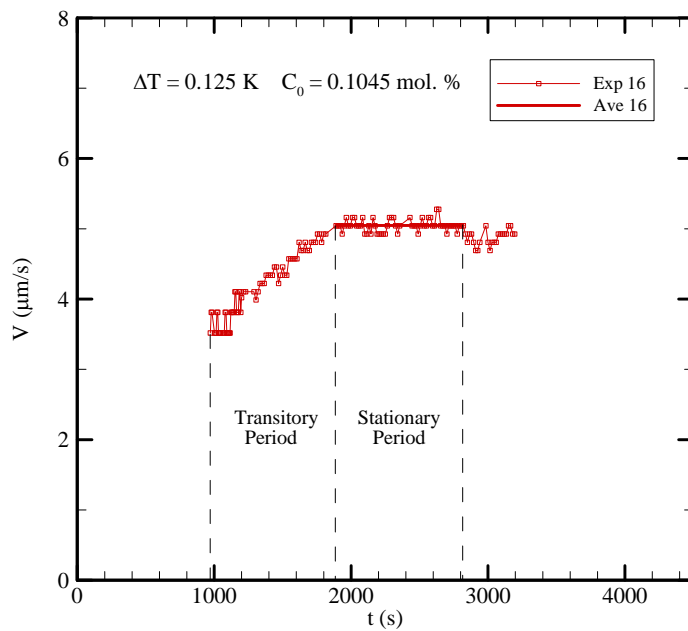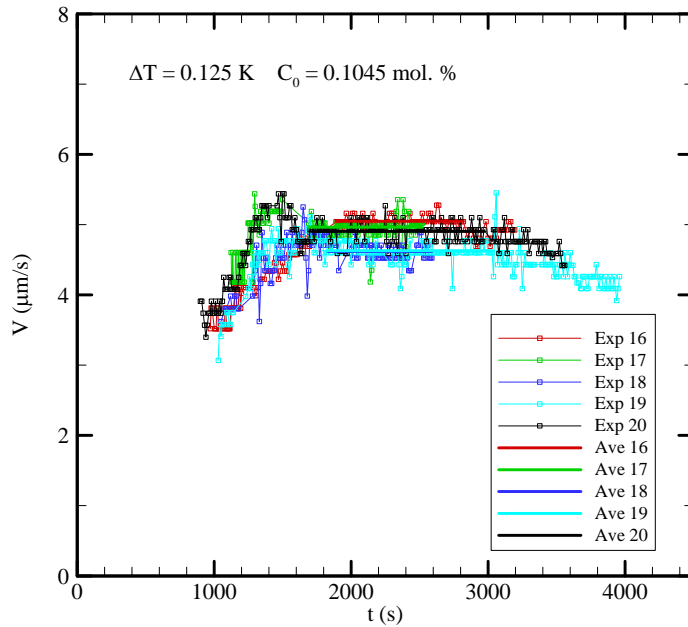(a) Top view.
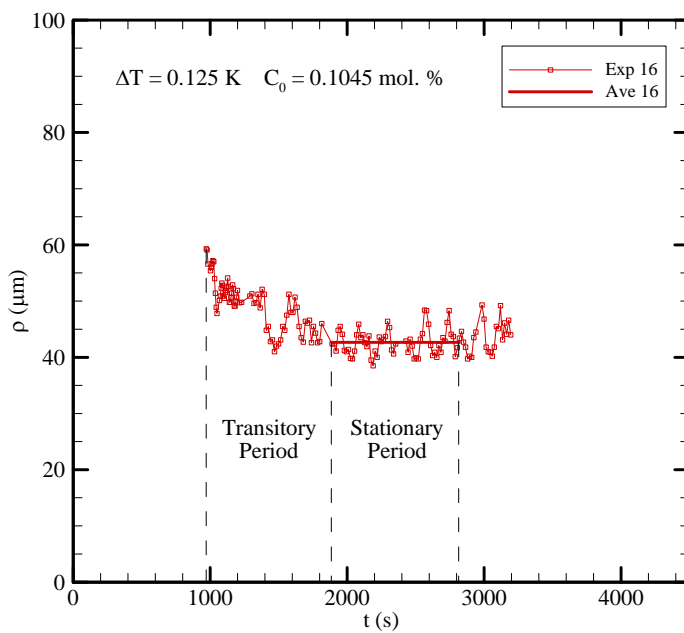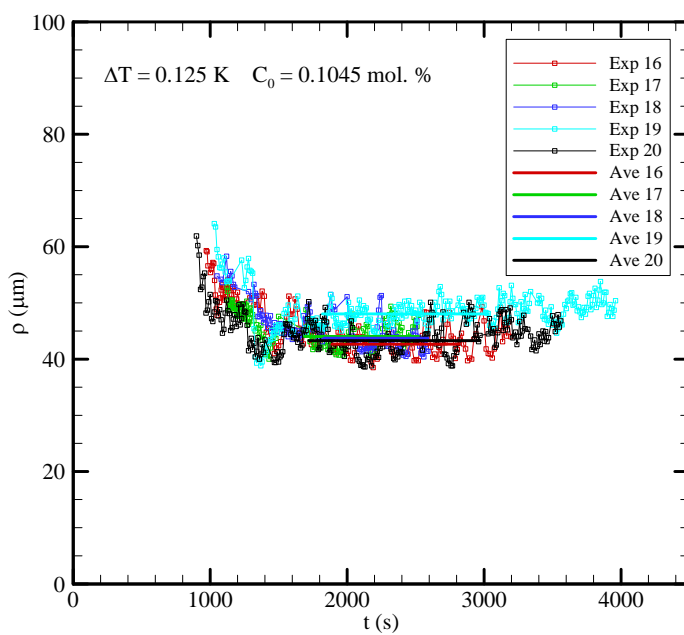(b) Side view.

Figure 3.2: Photo of the EDSE setup (side view).

(a)

(b)

Figure 3.3: Tip velocity measurement as a function of time.
(a) Single experiment for $\Delta T = 0.125\,\mathrm{K}$ and $C_0 = 0.1045$ mol. %
(b) Set of measurements for $\Delta T = 0.125\,\mathrm{K}$ and $C_0 = 0.1045$ mol. %.

Figure 3.4: Tip radius measurement as a function of time.

(a) Single experiment for $\Delta T = 0.125\,\text{K}$ and $C_0 = 0.1045$ mol. %

(b) Set of measurements for $\Delta T = 0.125\,\text{K}$ and $C_0 = 0.1045$ mol. %.

(a)
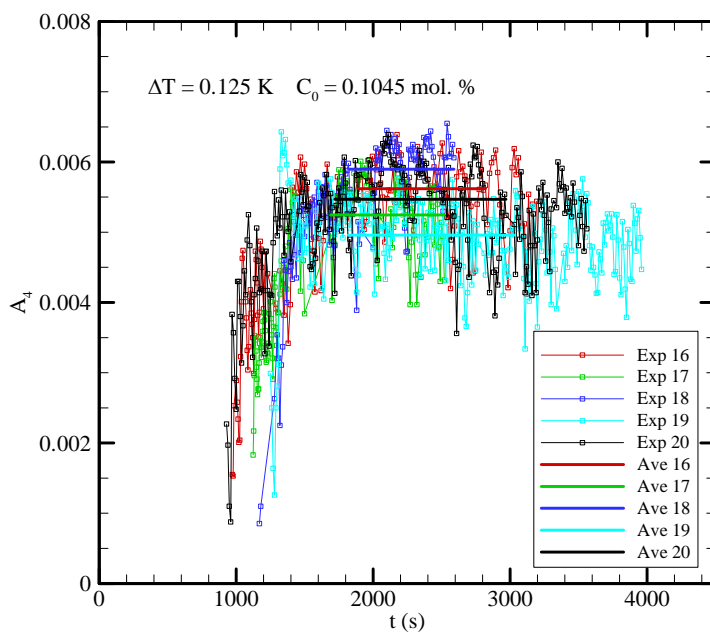
(b)

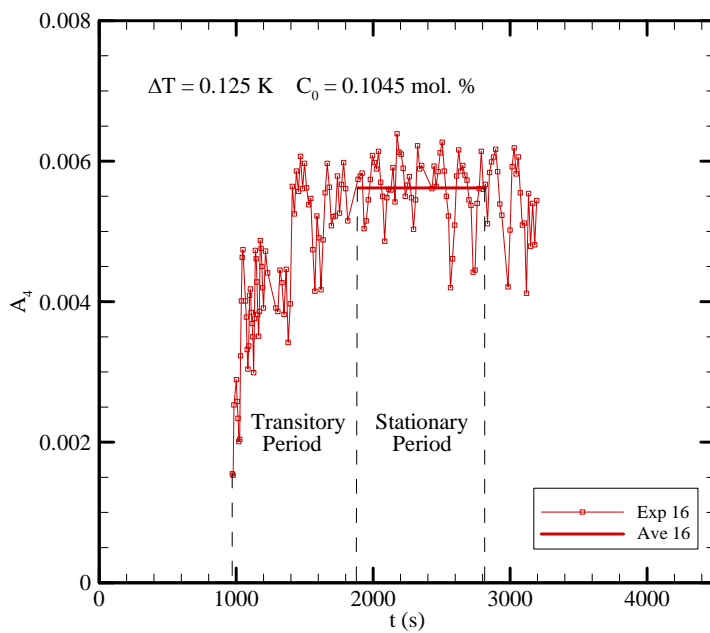Figure 3.5: Coefficient A_4 as a function of time.

(a) Single experiment for $\Delta T = 0.125\,\mathrm{K}$ and $C_0 = 0.1045$ mol. %

(b) Set of measurements for $\Delta T = 0.125\,\mathrm{K}$ and $C_0 = 0.1045$ mol. %.
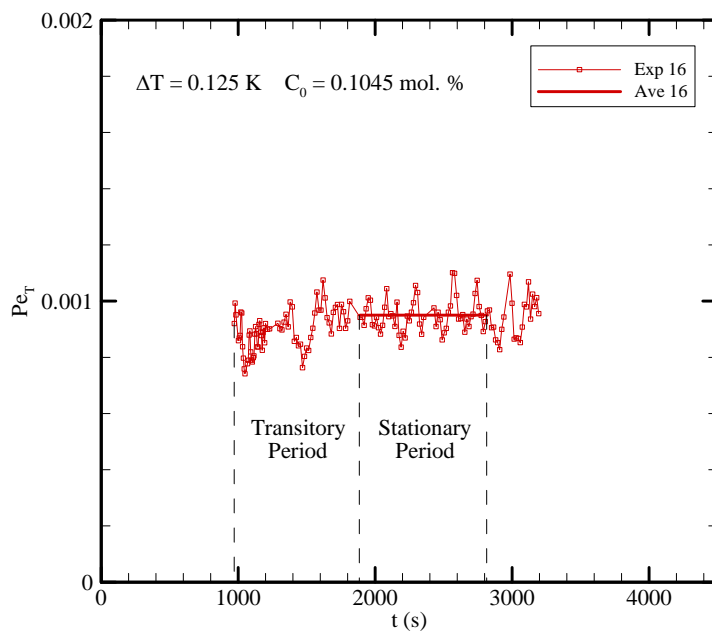
(a)
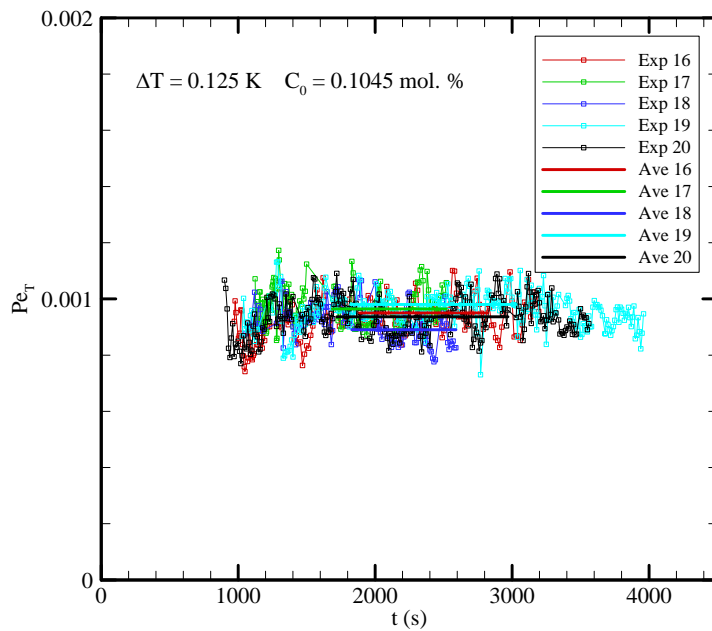
(b)

Figure 3.6: Peclet number as a function of time.
(a) Single experiment for $\Delta T = 0.125$ K and $C_0 = 0.1045$ mol. %
(b) Set of measurements for $\Delta T = 0.125$ K and $C_0 = 0.1045$ mol. %.
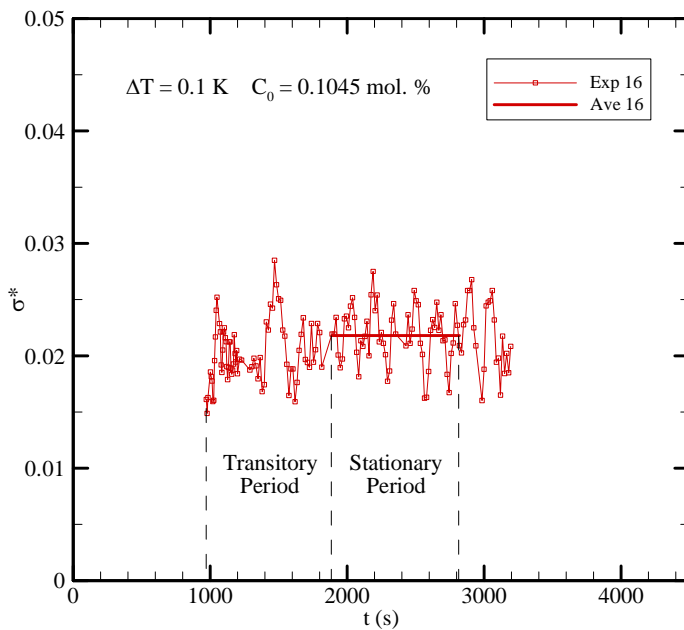
(a)
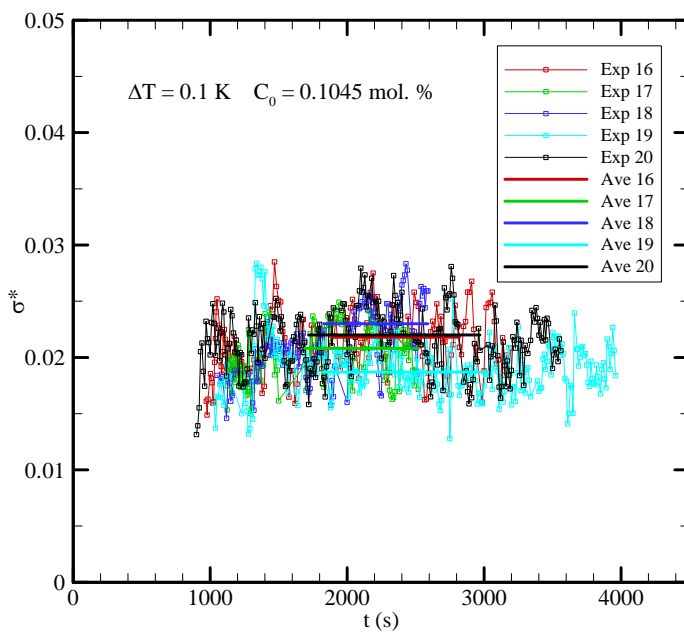
(b)

Figure 3.7: Selection parameter as a function of time.

(a) Single experiment for $\Delta T = 0.125\,\mathrm{K}$ and $C_0 = 0.1045$ mol. %

(b) Set of measurements for $\Delta T = 0.125\,\mathrm{K}$ and $C_0 = 0.1045$ mol. %.

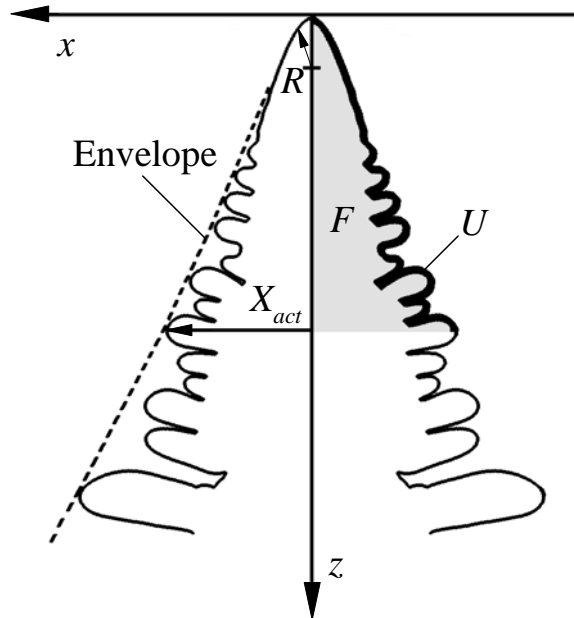Figure 3.8: Parameters used to characterize the sidebranching's morphology. The dendrite's envelope is illustrated on the left half of the figure. Conversely, the integral parameters (F and U) are sketch on the right half.

CHAPTER IV

RESULTS AND DISCUSSION

4.1 Introduction

All contributions of the current investigation are summarized in this chapter. First, the data collected for pure SCN are presented and discussed. Then, the experiments with alloys are reviewed. In both cases, the new experimental data will be compared with theoretical models and previous experimental benchmarks. Two major points are stressed in this discussion. On one hand, the significant agreement found between the experiments with pure SCN and a previous benchmark by Glicksman et al. [69] validates the experimental methodology presented in Chapter III. On the other hand, the current experimental data for alloys exhibits more consistency than previous benchmarks and allows further validation of several aspects of the existing theories for free dendritic growth. Note that all physical properties used in this investigation are summarized in Table 4.1.

Most theories of dendritic growth have two components, a transport model and a selection criterion. Through the transport model, the Peclet number is estimated using the applied undercooling as input. Once the Peclet number is known, the selection criterion is employed to determine uniquely the tip velocity and radius. Consequently, the predictions of tip velocity and radius depend on both transport model and selection criterion. For that reason, the following discussions will address firstly the performance of transport models and selection criteria. Thereafter, predictions of tip velocity and radius will be evaluated. Finally, the dendrite's shapes obtained in this investigation are compared to the MST and phase field simulation predictions. Since the growth velocity and tip radius are the measured variables, this approach might seem contra-intuitive. However it allows identifying causes of disagreement between experiments and theoretical predictions.

<u>4.2 Experiments with Pure Succinonitrile</u>

Fourteen successful experiments, over a range of undercoolings between 0.1 and 1.0 K, are presented here for pure SCN. Several micrographs corresponding to these experiments are shown in Figure 4.1. For each performed test, the stationary values of growth velocity, tip radius, Peclet number, selection parameter ($\sigma *$), the coefficient A_4, and growth angle with respect to gravity are reported (Table 4.1) All collected data correspond to dendrites growing downward. The current benchmark shows good agreement with the existing theories, experiments and simulations of free dendritic growth. Such consensus validates experimental methodology used.

<u>4.2.1 Results for the Selection Parameter</u>

The LGK and LB models use the same selection criterion. They consider that selection parameter ($\sigma* = 2\alpha d_0 / V R^2$) is a constant, independent of the Peclet number and the applied undercooling. For pure SCN, the most accepted value of the selection parameter is 0.02 [50-51, 69]. In order to evaluate the selection criterion adopted in LGK and LB models, the selection parameter calculated from the measurements is compared to the constant value of 0.02 in Figure 4.2a. This graph portrays the selection parameter as a function of the applied undercooling. It shows that the selection parameter does not remain constant over the entire range of studied undercoolings. Moreover, the selection parameter seems to decay with the undercooling. A similar behavior was reported by Glicksman et al. [69].

Figure 4.2b portrays a comparison between the collected data and the terrestrial benchmark by Glicksman and coworkers [69] in terms of the selection parameter. Besides the dispersion in the data by Glicksman et al. [69], a reasonable qualitative agreement can be observed. Our measurements lay within the dispersion of Glicksman's values, even thought the first are slightly smaller. With the intention of quantitatively

comparing these experimental benchmarks, the collected data for the selection parameter in the present investigation have been regressed to the following power-law relationship:

$$\sigma^* = \sigma_0 \Delta T^n \qquad\qquad (4.1)$$

where σ_0 and n are adjustable parameters. If the selection parameter were independent of the undercooling, n would be zero and σ_0 would be equal to the average of the collected data for the selection parameter. Glicksman and coworkers reported a similar regression for each set of experiments presented in reference [69]. The regression obtained in the present research $\left(\sigma_0 = 0.0166 \text{ and } n = -0.151\right)$ reaffirms that the selection parameter is inversely related to the applied undercooling. Furthermore, these fitting parameters are close to the values reported $\left(\sigma_0 = 0.0194 \pm 0.0004 \text{ and } n = -0.088 \pm 0.017\right)$ by Glicksman et al. [69] for terrestrial experiments. Interestingly, our exponent agrees better with Glicksman's results for microgravity $\left(n = -0.131 \pm 0.014\right)$ and for the diffusion limited range $\left(n = -0.203 \pm 0.045\right)$. This later finding indicates that the disagreement between our data and the terrestrial benchmark by Glicksman has a systematic origin. Since the microgravity data was collected after the terrestrial benchmark, it is reasonable to infer that methodology and equipments used in space are closer to those employed during this investigation and presented in Chapter III.

Through three-dimensional phase field simulations, Karma and Rappel [60] showed that the selection parameter decreases linearly with the undercooling (or Peclet number). In addition, Ramirez and Beckermann [103] also predicted an almost linear decrease in the selection parameter, as defined in the LGK and LKT models, with the applied undercooling (or Peclet number) using two-dimensional phase field simulations. Neither of these numerical investigations studied the exact range of surface energy anisotropy and applied undercooling corresponding to most experimental benchmarks, because of limitations in the computational cost of the simulations. However, their

qualitative agreement with the experimental benchmark by Glicksman et al. [69] and the present investigation seriously challenge the constancy of the selection parameter.

Two main conclusions can be drawn from the previous findings. On one hand, the selection criteria implemented into the LGK and LB models are not realistic for the range of studied condition. On the other hand, the collected data agrees reasonably well with the benchmark by Glicksman and coworkers [69] in terms of the selection parameter.

4.2.2 Results for the Peclet Number

In order to evaluate the transport portions of the LGK* and LB models, the thermal Peclet numbers obtained from experimental measurements and theoretical predictions are compared in Figure 4.3a. This logarithmic graph portrays the Peclet number as a function of the undercooling. Two predictions for the LB model are presented: the first one (continuous line) results from assuming $\sigma^* = 0.02$, while the other (white triangles) utilizes the measured selection parameter. It can be observed that the thermal Peclet number increases monotonically with the undercooling. An outstanding agreement between both LB model predictions and the collected data is observed for the range of undercooling studied $(0.1\,\mathrm{K} \leq \Delta T \leq 1.0\,\mathrm{K})$. Such behavior was expected because the convective effects control dendritic growth at low undercoolings. The agreement between both prediction for the LB model and our measurement indicates that the selection parameter (σ^*) and the thermal Peclet number (Pe_T) are independent of each other as the theory predicts. Also, the disagreement observed between LGK model prediction and the collected data indicates that the convective effects are important for the range of studied undercoolings. Moreover, the discrepancy between our measurements and the LGK model is similar to that reported in reference [69] (Figure 4.3b).

---

* In the absence of solutal and capillary undercoolings, the LGK model is reduced to the Ivantsov solution.

Our measurements are compared to the experimental benchmark by Glicksman et al. [69] in Figure 4.3b. Both sets of data show the same trend, the dispersion in Glicksman's data is enclosed by our uncertainty bars for almost the entire range of studied undercoolings. For undercoolings above 0.2 K, our measurements are slightly bigger than the averages for Glicksman's data. In general, both benchmarks agree quite well. This agreement validates our methodology.

4.2.3 Growth Velocity Measurements

Growth velocity measurements are presented as a function of the undercooling in Figure 4.4a. The predictions of the LGK and LB models based on a constant selection parameter $\left(\sigma^* = 0.02\right)$ are also presented in the same figure. In this logarithmic plot, it can be appreciated that the tip velocity increases with the undercooling. An outstanding agreement with the LB model can be observed for undercoolings below 0.6 K. Indeed, the small differences between experiments and theoretical predictions in this range of undercoolings are within the uncertainty of the measurements. The agreement between experiments and the LB model was expected, since convective effects dominate dendritic growth at low undercoolings. Glicksman et al. [69] reported a similar trend even in microgravity conditions.

For undercoolings above 0.6 K, the experimental data get closer to prediction of the LGK model. This behavior was expected, since diffusive effects dominate the growth of dendritic crystal at high undercoolings. However, the divergence of the experimental data from the LB model occurs before the corresponding theoretical estimate $\left(\Delta T = 1.7\,\text{K}\right)$. This finding indicates that LB model overpredicts slightly the convective effects for undercoolings above 0.6 K. The present benchmark is compared to the terrestrial measurements of Glicksman et al. [69] in Figure 4.4b. Both sets of experiments show the same behavior. Furthermore, the small dispersion in the terrestrial data by Glicksman and coworkers is within the uncertainty of the current benchmark. Finally, it

can be concluded that our velocity measurements have a good overall agreement with both the prediction of the LB model and the terrestrial data by Glicksman and coworkers [69].

4.2.4 Tip Radius Measurements

According to the MST [16-17], the dendrite shape is parabolic in the immediate vicinity of the tip, but it starts to evolve into a non-axisymmetric shape called non-axisymmetric needle crystal within a short distance from tip. It is well known that the cross section of this non-axisymmetric needle crystal can be described by a fourth order polynomial. In order to verify these aspects of the MST and to assess the quality of our measurements, the tip radius is presented in Figure 4.5a as function of the fitting range for a parabola and a four order polynomial. Furthermore, this figure compares the results for two different undercooling (0.2-0.7 K).

For the low undercooling (0.2 K), it can be seen that the tip radius increases linearly with the fitting range when the parabolic fit is used. Such behavior is consequence of the continuous deviation from the parabolic shape far from the tip. Conversely, the tip radius remains constant when the fourth order polynomial fit is used. In case of the high undercooling (0.7), the accumulation of error barely can be appreciated when the parabolic fit is used. This means that the resolution of the photos is not enough to register any difference between one regression and the other.

Because of the lack of resolution, it is natural to extend the fitting range as much as possible so a stable measurement can be taken. However, the inclusion of sidebranches inside the fitting range needs to be avoided if possible. In order to get a good compromise between these issues, a fitting range of 10 radii behind the tip was adopted. The uncertainty of the radius was established as the difference between the values for fitting ranges of 6 radii and 10 radii behind the tip. Since the sidebranches generally appear 6 radiuses or more behind the tip, the value for such fitting range was selected as a

reference for the uncertainty estimation. Additionally, the robust fitting method was adopted to reduce the effects of the inclusion of the sidebranches inside the fitting range. The robust fitting is relatively insensible to outliers and help to obtain stable measurements of the tip radius. Figure 4.5b portrays the coefficient of the 4th order non-axisymmetric term A_4 as a function of the fitting range for two different undercoolings (0.2–0.7 K). It can be seen that our photos do not have enough resolution to facilitate the measurement the coefficient A_4 for undercoolings above 0.7 K. The measurements undercoolings below 0.7 K are discussed in the next section.

Figure 4.6 presents a comparison among the actual dendrite shape for an undercooling of 0.3 K, the corresponding parabola (red dots) and the non-axisymmetrical needle crystal (green dots). Instead of using the value of A_4 predicted by the MST $\left(A_4 = 1/96\right)$, the measure value $\left(A_4 = 0.004\right)$ was employed to draw the needle crystal contour. An outstanding agreement can be appreciated between the dendrite contour and the shapes proposed by the MST. The first sidebranches appear around 8 radii behind the tip. Also it can be appreciated that the needle crystal approximation breaks down around 15 radii behind the tip.

Finally, the tip radius measurements as a function of the applied undercooling are portrayed in the logarithmic plots contained in Figure 4.7 Again, a comparison between experimental data and the predictions of LGK (dash line) and LB (continuous) models are provided for $\sigma* = 0.02$ (Figure 4.7a). Another prediction of the LB (white triangles) model is presented, in this case the tip radius is estimated using the measured $\sigma*$. As expected, the tip radius is inversely related to the applied undercooling. This trend can also be appreciated through the set of micrographs presented in Figure 4.1. The agreement between collected data and the prediction of the LB model with constant $\sigma*$ is satisfactory for undercoolings less than or equal to 0.4 K. In the case of undercoolings bigger than 0.4 K, the radius measurements deviate towards the LGK prediction. This change in tip radius behavior was anticipated since the dendritic growth at low

undercoolings is controlled by convective effects. The decline in the selection parameter with the undercooling might be responsible for the departure of the radius measurement from the prediction of the LB model with constant σ^*. Because the selection parameter is inversely proportional to the square of the tip radius, the deviation of the radius measurement from the LB model prediction with constant σ^* is larger than in the case of the growth velocity. Conversely the prediction of the LB model using the measured σ^* agrees with our experimental measurements along the entire range of studied undercooling . In Figure 4.7b, our measurements are compared to those by Glicksman and coworkers [69]. A complete agreement can be observed.

4.2.5 Results for the Coefficient A_4

As stated in Chapter II, the amplitude of dendrite's ridges can be quantified through the coefficient A_4. According to the MST [16-17], this parameter is predicted to be universal and equal to 1/96. However, phase field simulations by Karma and coworkers [58] predicted a smaller value $\left(A_4 \approx 0.0045\right)$ for a fitting range of ten radii behind the tip. For this particular fitting range, the phase field simulations shows that the coefficient A_4 is almost independent of the surface energy anisotropy intensity and the applied undercooling. Glicksman and coworkers [69] studied experimentally the morphology of pure SCN dendrites. They used a fourth order polynomial to fit the dendrite contour and to measure A_4. Using a fitting range of eight radii behind the tip, these authors found that $A_4 = 0.004$. The measurements of the coefficient A_4 collected during the present investigation are displayed in Figure 4.6. These measurements come from a regression to a fourth order polynomial with a fitting range of ten radiuses behind the dendrite tip. In this plot, the coefficient A_4 is portrayed as function of the applied undercooling. It can be appreciated that the coefficient A_4 is roughly constant and equal to 0.004. The fluctuations in the value of A_4 are well within the uncertainty of the experiments. Even though the collected measurements present a factor two difference

with the MST prediction, a qualitative agreement with the MST can be claimed. On the contrary, an outstanding quantitative agreement with the phase field simulations of Karma et al. [58] and the experimental benchmark by Glicksman et al. [69] can be appreciated.

4.2.6 Sidebranching Morphology

4.2.6.1 Dendrite Envelope

Li and Beckermann [85-86] measured the dendrite envelop for the pure SCN dendrites grown in microgravity by Glicksman and coworkers [69]. They found the following expression for the envelope:

$$\frac{X_{act}}{R} = 0.67 \left(\frac{z}{R} \right)^{0.86} \tag{4.2}$$

The discrepancies between the measurement by Li and Beckermann and the MST prediction are due to two-dimensional nature of the MST model for the sidebranches. Since such model is based in the solution for the Hele-Shaw flow proposed by Algrem [1], it does not account for the three-dimensional features of the boundary layer around the dendrite. The measurements of integral parameters show similar disagreements with the MST.

In order to validate our methodology, the dendritic envelope was measured for pure SCN dendrites grown under seven different undercoolings (0.1, 0.2, 0.3, 0.5, 0.6., 0.8, 1.0 K). The results are presented in Figure 4.9; the envelope obtained is given by:

$$\frac{X_{act}}{R} = 0.60 \left(\frac{z}{R} \right)^{0.92} \tag{4.3}$$

Along with our experimental data, Figure 4.9 portrays the tip's shape predicted by the MST (non-axisymmetric needle crystal) and Li's envelop. An outstanding agreement

between terrestrial and microgravity envelop can be seen. Both envelopes meet the non-axisymmetric needle crystal around 10 radii from the tip. The terrestrial envelop is thinner than the microgravity one. Since the experiments on earth correspond to dendrites grown downward, the effects of heat convection may be responsible for the morphological differences in the sidebranches.

4.2.6.2 Projection area

The experimental investigations by Hurlimann et al. [52] and Bisang and Bilgram[14-15] hinted that the dendritic structure can be described by geometrical parameters, which are independent of the undercooling, and that can be scaled by the tip radius. The projection area corresponds to one half of the cross sectional area enclosed by the dendrite's ridges. Integrating Equation 2.40, the prediction of the MST for the normalized projection area can be obtained:

$$\frac{F}{R^2} = 0.85 \left(\frac{z}{R} \right)^{1.60} \tag{4.4}$$

Li and Beckermann [85-86] also measured the normalized projection area for the dendrites grown in microgravity during the IDGE flights [69] and reported the following expression:

$$\frac{F}{R^2} = 0.58 \left(\frac{z}{R} \right)^{1.72} \tag{4.5}$$

In Figure 4.10, our measurements of the normalized projection area for pure SCN dendrites are presented along with Li's results and the normalized projection area for a non-axisymmetric needle crystal. Our expression for the normalized projection area is given by:

$$\frac{F}{R^2} = 0.56 \left(\frac{z}{R} \right)^{1.73} \tag{4.6}$$

The projection area of the terrestrial dendrites is slightly bigger than the projection area of microgravity dendrites. Such small difference is within the uncertainty of the measurements

4.2.6.3 Contour Length

The contour length corresponds to the distance for the tip to any point in the dendrite contour measured along the solid-liquid interface. Li and Beckermann [85-86] also measured the contour length for the dendrites grown in microgravity during the IDGE flights [69] and reported the following expression:

$$\frac{U}{R} = 0.38\left(\frac{z}{R}\right)^{1.50} \tag{4.7}$$

Our measurements of the contour length for pure SCN dendrites are presented in Figure 4.11 along with Li's results and the normalized projection area for a non-axisymmetric needle crystal. The latter was obtained applying the definition of arc length in two-dimensions to the fourth order polynomial proposed by the MST, and solving numerically the resulting integral. Our expression for the contour length is given by:

$$\frac{U}{R} = 0.36\left(\frac{z}{R}\right)^{1.50} \tag{4.8}$$

The morphological differences between terrestrial and microgravity dendrites are very slim, observed differences are within the uncertainty of the measurements. This outstanding agreement among our measurements and several previous investigations validates the methodology proposed to characterize the sidebranching

4.3 Experiments with Succinonitrile-Acetone Alloys

Four dilute SCN-ACE alloys (0.1045, 0.1710, 0.3065 and 0.4976 mol. %) had been studied. Ninety three successful experiments were carried out on these alloys over a

range of undercoolings between 0.1 and 0.7 K. Micrographs shown in Figures 4.11 to 4.14 correspond to these experiments. As in the case of pure substances, only dendrites growing downward were considered in this investigation. For each experiment, the steady-state values of growth velocity, tip radius, Peclet number, selection parameter, growth angle with respect to gravity, and the sidebranching parameters were measured or estimated following the proposed methodology (Chapter III). In addition, each experiment was replicated between two and five times to ensure the statistical significance of the reported data. All collected data are presented in Tables 4.2, 4.3, 4.4 and 4.5. This experimental benchmark is aimed at to corroborate and to complement the experimental investigation carried out by Chopra and coworkers [23].

4.3.1 Selection Parameter

<u>4.3.1.1 Effects of Undercooling</u>

The selection parameter is presented in Figure 4.16 as a function of the applied undercooling for each of the SCN-ACE alloys studied. As in the case of pure SCN, the selection parameter decreases almost linearly with the undercooling. The slope for alloys is slightly steeper than for pure SCN. The selection parameter dependence on the undercooling is almost identical for all studied alloys. Statistical tests of correlation show that the selection parameter depends only on the undercooling (p-value = 0.000 and Pearson coef = -0.595). On one hand, a negative Pearson coefficient means that the selection parameter and the undercooling are inversely related as stated above. On the other hand, a p-value of 0.000 indicates that there is almost 100% confidence on the correlation between the selection parameter and the undercooling. These findings can be supported qualitatively by the phase-field simulations of Ramirez and Beckermann [103], which predicted similar behavior for the selection parameter of alloys defined by the LGK and LKT models. In addition, our data show more consistency and less scatter in terms of the selection parameter than the benchmark by Chopra et al.

4.3.1.2 Effects of Solute Concentration

Figure 4.16 shows that any variation in the selection parameter respect to the solute concentration is within the uncertainty of our experiments. Statistical analysis shows no correlation between this variables (p-value = 0.870 and Pearson coef = 0.017). Specifically a p-value above 0.05 means a very low level of confidence in the relation between the selection parameter and solute concentration, and a Pearson correlation coefficient of 0.017 a weak dependence between this variables. For all concentrations, the selection parameter $\sigma*$ is less or equal to 0.02. This finding indicates that the inconsistencies in Chopra's measurements of the selection parameter [23] for concentrations above 0.1 mol % were caused by systematic errors. According to Trivedi and Kurz [118], the selection parameter $\sigma*$ should be independent of the solute concentration and undercooling (or Pe_T). Recently, Liu et al. validated the MST and LGK model for an Al- 4 wt% Cu alloy under solidification directional in the fully diffusive regime. Consequently, it is reasonable to assume that convective effects are responsible for the discrepancy between our data and the theories for alloys.

4.3.2 Results for the Peclet Number

4.3.2.1 Effects of Undercooling

The Peclet number as a function of the undercooling is presented in the logarithmic plots contained in Figures 4.17 and 4.18. Two predictions for the LB model are reported: the first one (continuous line) results from assuming a constant selection parameter $(\sigma* = 0.02)$, while the other (white triangles) utilizes the measured selection parameter. In the LGK prediction (dashed line), the selection parameter is also assumed to be constant $(\sigma* = 0.02)$. For all concentrations studied the thermal Peclet number increases almost monotonically with the undercooling. Figure 4.17 shows that both LB model predictions agree outstandingly with the collected data along the entire range of undercooling studied $(0.1\,\text{K} \leq \Delta T \leq 0.7\,\text{K})$, for low solute concentrations (0.1045 and

0.1710 mol. %). Conversely, an important disagreement between the experimental results and the LGK model can be appreciated for such concentrations. These findings suggest that the dendritic growth of alloys with low solute concentrations is controlled by convective effects. Moreover, the agreement between the current experiments and the LB model predictions indicates that such model accounts effectively for thermo-solutal convection.

For higher solute concentrations (0.3065 and 0.4976 mol %), the transition towards the diffusive regime starts (Figure 4.18). The agreement between the measurements and the LGK predictions improves over the entire range of studied undercooling, but more strongly at high undercoolings. It is important to mention that the measurements of Peclet never fall below the prediction of the diffusion theory (LGK). This means that thermal and solutal boundary layers, indeed, cooperate with each other. Consequently, such important assumption of the LB model holds for the set of measurements presented here. Besides, this finding supports our claim that this measurements only correspond to dendrites growing downward.

4.3.2.2 Effects of Solute Concentration

In Figures 4.19 to 4.21, experimental and theoretical values of the thermal Peclet number are presented as functions of the solute concentration for all studied conditions. It is worthwhile to mention that the undercooling was not kept constant during the study of solutal effects. Because of that, some results can only be compared qualitatively with previous investigation. As usual, two predictions for the LB model are reported: the first one (continuous line) corresponds to a constant selection parameter $(\sigma^* = 0.02)$, whereas the other (white triangles) utilizes the measured selection parameter. The LGK prediction (dashed line) results also from assuming a constant selection parameter $(\sigma^* = 0.02)$. As most dendritic growth theories predict, the collected data indicate that the thermal Peclet number decreases monotonically with the solute concentration. In general the theoretical

predictions are within the uncertainty of the experiments. Also, the thermal Peclet number is independent of the selection parameter as the theories predict. With the exceptions of points for concentrations of 0.1045 and 0.1710 mol %, both LB predictions lay in top of each other. This agreement evidences the independence of the Peclet number from the selection parameter. Furthermore, the apparent deviations between the LB predictions for concentrations of 0.1045 and 0.1710 mol % are caused by differences in the undercoolings. In other words, LB predictions assuming constant selection parameter $(\sigma^* = 0.02)$ correspond to undercoolings smaller than those for LB predictions using the measured selection parameter.

These results indicate that the transport portion of the LB model can accurately estimate the heat and solute transfer during free dendritic solidification of alloys for all solute concentrations studied. Above 0.1710 mol %, diffusive effects start to take control of the solidification process and the experimental data deviates slightly from the LB prediction. The observed discrepancies between model predictions and experiments are in general within the reported uncertainties. However, further calibration of the LB models using the current experimental benchmark might be needed.

4.3.3 Velocity Measurements

4.3.3.1 Effects of Undercooling

The tip velocity is presented as a function of the applied undercooling for each of the studied concentration in Figures 4.22 and 4.23. These plots have been formatted using the conventions presented before. These logarithmic charts show that the growth velocity increases monotonically with the undercooling. In previous analysis of the results, it was found that the LB model predicts more accurately the Peclet number for concentrations less or equal to 0.1710 mol%. Keeping that finding in mind, the results corresponding to concentrations below and above 0.1710 mol % are discussed separately.

For low solute concentrations $(C_0 \leq 0.1710)$, the velocity measurements exhibit good agreement with the LB prediction using a constant selection parameter for undercooling below 0.4 K. This finding indicates that the selection criterion of the LB model under predicts the stability constant $(\sigma *)$ for undercooling above 0.4 K. A careful inspection to the LB predictions based on the measured selection parameter (Figure 4.22), taking into account that the velocity and the selection parameter are directly related, corroborates this hypothesis. The predicted velocities based on the measured stability constant are significantly smaller than our measurements for undercooling above 0.4 K. The adoption of a selection criterion similar to the one in the LKT model might help to prevent the under prediction of the stability constant. However, some additional modifications to this selection criterion might be needed because Ramirez et al.[103] reported that LKT correction to the stability constant were meaningless for Peclet numbers less or equal to 0.3.

In the case of high solute concentrations $(C_0 \geq 0.1710)$, both Peclet number and selection parameter are over predicted by the LB model. This behavior recedes when pure diffusion conditions (higher undercooling) are achieved. The agreement between our measurements and the LB prediction based on the measured stability constant, for an undercooling of 0.7 K and concentrations of 0.3065 and 0.4976 mol %, illustrates this finding. For undercoolings below 0.7 K, the LB model over predicts the growth velocities.

4.3.3.2 Effects of Solute Concentration

Figures 4.24, 4.25 and 4.26 portray the tip velocity as a function of the solute concentration. Because of the variation in the undercoolings, it is difficult to observe the dependence of the tip velocity on the solute concentration. However, the main theoretical predictions can be corroborated at least qualitatively. It is evident from these figures that the growth velocity increases with the solute concentration, reaches a maximum for

solute concentrations between 0.1 and 0.2 mol %, and then decreases with further increments in the concentration. Such behavior is consequence of the competition between the rejection of solute and the latent heat release. While the diffusion of solute ahead of the interface retards the growth and destabilizes the tip, the dissipation of the latent heat speeds up the dendrite causing the observed maximum in the velocity. An analysis of the performance of the LB model can be conducted using Figures 4.24, 4.25 and 4.26, however it will yield identical conclusions to those presented in the previous section

4.3.4 Radius Measurements

The dependence of the tip radius on the fitting range was studied in order to determine the suitability for alloys of the criterion adopted for measurement on pure SCN dendrites. Figure 4.27 portrays the tip radius and the coefficient A_4 as function of the fitting range using a parabolic fit and a four order polynomial regression. This figure contains the results for pure SCN and SCN-Acetone alloy for undercoolings around 0.2 K. In order to made this comparison as meaningful as possible, the alloy studied correspond to the solute concentration (0.1710 mol %) that produces the smallest dendrites observed

For pure SCN, it can be seen that the tip radius increases linearly with the fitting range when the parabolic fit is used. Conversely, the tip radius remains constant when the fourth order polynomial fit is used. For the alloy, the accumulation of error is less significant when the parabolic fit is used. Also the measurement using the fourth order regression is less stable than in the case of pure SCN. Moreover, the difference between in the radiuses for fitting ranges of 6 and 10 radii behind the tip is around 10%. This level of uncertainty in the radius is relatively high, because it translates into an uncertainty of 20 % in the stability constant. However, such criterion was adopted also for alloys because of the excellent validation obtained for pure SCN. Figure 4.27b portrays the

coefficient of the 4th order non-axisymmetric term A_4 as a function of the fitting range for pure SCN and SCN-Acetone dendrites. The data presented correspond to undercoolings around 0.2 K. It can be seen that our photos do not have enough resolution to allow the measurement of the coefficient A_4 in alloys.

Figures 4.28, 4.29 present comparisons among the actual dendrite shapes, the corresponding parabolas (red dots) and the non-axisymmetrical needle crystals (green dots) for all studied alloys. All comparisons were obtained for undercooling around 0.3 K. The most accepted value for the coefficient of the 4th order non-axisymmetric term $(A_4 = 0.004)$ was employed to draw the needle crystal contours. An outstanding agreement can be appreciated between the dendrite contours and the shapes proposed by the MST. This finding indicates that the MST might also be true for alloys. For the low solute concentrations (0.1045 and 0.1710 mol %), the first sidebranches seem to appear between 4 and 6 radii behind the tip. In the case of high solute concentrations (0.3064 and 0.4976 mol %), the first sidebranches seem to appear between 6 and 8 radiuses behind the tip. These values are reported here just to provide a qualitative description. They can be misleading because the studied dendrites grew in different directions and the appearance of the sidebranches varies significantly depending on their orientation. .For all studied dendrites, the needle crystal approximation breaks down around 15 radii behind the tip because the same value of the coefficient of the 4th order non-axisymmetric term $(A_4 = 0.004)$ was used to plot all non-axisymmetric needle crystals.

4.3.4.1 Effects of Undercooling

The tip radius measurements as a function of the applied undercooling are portrayed in the logarithmic plots contained in Figure 4.30 and 4.31. As expected, the tip radius is inversely related to the applied undercooling. This trend can also be appreciated through the set of micrographs presented in Figures 4.13, 4.14 and 4.15. For low solute concentrations ($C_0 \geq 0.1710$ mol %), the radius measurements exhibit some agreement

with the LB prediction using the measured stability constant (Figure 4.30). These predictions are consistently bigger than our measurements, although most of them are enclosed by the uncertainty of the measurements.

In the case of high solute concentrations ($C_0 \geq 0.1710$ mol %), the tip radius is under predicted by the LB model until pure diffusive regime ($\Delta T \geq 0.7$ K) is achieved. The agreement between our radius's measurements and the LB prediction based on the measured stability constant, for an undercooling of 0.7 K and concentrations of 0.3065 and 0.4976 mol %, illustrates this finding.

4.3.3.2 Effects of Solute Concentration

Figures 4.32, 4.33 and 4.34 portray the tip radius as a function of the solute concentration. It can be seen that, the tip radius decrease monotonically with the solute concentration. A minimum in the tip radius can be appreciated for concentrations between 0.1 and 0.2 mol %. Our measurements do not have enough resolution to locate such minimum.

4.3.4 Sidebranching Morphology

4.3.4.1 Dendrite Envelope

Currently, the dendrite envelope and the integral parameter for dendritic sidebranching only have been reported for Xenon [13-15] and SCN [85-86]. Consequently, it is worthwhile to carry out those measurements for SCN-Acetone alloys. During the present investigation, four SCN-Acetone alloys were characterized. For each concentration dendrites grown under 6 different undercoolings were measured. The results in terms of the dendrite envelop are presented in Figure 4.35. The dendritic envelope for pure SCN dendrites and the non-axisymmetric needle crystal are presented in that figure. Li and Beckermann [85-86] obtained the following expression for the dendrite envelope:

$$\frac{X_{act}}{R} = 0.67\left(\frac{z}{R}\right)^{0.86} \tag{4.9}$$

Our envelope for SCN-Acetone alloys, presented in Figure 4.35, is given by:

$$\frac{X_{act}}{R} = 0.84\left(\frac{z}{R}\right)^{0.85} \tag{4.10}$$

An outstanding agreement between terrestrial envelop for alloys and microgravity envelop for SCN can be appreciated. These envelopes meet the non-axisymmentrical needle crystal at different locations. The terrestrial envelop meets the needle crystal around 6 radii behind the tip; while the microgravity one collide with the needle crystal around 10 radii behind the tip. The microgravity sidebranching is slightly thicker that the terrestrial one. The solute rejection is responsible for the morphological differences in the sidebranches. Since the solutal boundary layer has a smaller thickness than the thermal boundary layer, the thermal noise amplification along the dendrite is bigger for alloys than for pure substance.

4.3.4.2 Projection area

Measurements for the normalized projection area carried out for Li and Beckermann [85-86] for the dendrites grown in microgravity during the IDGE flights [69] can be summarized by the following expression:

$$\frac{F}{R^2} = 0.58\left(\frac{z}{R}\right)^{1.72} \tag{4.11}$$

In Figure 4.36, our measurements of the normalized projection area for SCN-Acetone alloys dendrites are presented along with Li's results and the normalized projection area for a non-axisymmetric needle crystal. Our expression for the normalized projection area is given by:

$$\frac{F}{R^2} = 0.58\left(\frac{z}{R}\right)^{1.77}$$
(4.12)

The projection area of the alloys dendrites is slightly bigger than the projection area of microgravity pure SCN dendrites. The observed differences are within the uncertainty of our measurements

4.3.4.3 Contour Length

Li and Beckermann [85-86] also measured the contour length for the dendrites grown in microgravity during the IDGE flights [69] and reported the following expression:

$$\frac{U}{R} = 0.38\left(\frac{z}{R}\right)^{1.50}$$
(4.13)

Our measurements of the contour length for SCN-Acetone alloys dendrites are presented in Figure 4.37 along with Li's results and the normalized projection area for a non-axisymmetric needle crystal. Our expression for the contour length is given by:

$$\frac{U}{R} = 0.25\left(\frac{z}{R}\right)^{1.55}$$
(4.14)

The contour length of alloys dendrites is slightly smaller than the contour length of microgravity dendrites. This difference is within the uncertainty of the measurements The agreement between the MST and our measurements of the side branching, in term of both the dendrite envelope and the integral parameter, indicates that the MST must be held true at some degree for alloys. Further research is needed to measured accurately the parameter A_4 and the exact relationship between the selection parameter $\sigma*$ and the anisotropy of the interfacial excess free-energy

4.3.5 Eulerian Angle

Appolaire et al.[126] investigated experimentally the settling of equiaxed dendritic crystal on an undercooled melts. They found a strong dependence of the selection parameter on the orientation of the crystal respect to the direction of settling (Eulerian angle). Such effect is not expected in our experiment because the flow induced by thermo-solutal natural convection is substantially slower than that created by the settling of the equiaxed crystal. Besides, Badillo et al.[127] recently showed experimentally that the selection parameter, based on the average velocity of the crystal settling down, is constant. However, some influence of the Eulerian angle on the Peclet numbers is expected, because the flow induced by the thermo-solutal natural convection goes always upward in the opposite direction to gravity. Consequently, the orientation of the dendrite will determine the shape of the boundary layers and the Peclet numbers.

The histogram for the Eulerian angle is presented in Figure 4.38. Only 7 experiments (6.36%) correspond to Eulerian angles bigger than 25 degrees. Also, about 80% of the data correspond to angles between 10 and 25 degrees. Consequently, a weak dependence between the selection parameter and the Eulerian angle should be expected.

Statistical test of correlation, in terms of the p-values and the Pearson coefficient, were carried out among the undercooling, the solute concentration, the thermal Peclet number, the selection parameter, and the Eulerian angle. These test show that there is some correlation between the Eulerian angle, the solute concentration and the Peclet number. In addition, the Eulerian angle and the Peclet number are inversely correlated. The dependence between this two variables is not too strong, the Pearson coefficient obtained (-0.393) indicates a less than linear relationship. As inferred from the histogram, there is no correlation between the Eulerian angle and the Eulerian angle.

Table 4.1: Experimental benchmark for free dendritic growth in pure succinonitrile ($C_0 = 0.0086\, \text{mol.}\%$).

ΔT (K)	V (μm/s)	ΔV (μm/s)	R (μm)	ΔR (μm)	Pe_T	ΔPe_T	σ^*	$\Delta\sigma^*$	A_4	ΔA_4	θ (deg)
0.100	3.2945	0.8208	93.9394	1.5875	0.00136	0.000341	0.02192	0.00587	0.00392	0.00017	13.36
0.200	10.6374	1.7263	51.4753	0.0806	0.00241	0.000392	0.02261	0.00377	0.00387	0.00021	15.70
0.300	23.1978	2.6235	36.5180	0.1671	0.00374	0.000423	0.02060	0.00237	0.00386	0.00020	9.93
0.400	39.8224	4.7183	27.6577	0.2227	0.00486	0.000577	0.02092	0.00254	0.00393	0.00028	7.15
0.500	60.0158	4.9894	23.6692	0.6574	0.00626	0.000549	0.01895	0.00191	0.00392	0.00054	6.23
0.600	84.0679	3.6002	19.7989	0.7119	0.00734	0.000410	0.01934	0.00162	0.00425	0.00040	6.76
0.700	114.6550	4.4511	18.3752	0.6712	0.00929	0.000495	0.01646	0.00137	-	-	25.37
0.800	148.0985	13.3487	16.2212	0.6097	0.01059	0.001034	0.01635	0.00193	-	-	19.95
0.900	179.2028	5.9471	14.7297	1.1656	0.01164	0.000999	0.01639	0.00268	-	-	6.11
1.000	234.6455	12.0863	13.0342	1.3618	0.01349	0.001571	0.01599	0.00351	-	-	15.25

Table 4.2: Experimental benchmark for free dendritic growth in succinonitrile acetone alloys ($C_0 = 0.1045$ mol.%).

ΔT (K)	V (μm/s)	ΔV (μm/s)	R (μm)	ΔR (μm)	Pe	ΔPe_T	σ^*	$\Delta\sigma^*$	θ (deg)
0.125	4.8896	0.1604	45.4662	0.9288	0.00098	0.000038	0.02024	0.00112	15.88
0.225	15.7563	0.2752	26.2866	1.2808	0.00183	0.000095	0.01763	0.00186	12.83
0.325	31.7281	0.8163	18.5179	2.0920	0.00259	0.000300	0.01683	0.00423	17.47
0.425	56.4301	1.3984	14.1710	2.1005	0.00353	0.000530	0.01537	0.00522	17.86
0.525	88.9393	3.0985	11.7355	1.7359	0.00460	0.000699	0.01352	0.00465	12.57
0.725	169.0321	8.8911	8.5894	2.0340	0.00640	0.001553	0.01236	0.00747	8.75

Table 4.3: Experimental benchmark for free dendritic growth in succinonitrile acetone alloys ($C_0 = 0.1710$ mol. %).

ΔT (K)	V (μm/s)	ΔV (μm/s)	R (μm)	ΔR (μm)	Pe	ΔPe_T	σ^*	$\Delta\sigma^*$	θ (deg)
0.141	7.2179	0.1641	31.7028	2.4653	0.001009	0.000082	0.01962	0.003278	18.42
0.241	18.1527	1.4347	20.2915	2.3201	0.001624	0.000226	0.01805	0.004801	19.98
0.341	38.1446	2.8168	14.2361	1.9189	0.002394	0.000368	0.01650	0.005196	19.36
0.441	60.3046	2.3649	12.0906	1.1864	0.003215	0.000340	0.01375	0.003081	17.35
0.541	88.5782	4.7361	10.6116	1.3061	0.004144	0.000556	0.01155	0.003337	15.45
0.741	160.4276	11.8061	8.0049	1.4185	0.005662	0.001086	0.01043	0.004558	11.12

Table 4.4: Experimental benchmark for free dendritic growth in succinonitrile acetone alloys ($C_0 = 0.3065 \, \text{mol.}\%$).

ΔT (K)	V (μm/s)	ΔV (μm/s)	R (μm)	ΔR (μm)	Pe	ΔPe_T	σ^*	$\Delta\sigma^*$	θ (deg)
0.200	6.1726	0.3271	26.6432	1.3303	0.00073	0.000053	0.02077	0.00249	14.62
0.300	16.1517	0.2128	17.5123	2.1917	0.00125	0.000157	0.01736	0.00477	16.44
0.400	30.1691	0.6707	12.8694	1.5450	0.00171	0.000209	0.01649	0.00440	15.81
0.500	46.7873	3.0531	10.5221	1.9165	0.00217	0.000420	0.01532	0.00661	18.53
0.700	94.6685	4.5391	8.0950	1.0552	0.00338	0.000469	0.01177	0.00359	19.07
0.800	119.2196	3.6698	6.3416	1.0855	0.00333	0.000580	0.01528	0.00619	20.23

Table 4.5: Experimental benchmark for free dendritic growth in succinonitrile acetone alloys ($C_0 = 0.4976$ mol.%).

ΔT (K)	V (μm/s)	ΔV (μm/s)	R (μm)	ΔR (μm)	Pe	ΔPe_T	σ^*	$\Delta\sigma^*$	θ (deg)
0.300	11.2005	0.3152	17.1887	0.9410	0.00085	0.000052	0.01764	0.00212	32.70
0.400	21.3487	2.2474	11.9534	0.7129	0.00113	0.000136	0.01854	0.00324	36.15
0.500	31.7273	0.7250	10.1008	1.5394	0.00141	0.000218	0.01696	0.00583	23.55
0.700	62.5460	2.5334	8.0556	1.5352	0.00222	0.000433	0.01260	0.00569	35.54
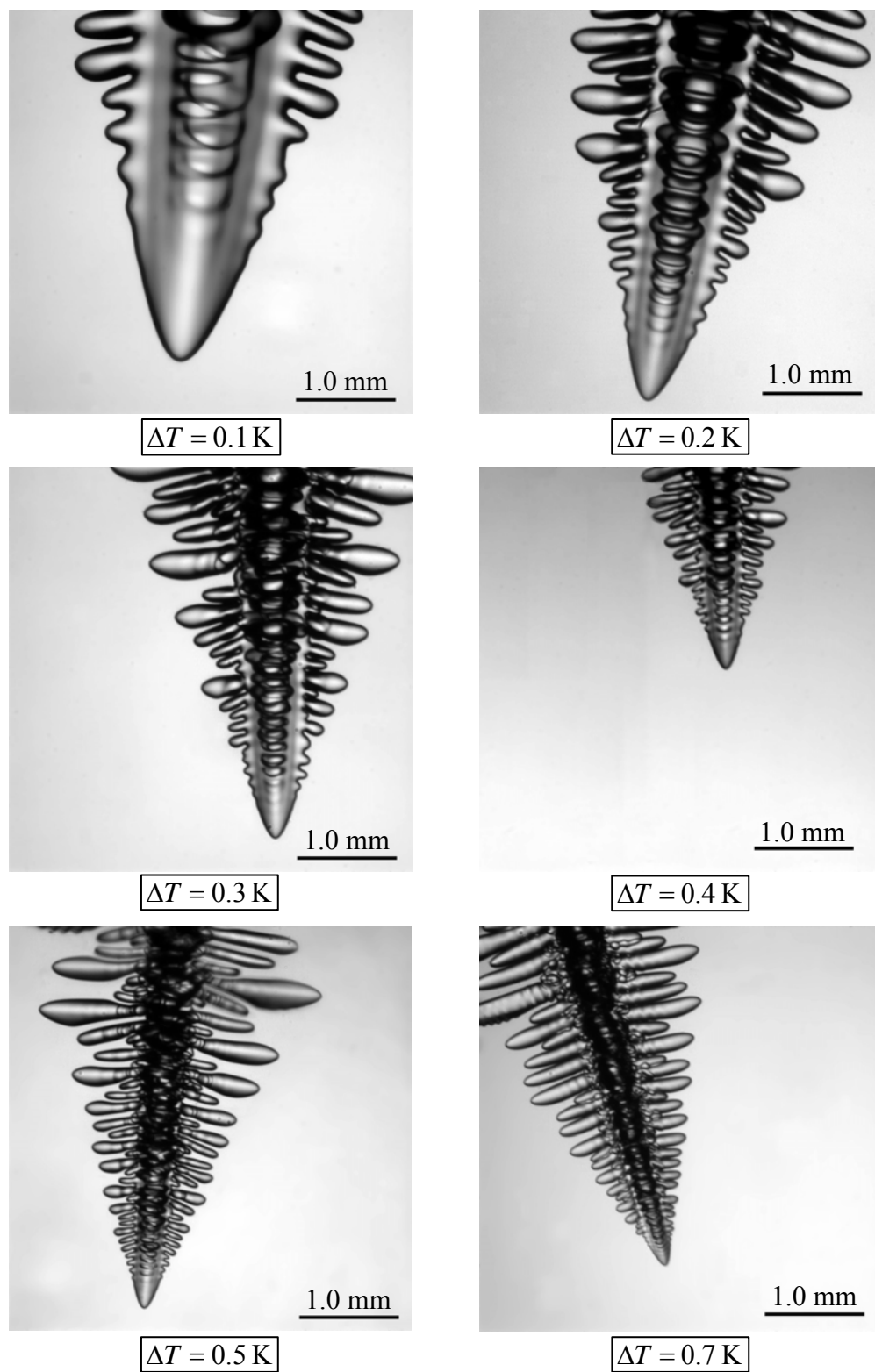
Figure 4.1: Micrographs of almost pure SCN dendrites $\left(C_0 = 0.0086\,\mathrm{mol.\%}\right)$
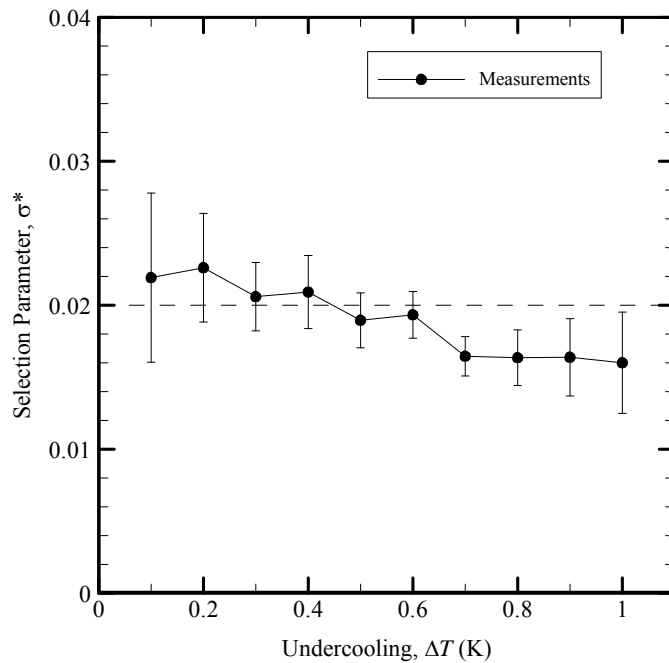
(a)
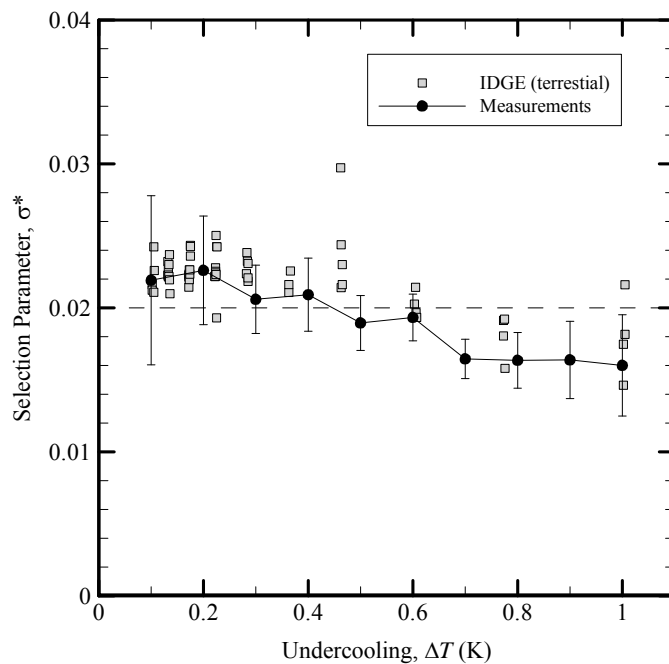
(b)
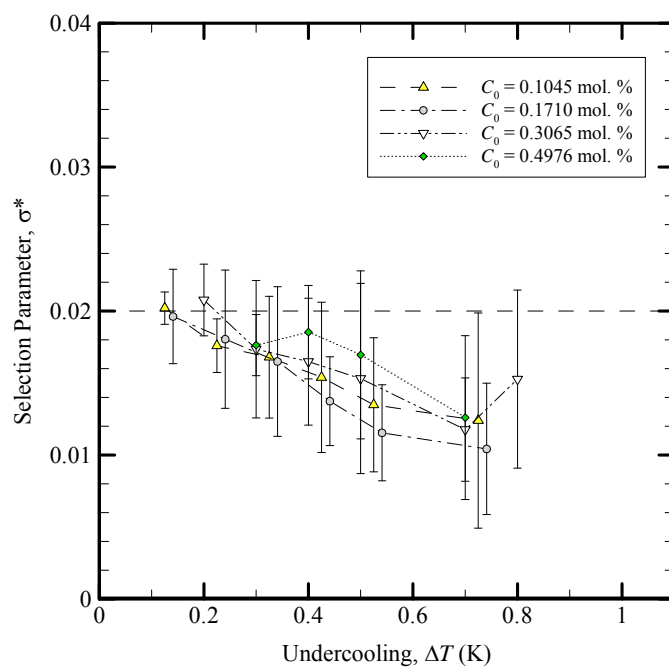
Figure 4.2: Measurements of the selection parameter (σ^*) as a function of the undercooling for almost pure SCN $(C_0 = 0.0086\,\mathrm{mol.\%})$

(a) Comparison with $\sigma^* = 0.02$

(b) Comparison with the experimental benchmark by Glicksman et al.
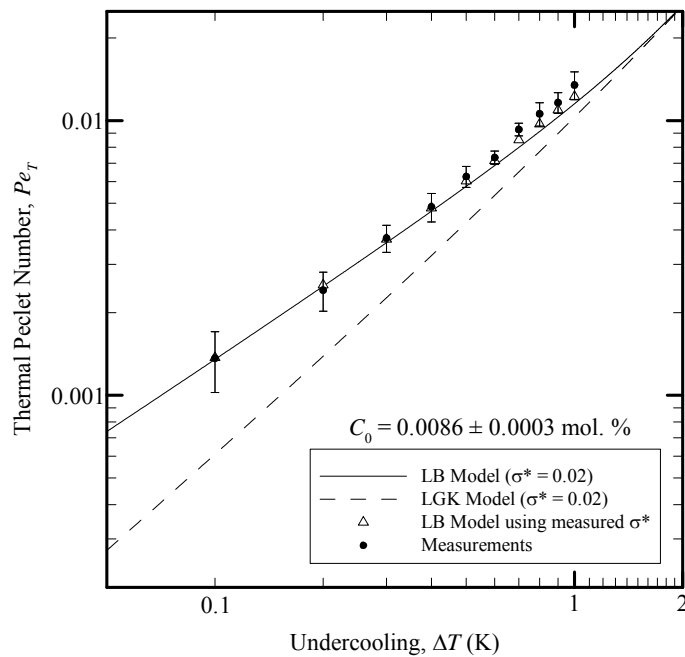
(a)
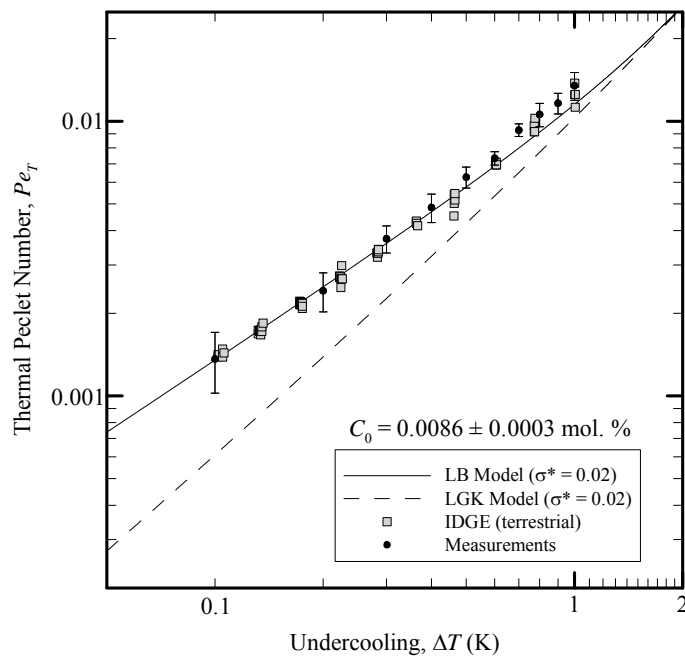
(b)

Figure 4.3: Measurements of the thermal Peclet number as a function of the undercooling for almost pure SCN $\left(C_0 = 0.0086 \,\text{mol}\,\%\right)$.

(a) Comparison with the existing theoretical models.
(b) Comparison with the experimental benchmark by Glicksman et al.
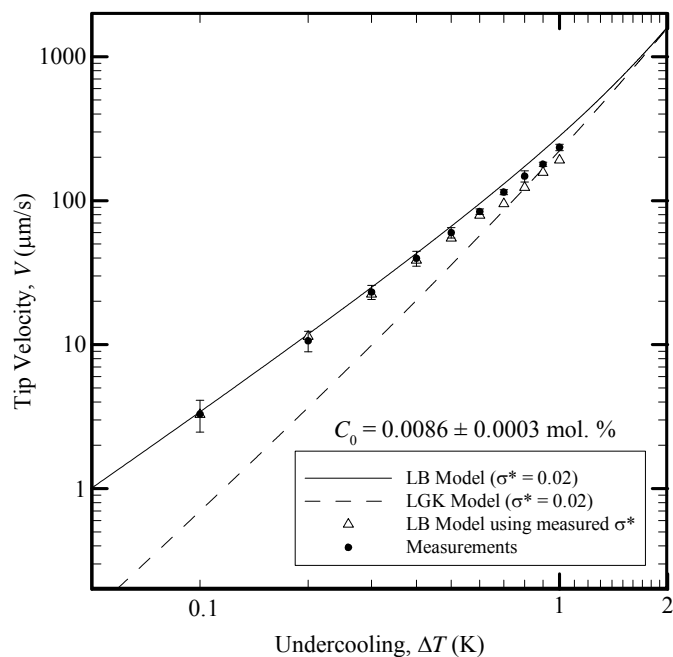
(a)
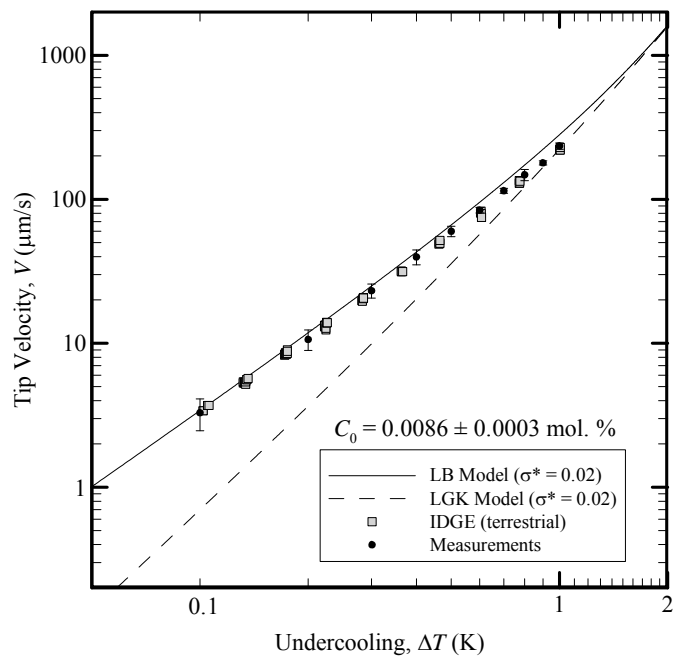
(b)

Figure 4.4: Measurements of the tip velocities as a function of the undercooling for almost pure SCN $\left(C_0 = 0.0086 \, \text{mol.} \% \right)$.

    (a) Comparison with the existing theoretical models

    (b) Comparison with the experimental benchmark by Glicksman et al.
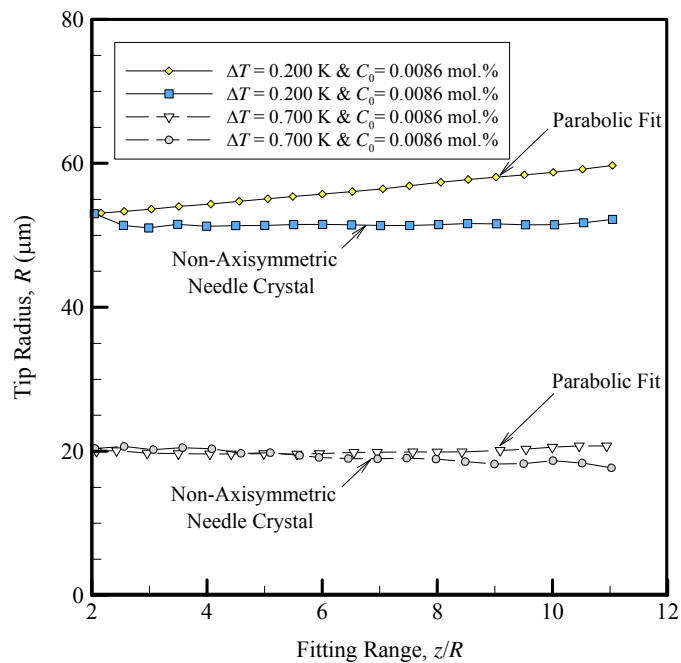
(a)
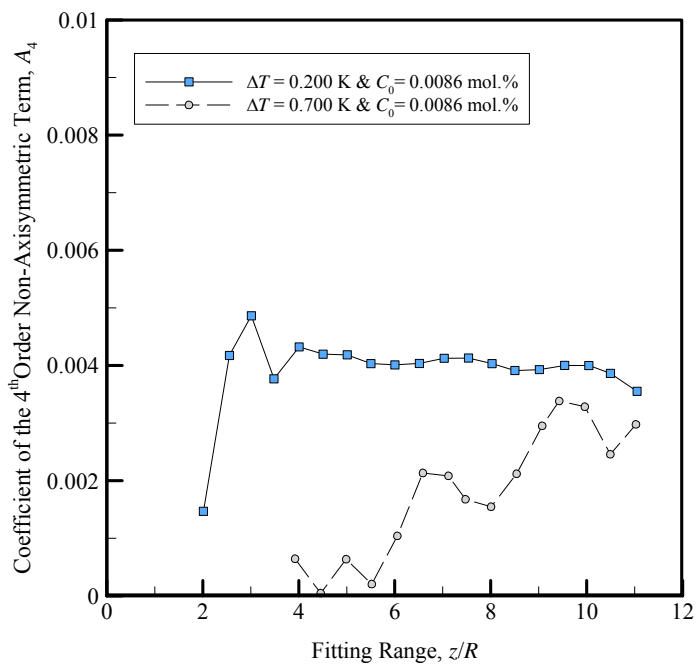
(b)

Figure 4.5: Tip measurements as a function of the fitting range for almost pure SCN $\left(C_0 = 0.0086\,\text{mol.}\%\right)$

    (a) Tip radius

    (b) Coefficient of the 4$^{\text{th}}$ order non-axisymmetric term A_4
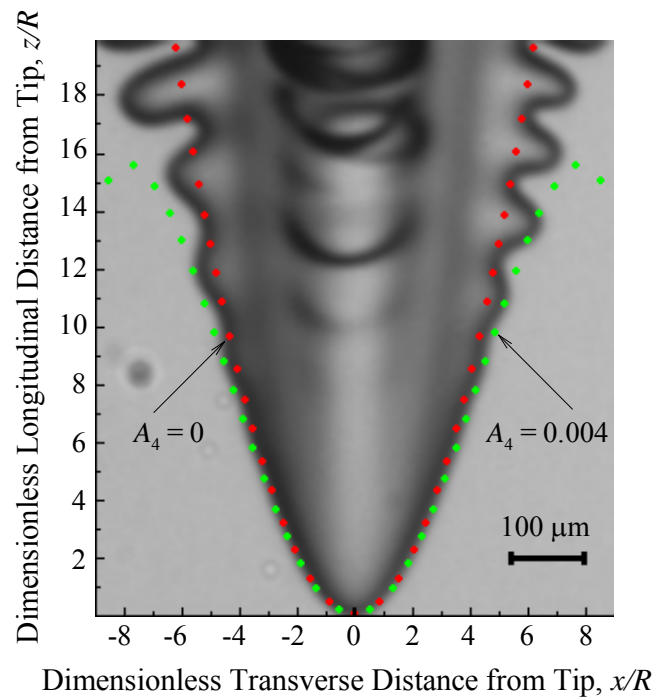
Figure 4.6: Verification of the MST for almost pure SCN $\left(C_0 = 0.0086\,\text{mol.\%}\; .\&\; \Delta T = 0.300\,\text{K}\right)$

(a)

(b)
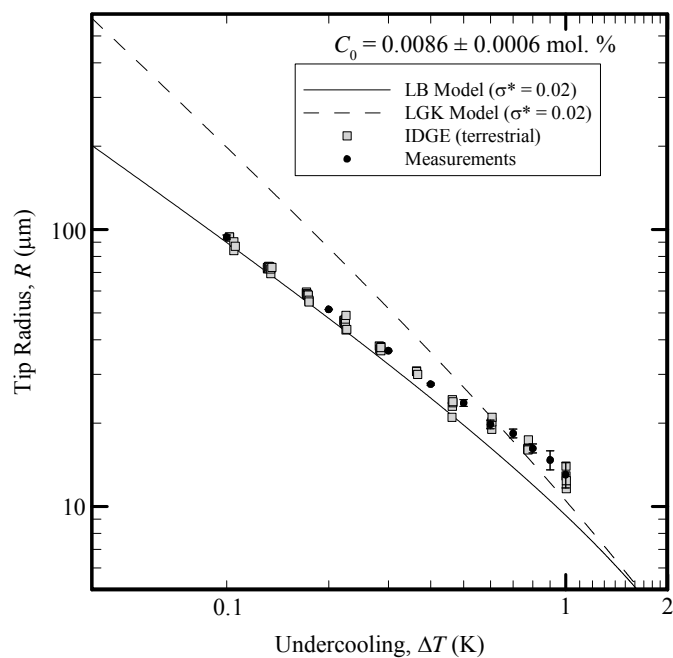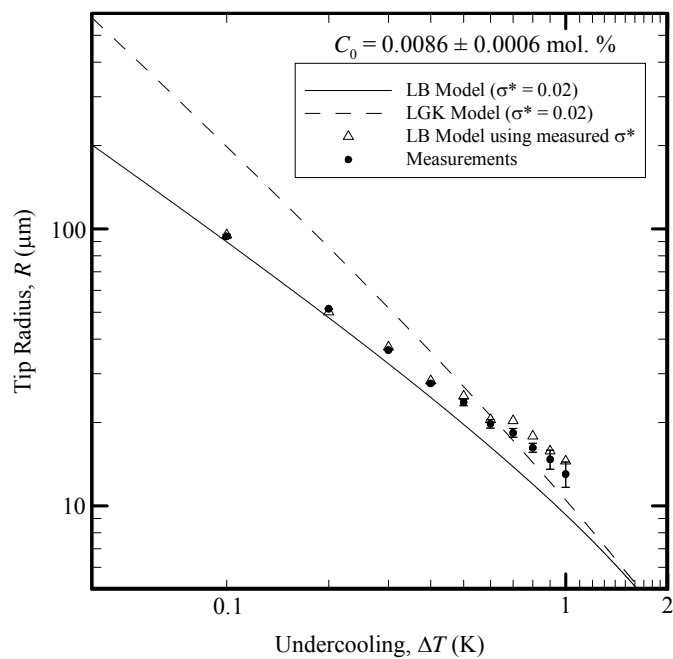
Figure 4.7: Tip radius measurements as a function of the undercooling for almost pure SCN $\left(C_0 = 0.0086 \, \text{mol.} \% \right)$.

(a) Comparison with the existing theoretical models

(b) Comparison with the experimental benchmark by Glicksman et al.
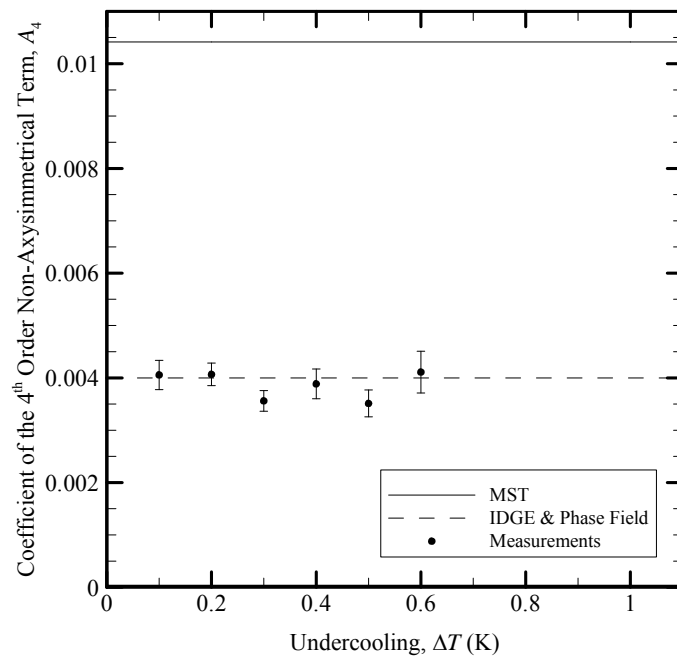
Figure 4.8: Tip radius measurements as a function of the undercooling for almost pure SCN $\left(C_0 = 0.0086\,\text{mol.}\%\right)$.
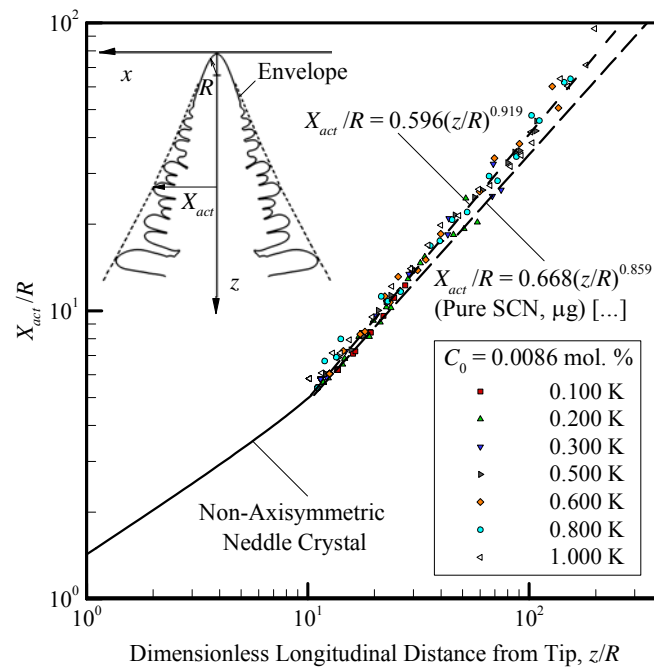
Figure 4.9: Dendrite's envelope as a function of the longitudinal distance from tip for almost pure SCN $\left(C_0 = 0.0086\,\text{mol.}\%\right)$
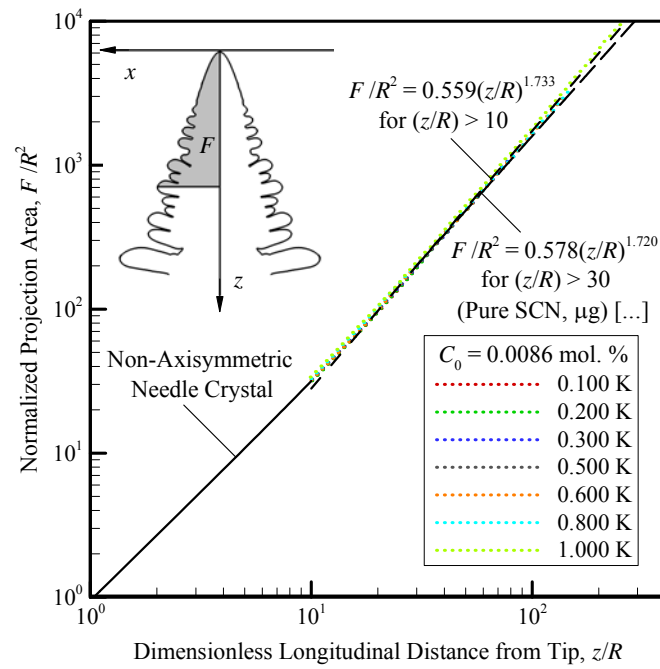
Figure 4.10: Projection area as a function of the longitudinal distance from tip for almost pure SCN $\left(C_0 = 0.0086 \, \text{mol.} \% \right)$.
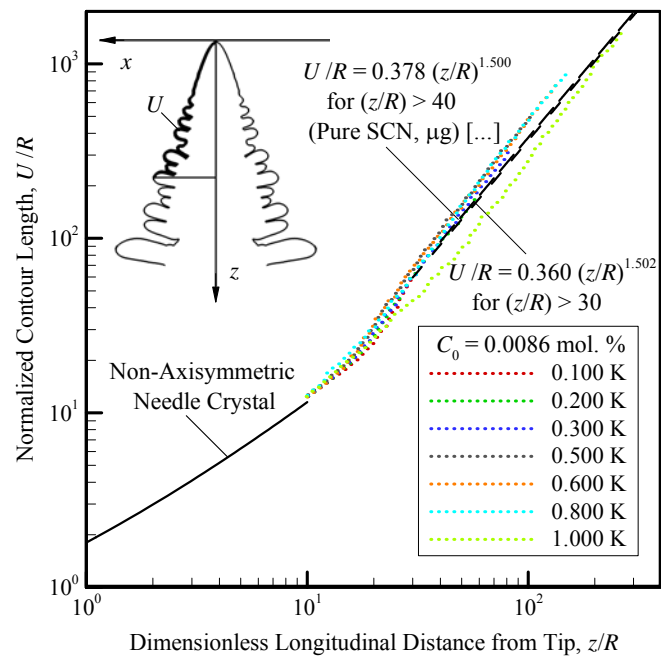
Figure 4.11: Contour length as a function of the longitudinal distance from tip for almost pure SCN $(C_0 = 0.0086\,\text{mol.}\%)$.
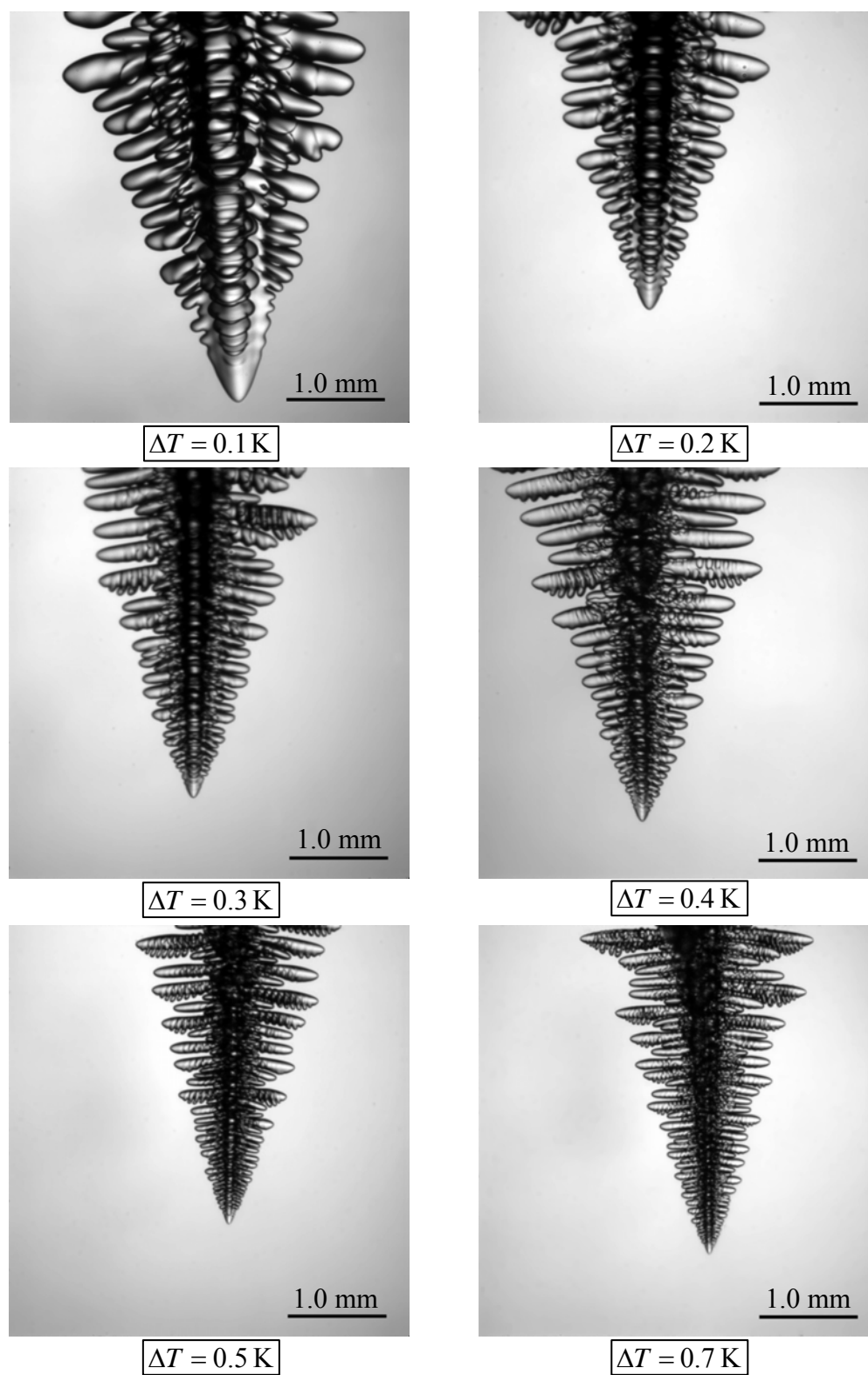
Figure 4.12: Micrographs of SCN-ACE dendrites $\left(C_0 = 0.1045\,\text{mol.\%}\right)$.
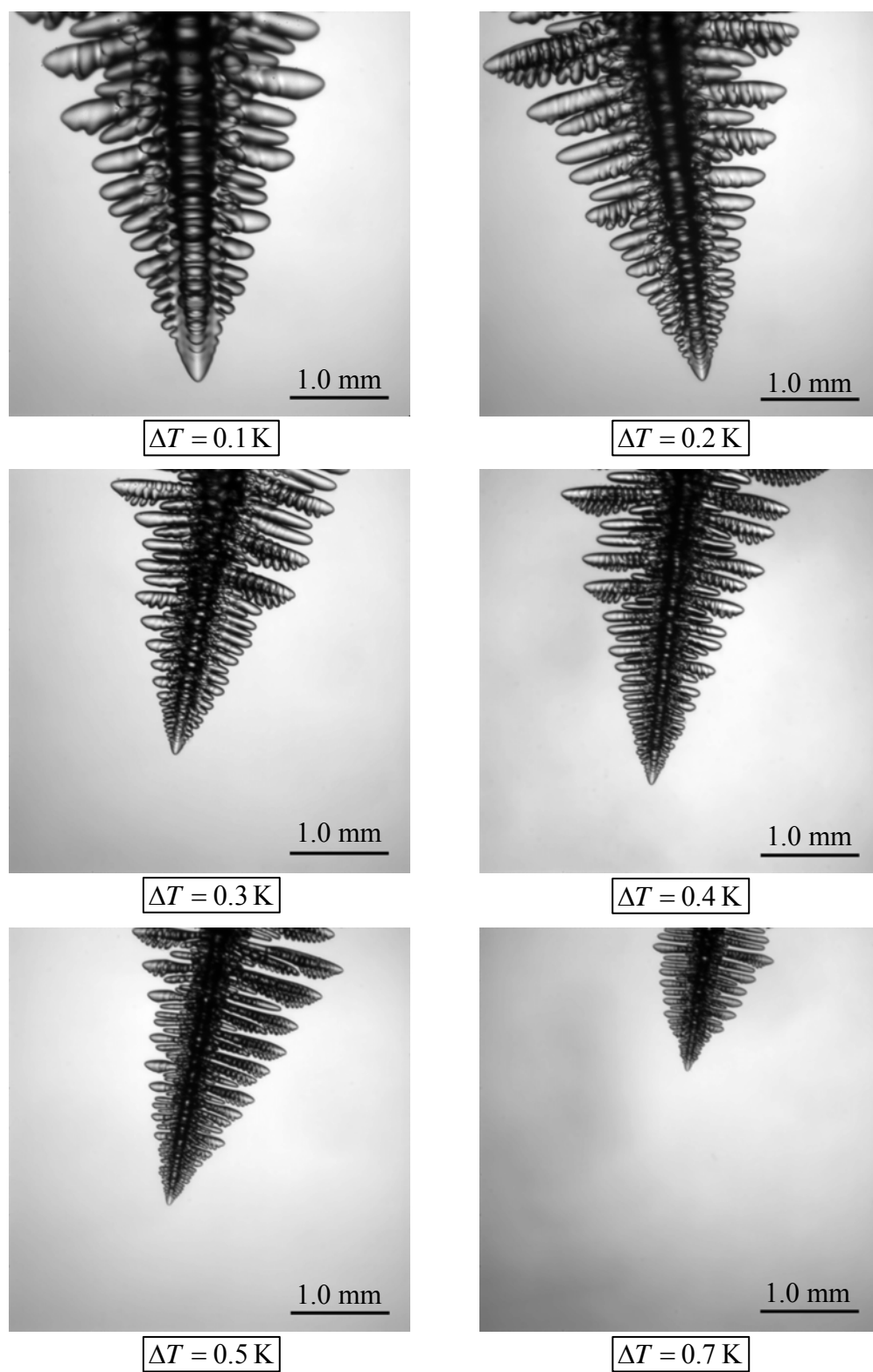
Figure 4.13: Micrographs of SCN-ACE dendrites $\left(C_0 = 0.1710 \, \text{mol.} \% \right)$.
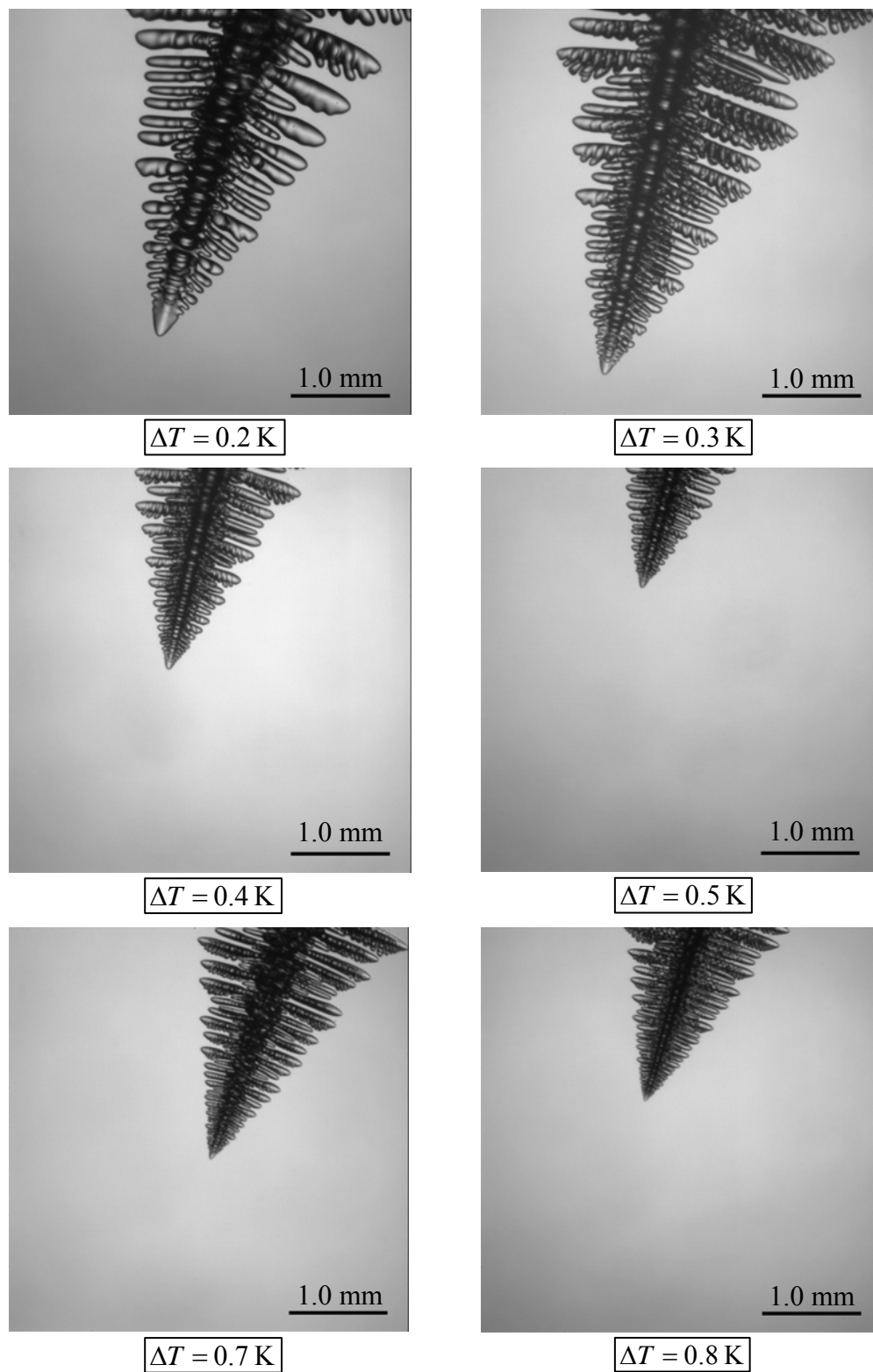
Figure 4.14: Micrographs of SCN-ACE dendrites $\left(C_0 = 0.3065\,\text{mol.}\%\right)$.
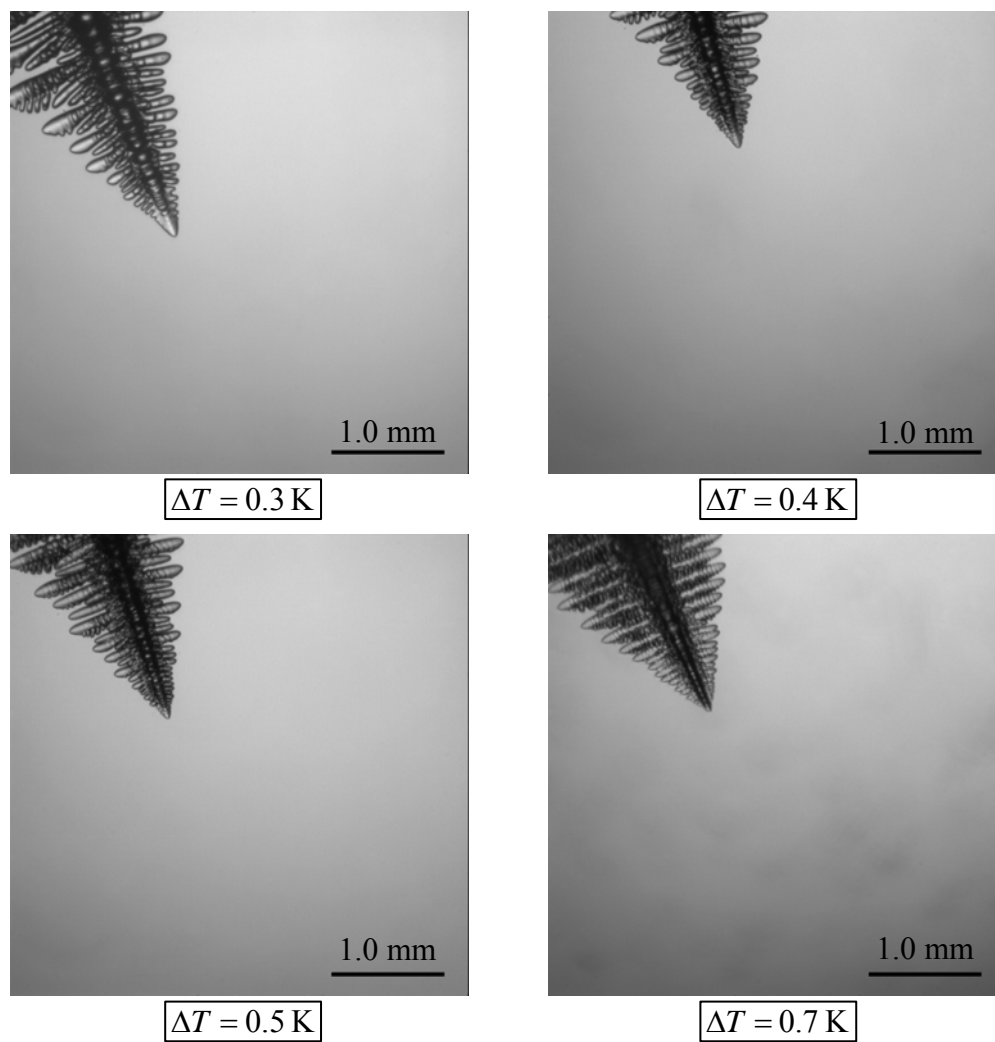
Figure 4.15: Micrographs of SCN-ACE dendrites $\left(C_0 = 0.4976.\%\right)$.

Figure 4.16: Measurements of the selection parameter $\left(\sigma^*\right)$ as a function of the undercooling for SCN-Acetone alloys.
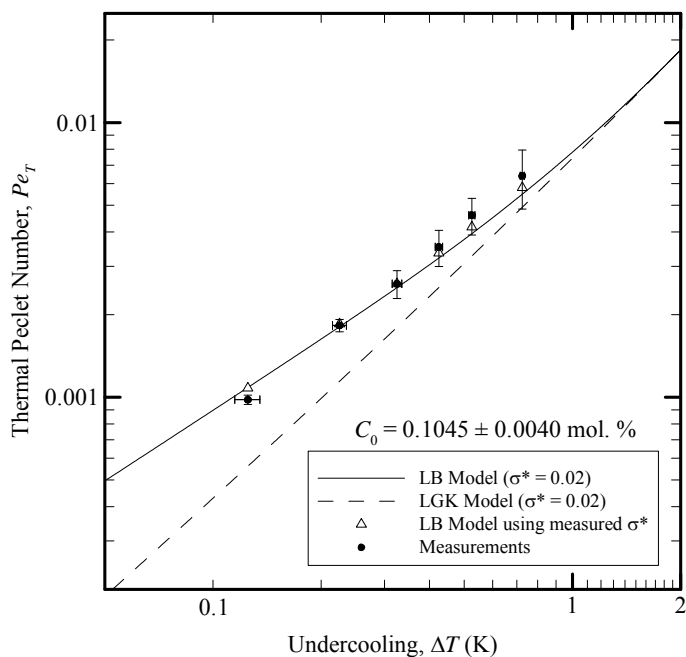
(a)
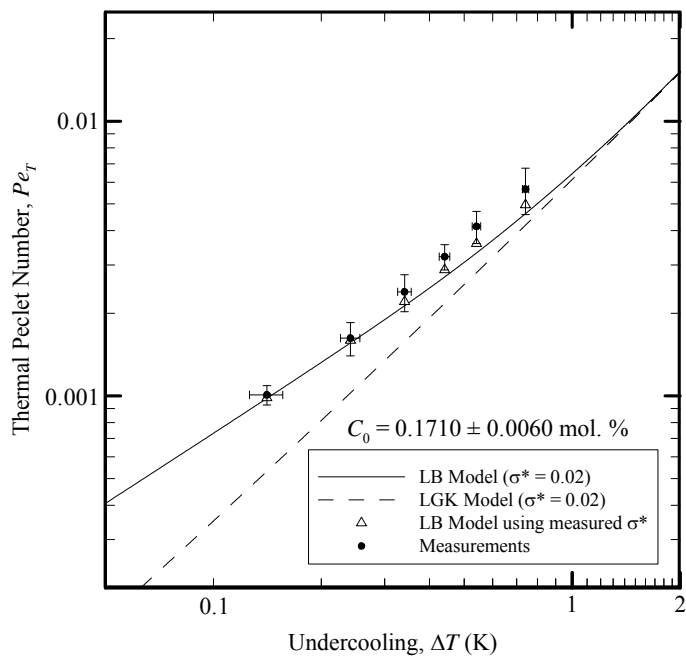
(b)

Figure 4.17: Measurements of the thermal Peclet number as a function of the undercooling for SCN-Acetone alloys.

(a) $C_0 = 0.1045 \, \text{mol} \, \%$.

(b) $C_0 = 0.1710 \, \text{mol} \, \%$.
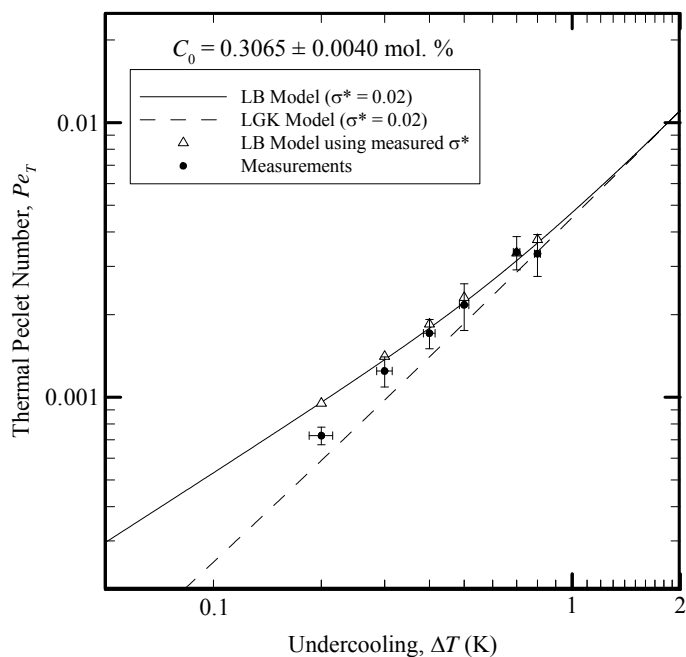
(a)
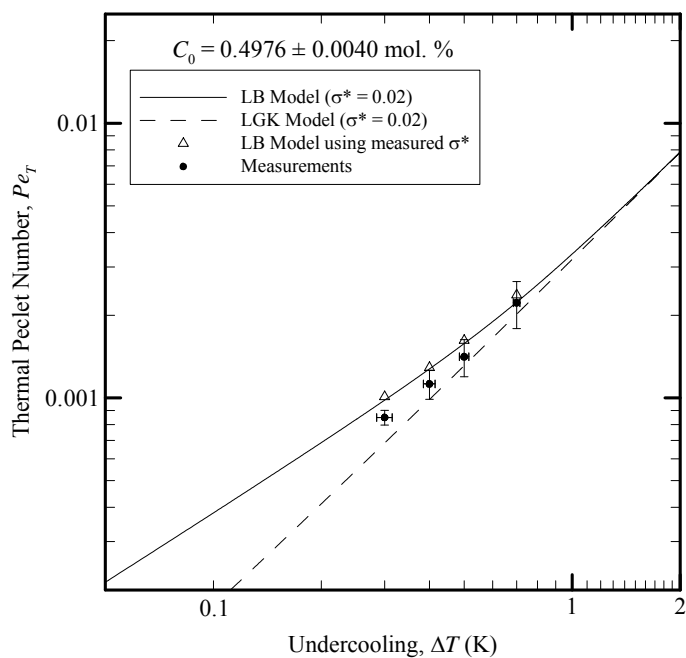
(b)

Figure 4.18: Measurements of the thermal Peclet number as a function of the undercooling for SCN-Acetone alloys.

(a) $C_0 = 0.3065\,\text{mol}\,\%$.

(b) $C_0 = 0.4976\,\text{mol}\,\%$.
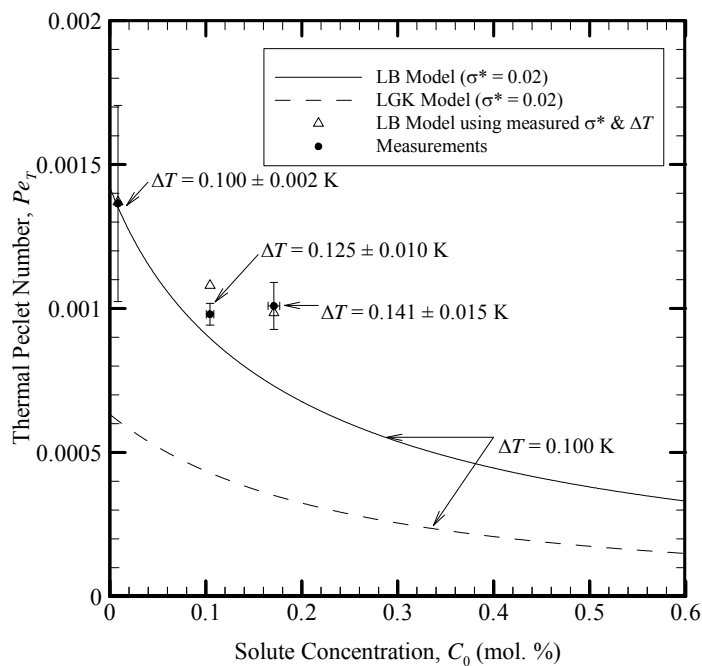
(a)
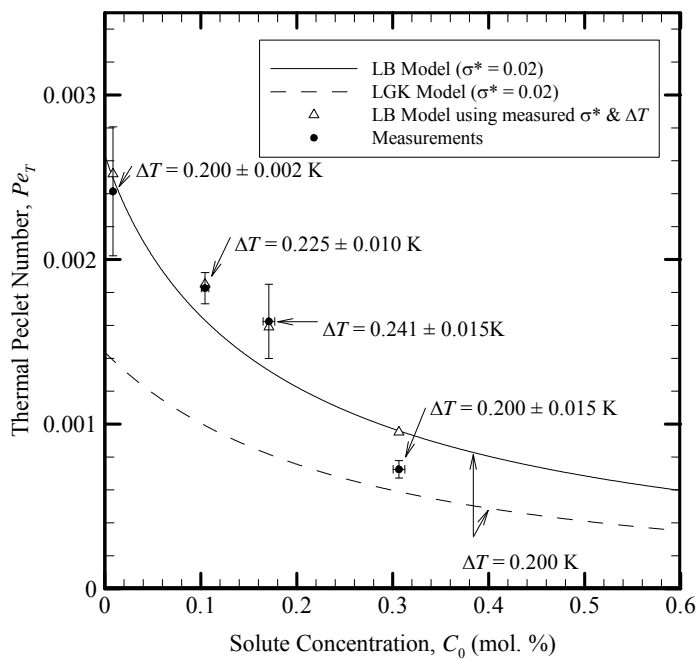
(b)

Figure 4.19: Measurements of the thermal Peclet number as a function of the solute concentration for SCN-Acetone alloys.

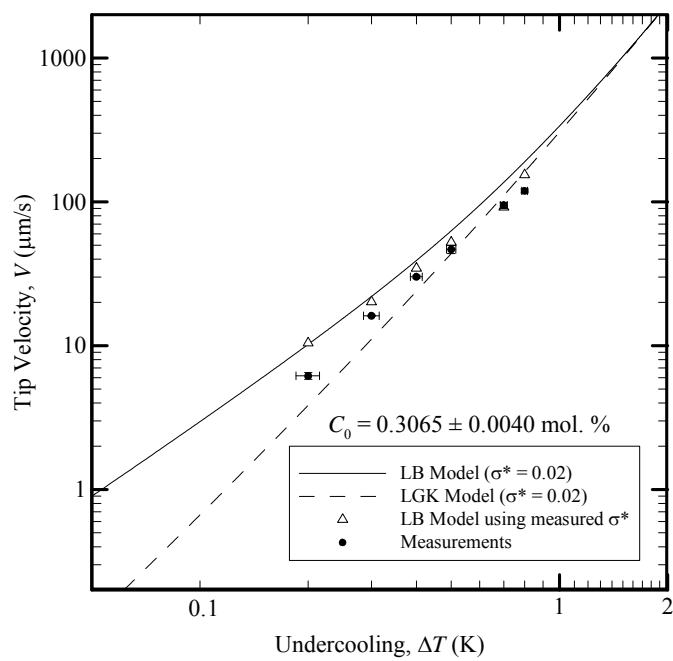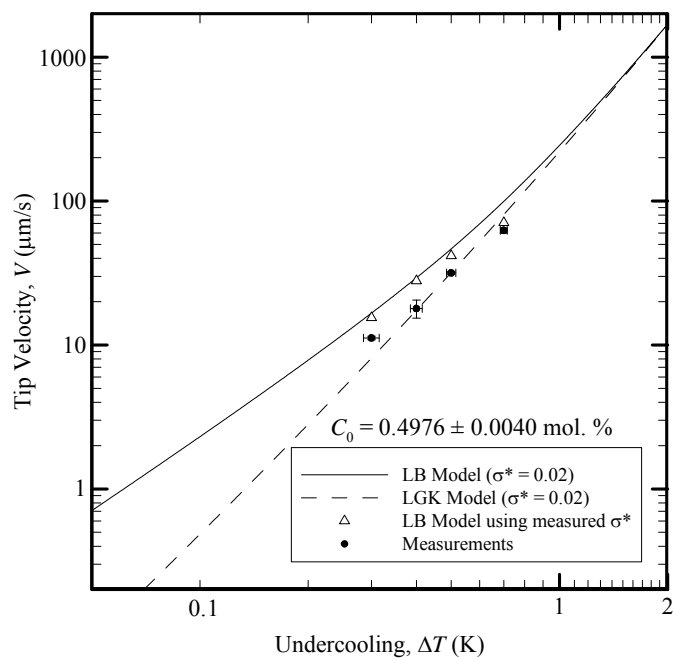(a) $\Delta T \approx 0.100\,\text{K}$.

(b). $\Delta T \approx 0.200\,\text{K}$.
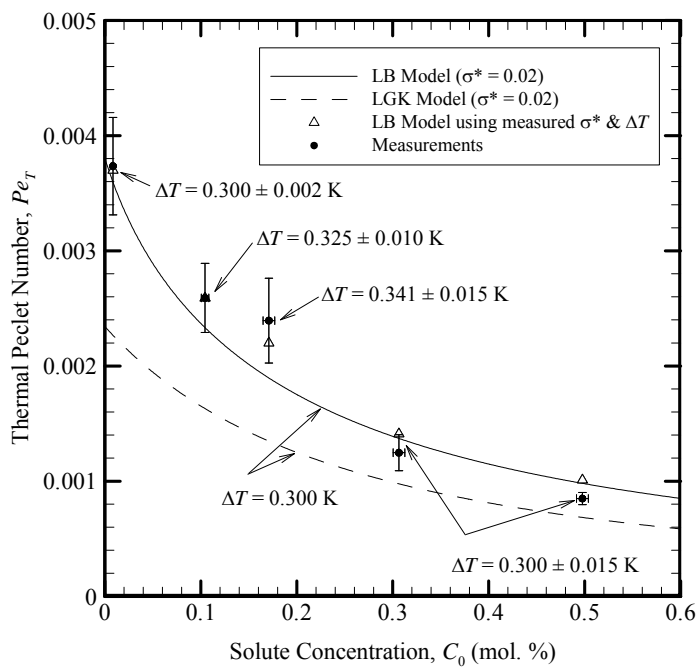
(a)
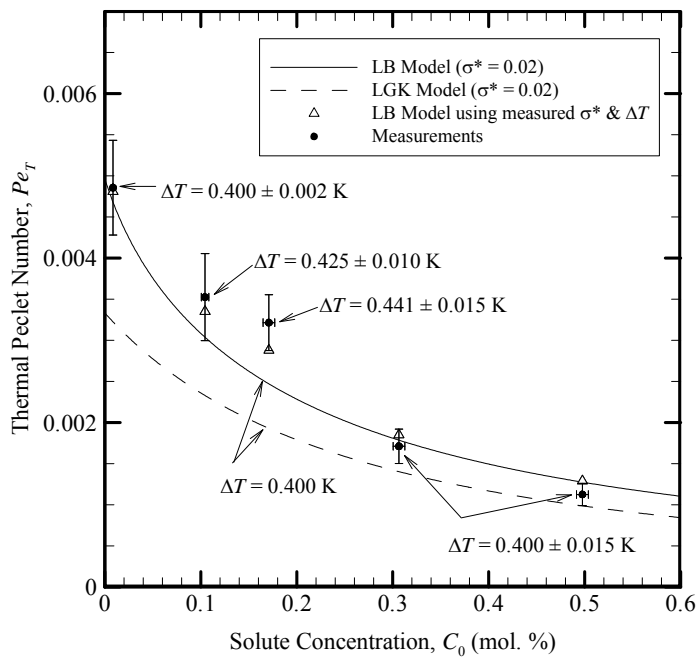
(b)

Figure 4.20: Measurements of the thermal Peclet number as a function of the solute concentration for SCN-Acetone alloys.

(a) $\Delta T \approx 0.300\,\text{K}$.

(b). $\Delta T \approx 0.400\,\text{K}$.
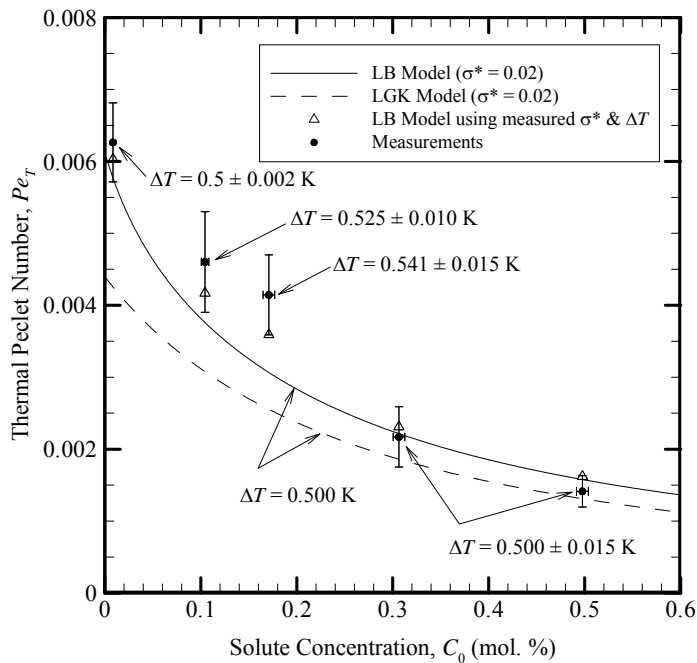
(a)
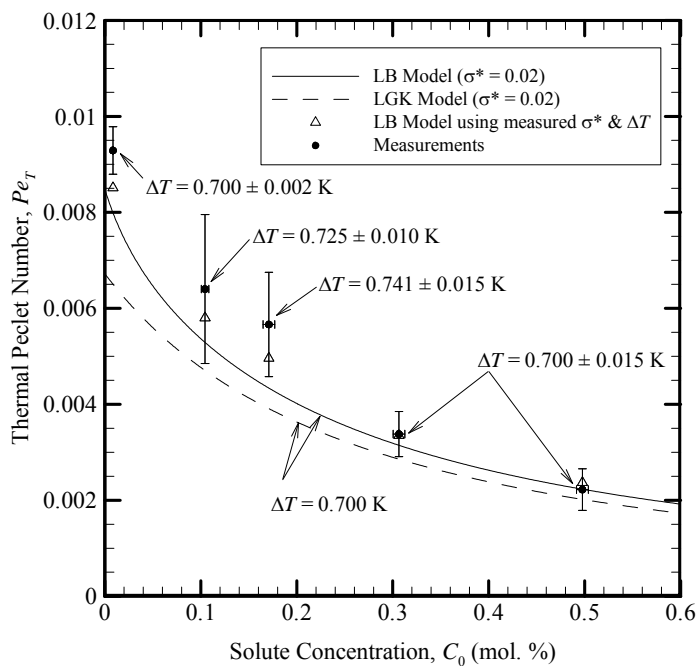
(b)

Figure 4.21: Measurements of the thermal Peclet number as a function of the solute concentration for SCN-Acetone alloys.

(a) $\Delta T \approx 0.500\,\text{K}$.

(b). $\Delta T \approx 0.700\,\text{K}$.
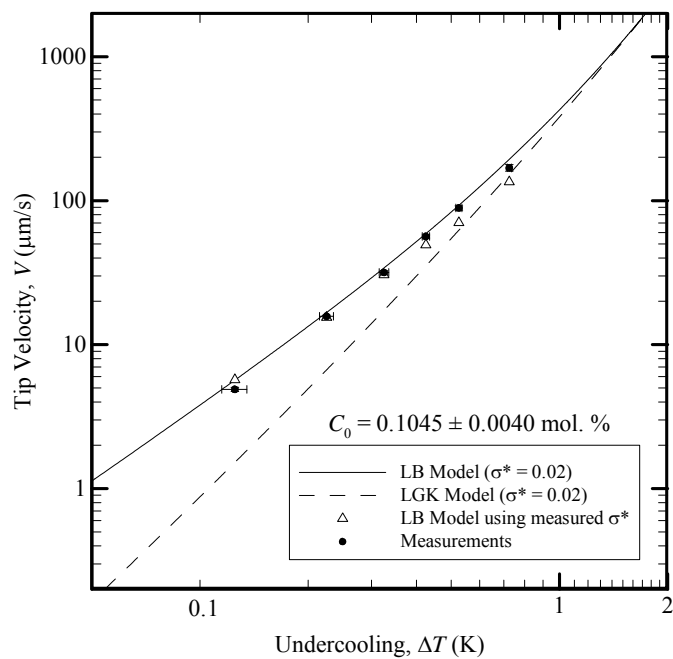
(a)
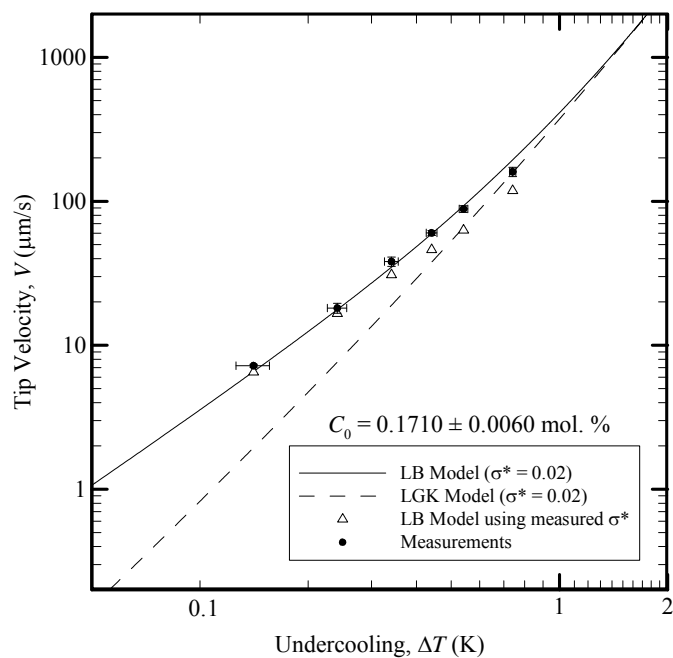
(b)

Figure 4.22: Measurements of the tip velocity as a function of the undercooling for SCN-Acetone alloys.

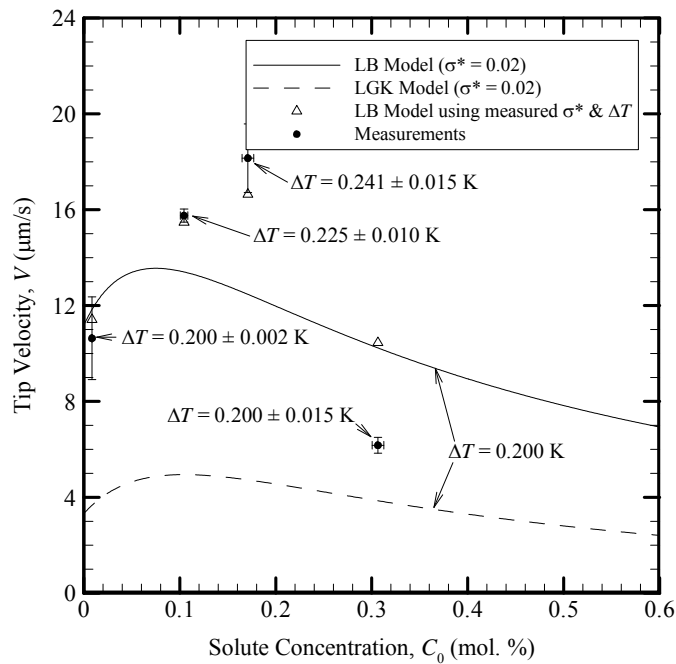(a) $C_0 = 0.1045 \, \text{mol} \, \%$.

(b) $C_0 = 0.1710 \, \text{mol} \, \%$.

(a)

(b)

Figure 4.23: Measurements of the tip velocity as a function of the undercooling for SCN-Acetone alloys.

(a) $C_0 = 0.3065 \, \text{mol} \, \%$.
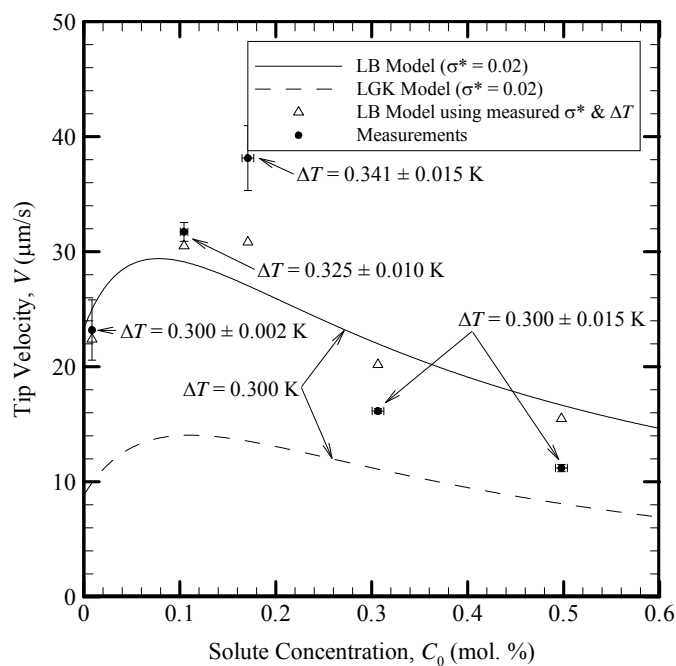
(b) $C_0 = 0.4976 \, \text{mol} \, \%$.
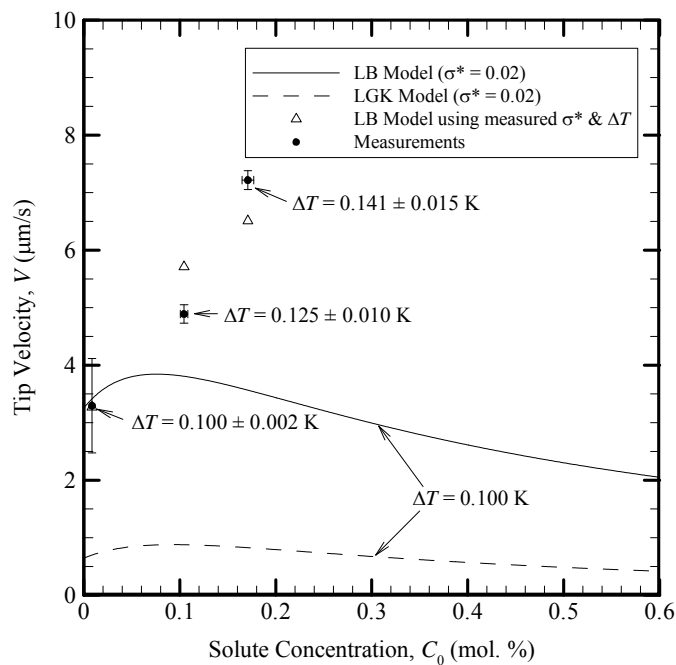
(a)

(b)

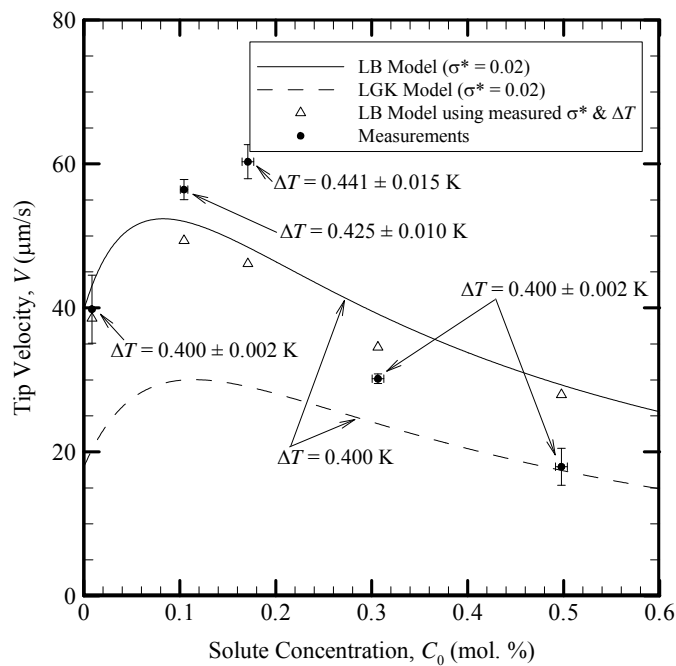Figure 4.24: Measurements of the tip velocity as a function of the solute concentration for SCN-Acetone alloys.
     (a) $\Delta T \approx 0.100\,\text{K}$.
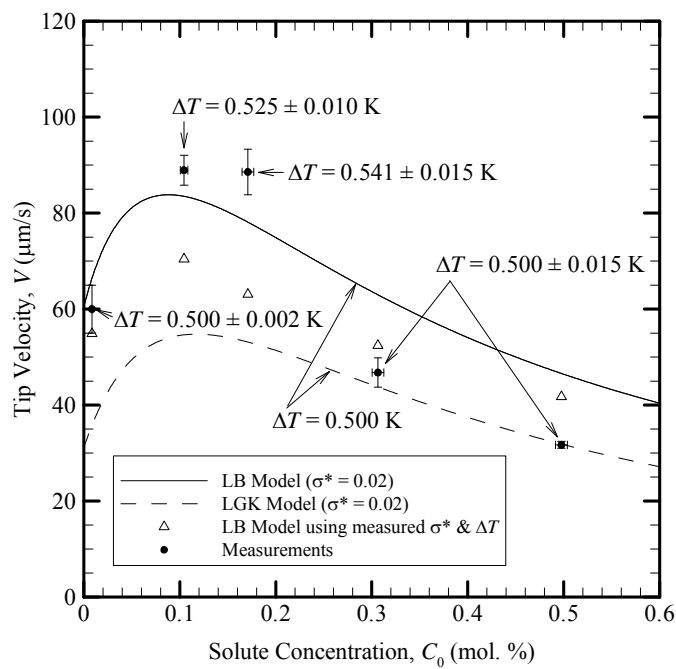   (b). $\Delta T \approx 0.200\,\text{K}$.

(a)

(b)
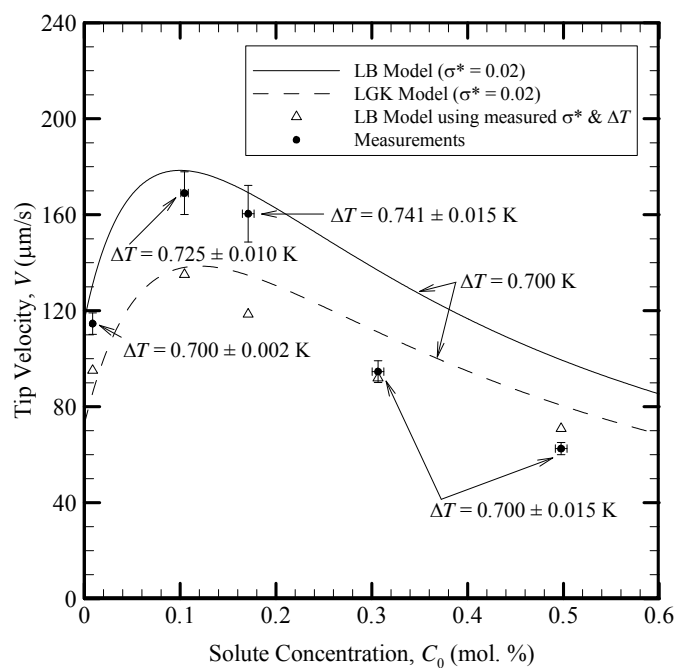
Figure 4.25: Measurements of the tip velocity as a function of the solute concentration for SCN-Acetone alloys.
(a) $\Delta T \approx 0.300\,\mathrm{K}$.
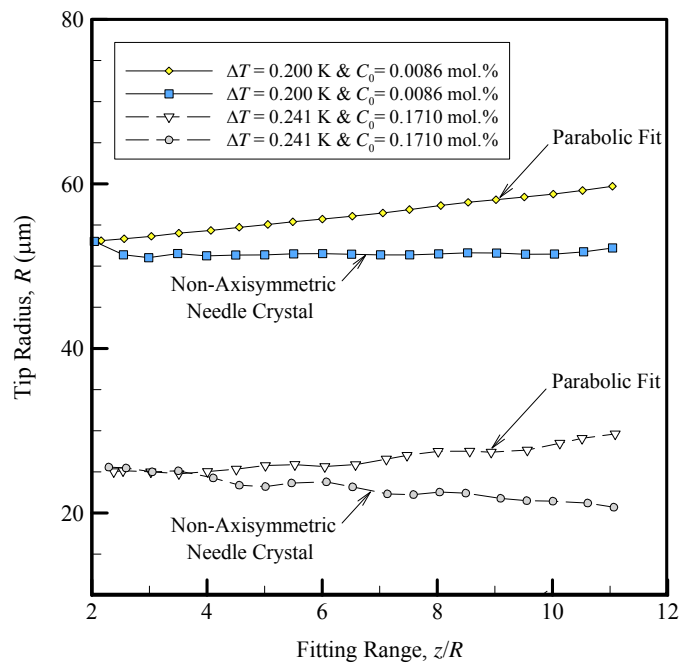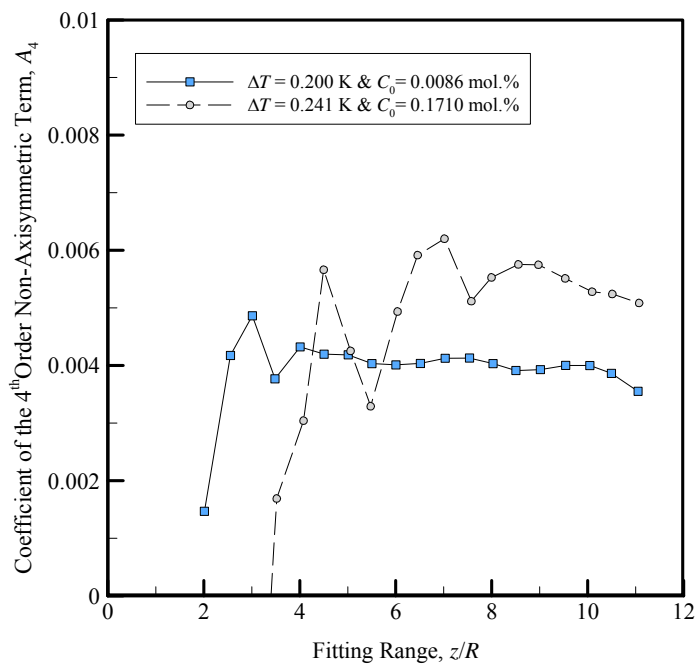(b). $\Delta T \approx 0.400\,\mathrm{K}$.

(a)

(b)

Figure 4.26: Measurements of the tip velocity as a function of the solute concentration for SCN-Acetone alloys.

     (a) $\Delta T \approx 0.500\,\mathrm{K}$.

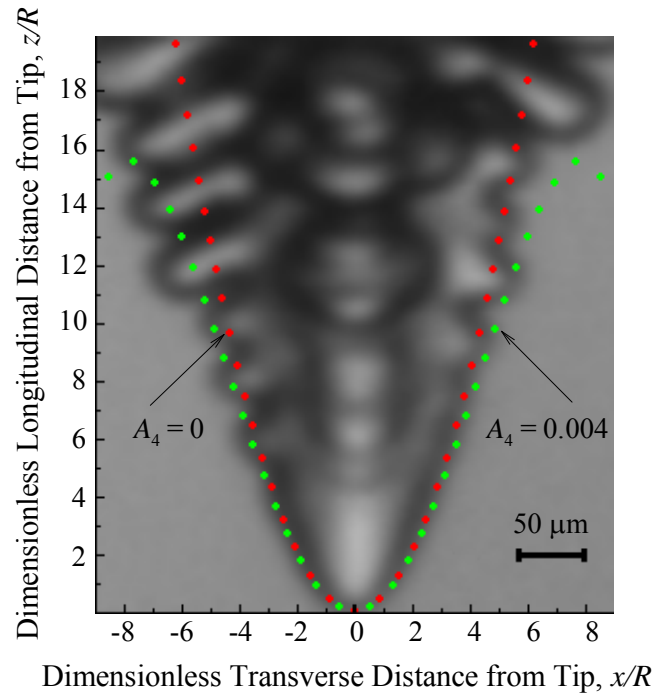   (b). $\Delta T \approx 0.700\,\mathrm{K}$.

(a)
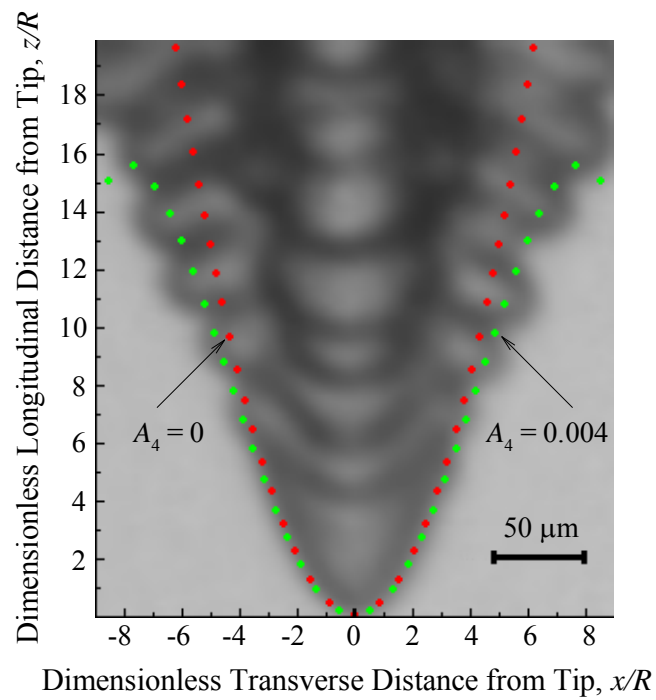

(b)

Figure 4.27: Tip measurements as a function of the fitting range for SCN-Acetone alloys
(a) Tip radius
(b) Coefficient of the 4th order non-axisymmetric term A_4

(a)

(b)

Figure 4.28: Verification of the MST for SCN-Acetone alloys.
(a) $C_0 = 0.1045 \, \text{mol}\% \ \& \ \Delta T = 0.325 \, \text{K}$.
(b). $C_0 = 0.1710 \, \text{mol}\% \ \& \ \Delta T = 0.341 \, \text{K}$.
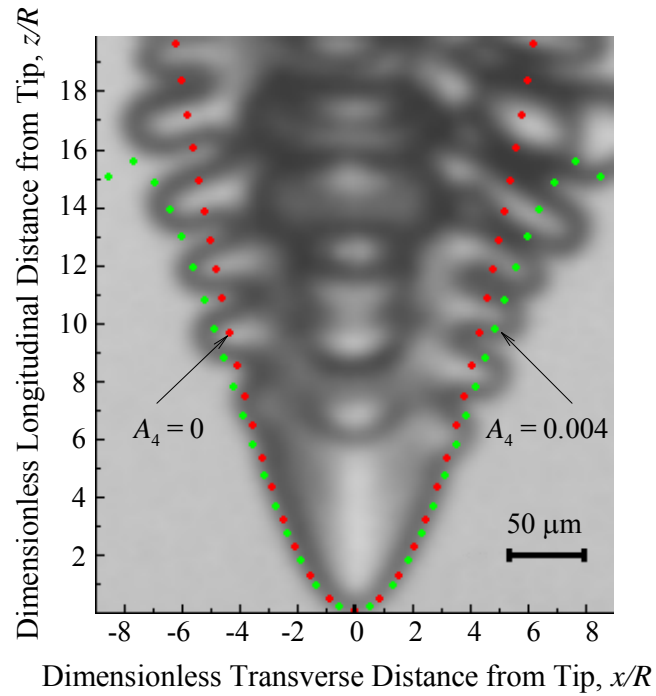
(a)
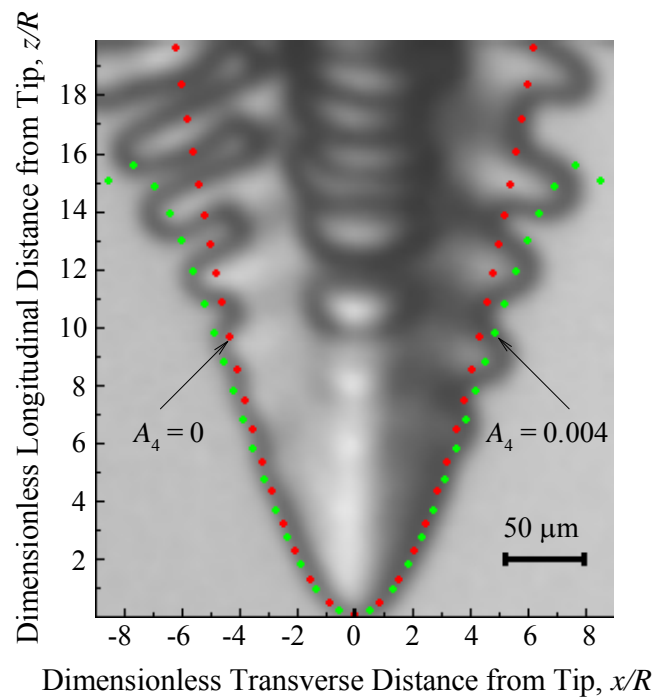
(b)

Figure 4.29: Verification of the MST for SCN-Acetone alloys.

(a) $C_0 = 0.3065\,\text{mol\%}$ & $\Delta T = 0.300\,\text{K}$.

(b). $C_0 = 0.4976\,\text{mol\%}$ & $\Delta T = 0.300\,\text{K}$.
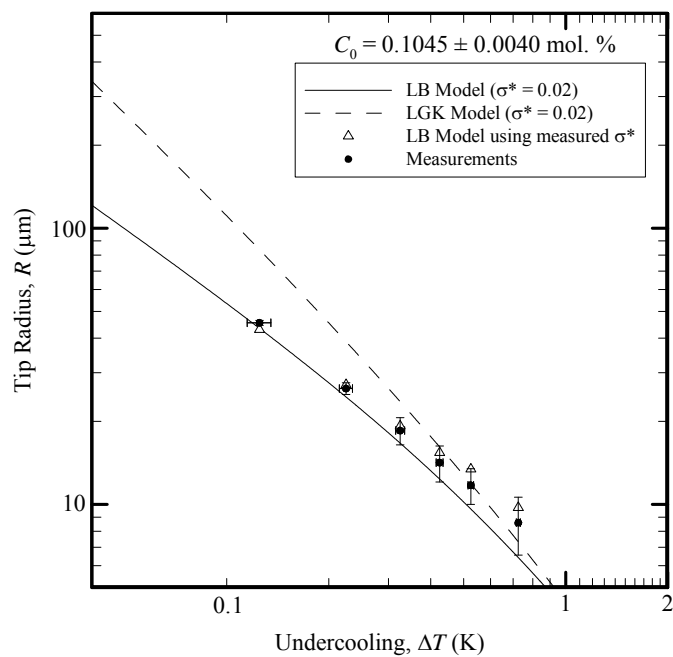
(a)
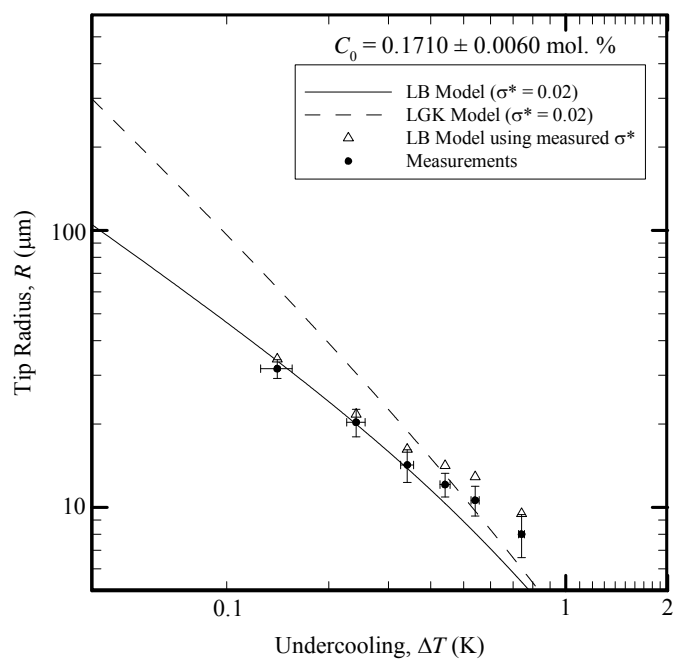
(b)

Figure 4.30: Measurements of the tip radius as a function of the undercooling for SCN-Acetone alloys.

     (a) $C_0 = 0.1045\,\text{mol}\,\%$.

     (b) $C_0 = 0.1710\,\text{mol}\,\%$.
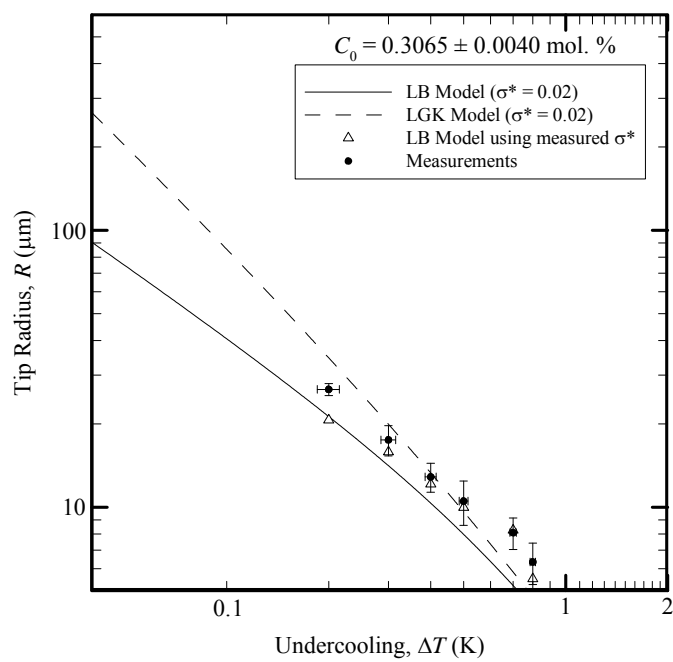
(a)
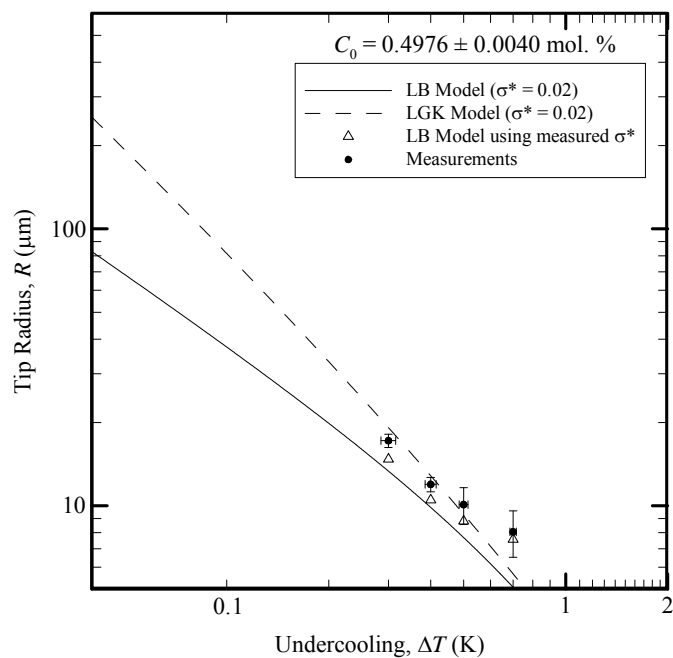
(b)

Figure 4.31: Measurements of the tip radius as a function of the undercooling for SCN-Acetone alloys.

(a) $C_0 = 0.3065\,\text{mol}\,\%$.

(b) $C_0 = 0.4976\,\text{mol}\,\%$.
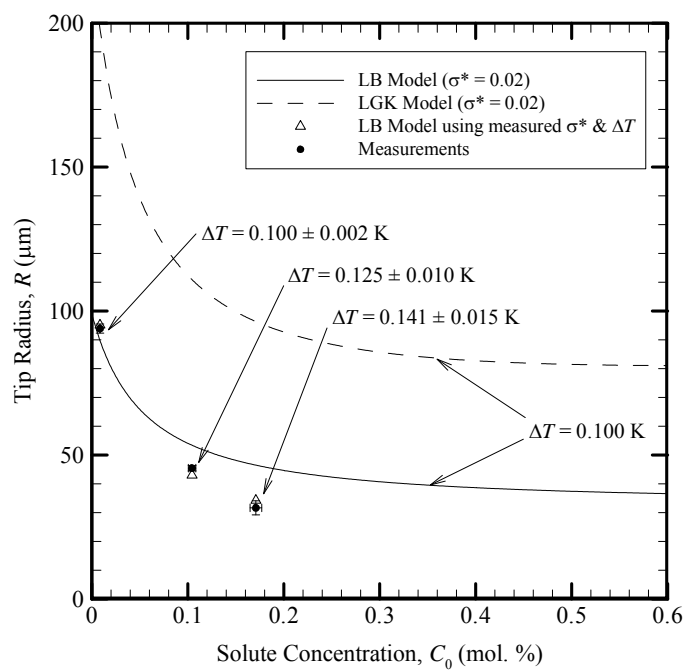
(a)
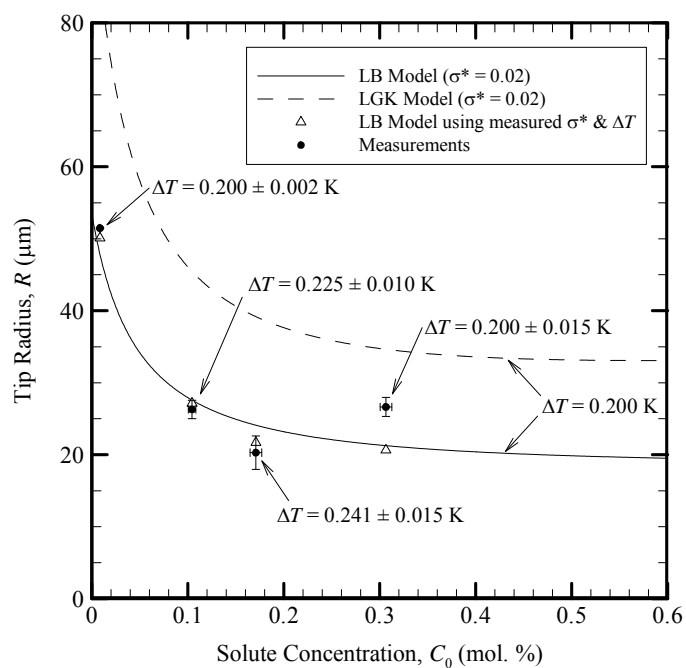
(b)

Figure 4.32: Measurements of the tip radius as a function of the solute concentration for SCN-Acetone alloys.
(a) $\Delta T \approx 0.100\,\mathrm{K}$.
(b). $\Delta T \approx 0.200\,\mathrm{K}$.
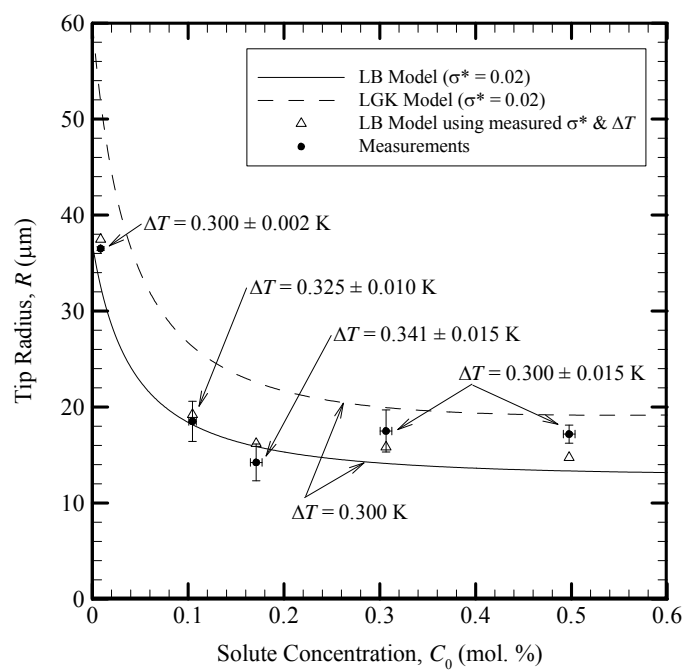
(a)
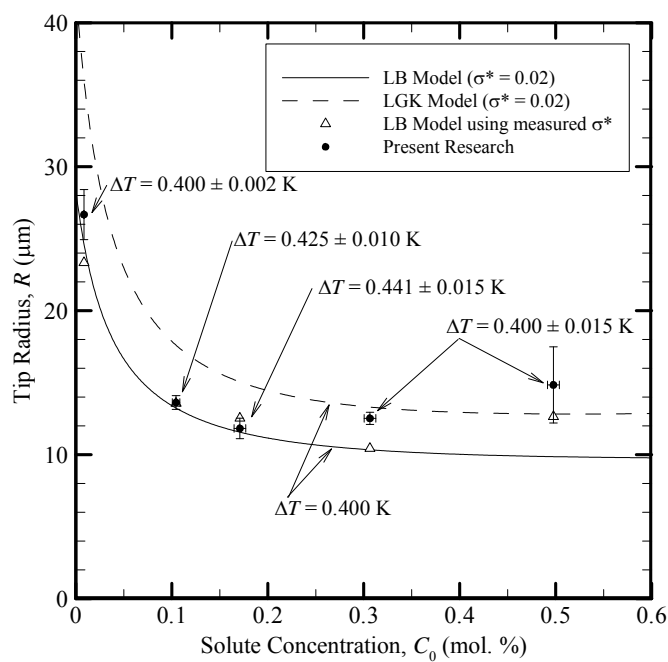
(b)

Figure 4.33: Measurements of the tip radius as a function of the solute concentration for SCN-Acetone alloys.

(a) $\Delta T \approx 0.300\,\mathrm{K}$.

(b). $\Delta T \approx 0.400\,\mathrm{K}$.
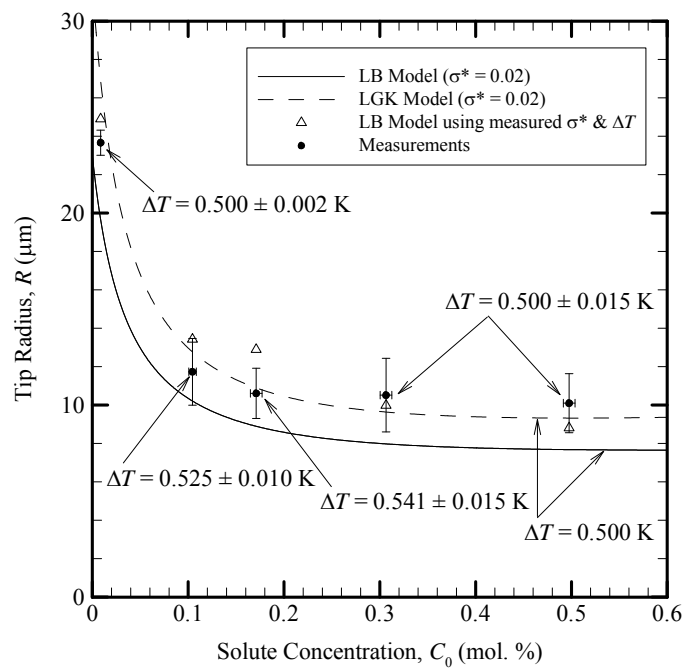
(a)
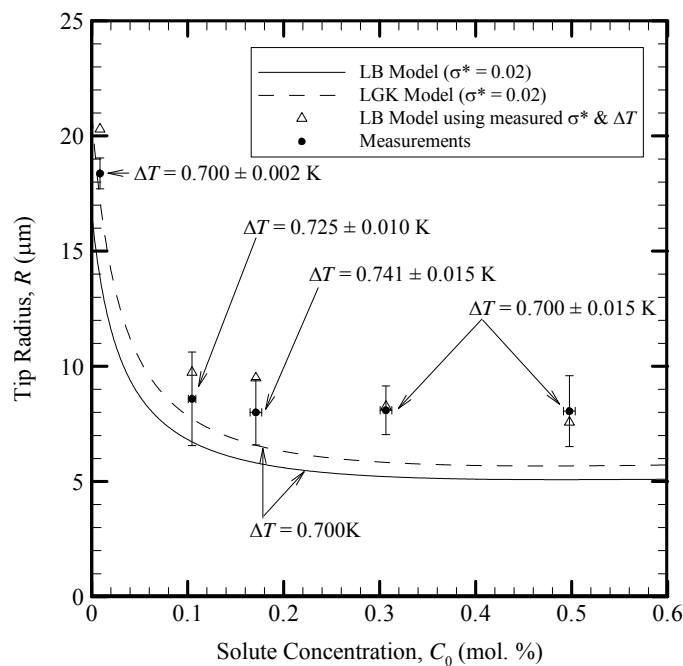
(b)

Figure 4.34: Measurements of the tip radius as a function of the solute concentration for SCN-Acetone alloys.

(a) $\Delta T \approx 0.500\,\text{K}$.

(b). $\Delta T \approx 0.700\,\text{K}$.
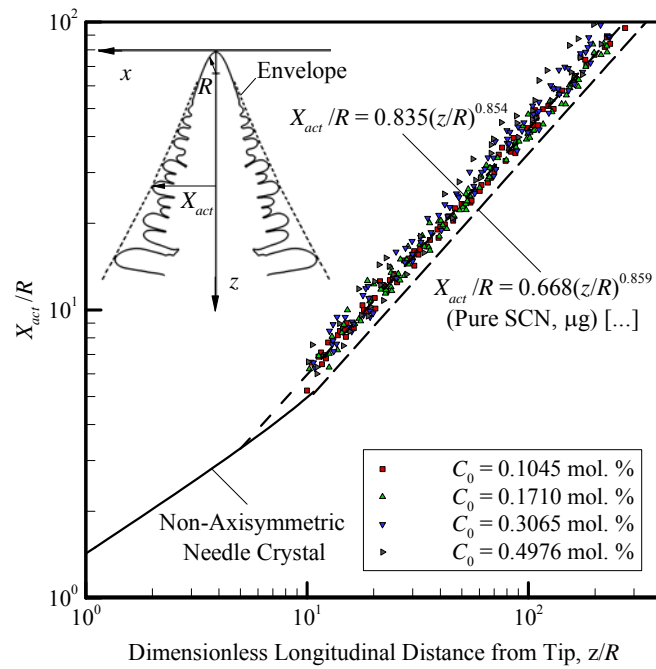
Figure 4.35: Dendrite's envelope as a function of the longitudinal distance from tip for SCN-Acetone alloys.
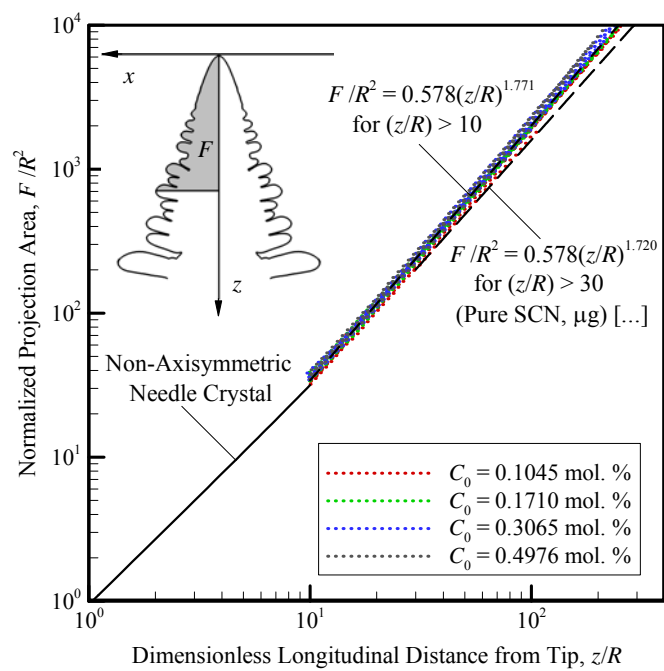
Figure 4.36: Projection area as a function of the longitudinal distance from tip for SCN-Acetone alloys.
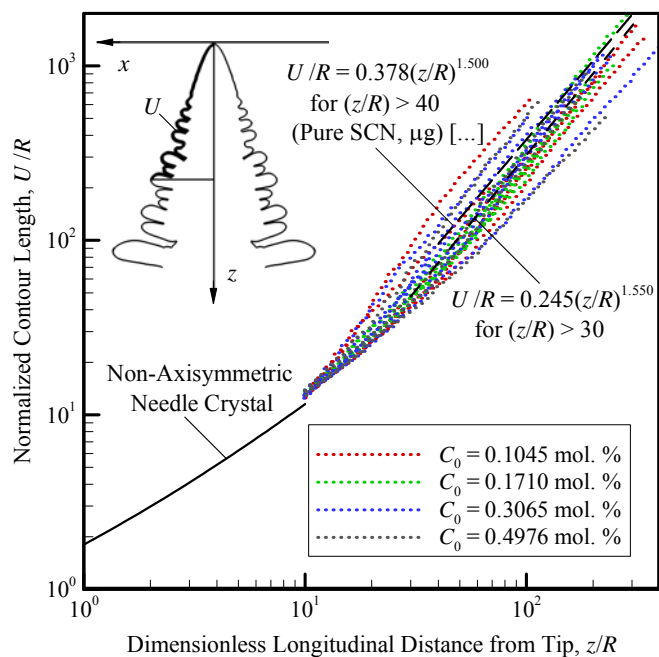
Figure 4.37: Contour length as a function of the longitudinal distance from tip for almost for SCN-Acetone alloys.
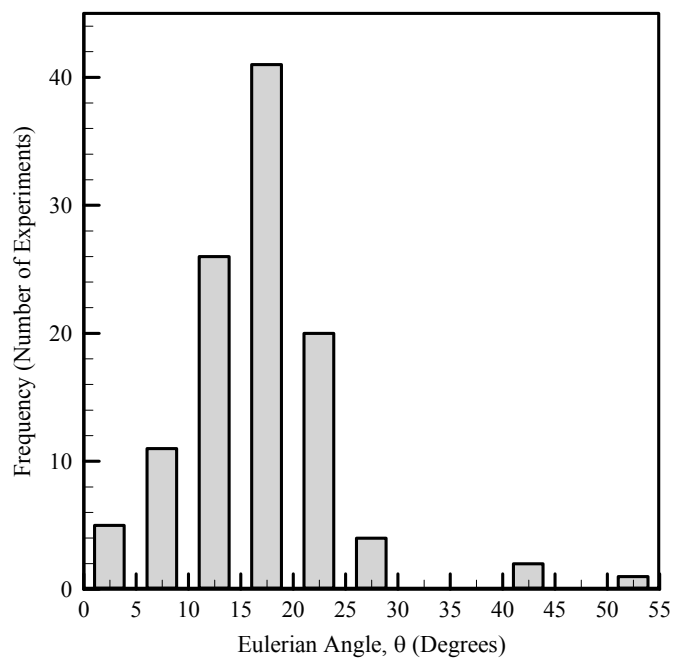
Figure 4.38: Histogram of the Eulerian angle (θ) for all dendrites studied.

CHAPTER V

CONCLUSIONS AND RECOMMENDATIONS

Current achievements of the present experimental investigation can be summarized as follows:

- A new experimental benchmark containing measurements of growth velocity, tip radius, Peclet number, selection parameter, and the coefficient A_4 for pure succinonitrile has been provided. The outstanding agreement observed between these measurements and the existing theoretical, numerical and experimental investigation of dendritic growth validates the experimental methodology proposed.

- A similar benchmark for succinonitrile-acetone alloys has been obtained. Results validate the transport portion of the model for free dendritic growth of succinonitrile-acetone alloys proposed by Li and Beckermann [78].

- Experiments provide accurate dendrite tip velocity and radius data for dilute SCN-acetone alloys. Tip velocity maximum at small solute concentration is verified by measurements.

- Tip growth Péclet number is well predicted by modified LGK model that accounts for thermosolutal convection (LB model [78]).

- The measurements of the selection parameter, σ^*, for pure succinonitrile exhibit an inverse dependence on the applied undercooling. This finding challenges the common assumption that the selection parameter is constant.

- In analogous fashion, the selection parameter for succinonitrile-acetone alloys shows a strong inverse dependence on the applied undercooling In addition, σ^* approaches value for pure SCN (0.02) at lo undercoolings.

Consequently, most selection criteria for alloys are questioned by this finding.

- Scaling relationships for the sidebranching shape were obtained for succinonitrile-acetone alloys in terms of the dendritic envelope, projection area and contour length. These new scaling relations agree well with previous measurements in pure succinonitrile dendrites by Li and Beckermann.

Experimental data for alloys with a higher concentration of acetone ($C_0 > 0.5 \, \text{mol.\%}$) would be very useful for validating phase field simulations. Such data can be obtained using the EDSE setup if the following improvements are carried out:

- Acquiring a monochrome progressive scan CCD camera with higher resolution in order to measure smaller dendrites resulting from experiments at bigger solute concentrations.

- Installing the cameras on new supports with a bigger range of motion. This improvement will increase the cameras field of view during the experiments.

- Installing more powerful thermo-electrical coolers in order to initiate the dendritic growth at higher solute concentrations.

- Designing and building a new support for the growth chamber that allows an easier alignment of the dentrite's ridges with the normal vector to the cameras' planes of view.

APPENDIX A

MELTING POINT MEASUREMENT

In order to measure the melting point of alloys, some solid must be created inside the chamber and melted away at the lowest temperature possible. The specific process employed is as follows:

- All the material in the chamber is completely melted by setting the bath temperature at 58.9°C.
- Then the bath temperature is set at the previous known melting point.
- Once the thermal equilibrium is reached, the solid is formed by cooling the chamber wall with water at room temperature. The solid is created by removing the growth chamber for the isothermal, rapidly submerging the bottom of the chamber in a Petri dish filled with water at room temperature, and returning the chamber to the isothermal bath. Using this technique a roughly semi-spherical layer of solid is obtained.
- The color video CCD camera is used to monitor the interface, which is traced on the TV screen with whiteboard marker to monitor its evolution.
- Next, the temperature in the chamber is decreased in 10 milli-Kelvin increments until the solid is observed to grow.
- Then, the bath temperature is then increased in 10 milli-Kelvin increments until it is observed that the solid begins to recede. After each modification of the bath temperature, the system is allowed to reach thermal equilibrium. Generally, a lapse of two hours is enough to ensure thermal equilibrium inside the growth chamber.
- If the entire solids melt away, then the current temperature setting exceeds the liquidus temperature and this process is started over. Otherwise, the

temperature is increased an additional 10 milli-Kelvin after the interface has become stable. This process is repeated until the level of solid in the chamber becomes very small (Figure A.1).

- At this point, the previous step is repeated but using increments of 3 milli-Kelvins.

- The temperature at which the last solid melts away corresponds to the liquidus temperature.
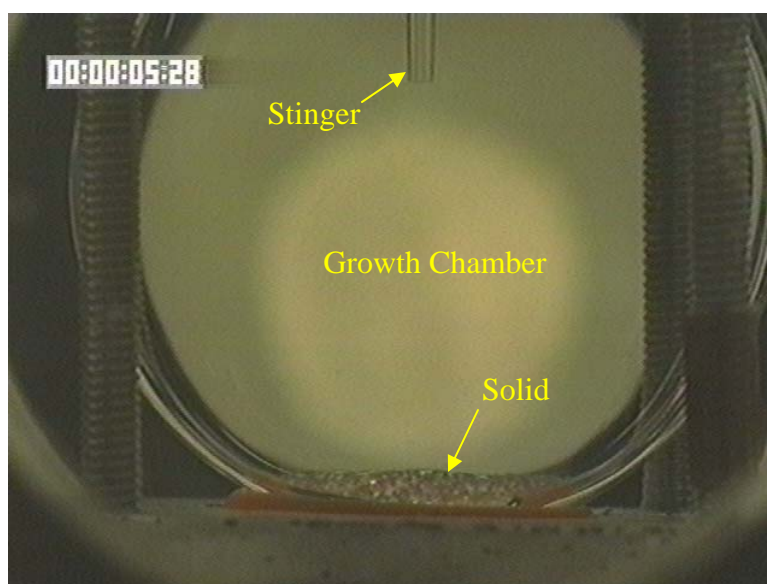
Figure A.1: Level of solid from which the temperature increments are reduced to 3 milli-Kelvins

REFERENCES

1. Algrem, R., Dai, W. and Hakim, V. 1993. Scaling behavior in anisotropic Hele-Shaw flow. *Physical Review Letters* **71** 3461-3464.

2. Asta, M., Beckermann, C., Karma, A., Kurz, W., Napolitano, R., Plapp, M., Purdy, G., Rappaz, M. and Trivedi, R. 2009. Solidification microstructure and solid-state parallels: recent developments, future directions. Acta Materialia 57 941-971.

3. Asta, M., Spaepens, F. and van der Ween, J. F. 2004. Solid-liquid interfaces: molecular structure, thermodynamics, and crystallization. *MRS Bulletin* **29** 920-926

4. Barbieri, A., Hong, D. and Langer, J. 1989. Velocity selection in the symmetric model of dendritic crystal growth. *Physical Review A* **39** 5314.

5. Barbieri, A. and Langer, J. 1989. Predictions of dendritic growth rates in the linearized solvability theory. *Physical Review A* **39** 5314-5325.

6. Beckermann, C., Diepers, H., Steinbach, I., Karma, A. and Tong, X. 1999. Modeling melt convection in phase-field simulations of solidification. *Journal of Computational Physics* **154** 468-496.

7. Beckermann, C., Li, Q. and Tong, X. 2001. Microstructure evolution in equiaxed dendritic growth. *Science and Technology of Advance Materials* **2** 117-126.

8. Ben-Amar, M. 1988. Theory of needle-crystal. *Physica D* **31** 409-423.

9. Ben-Amar, M. and Brener, E. 1993. Theory of pattern selection in three-dimensional nonaxisymmetric dendritic growth. *Physical Review Letters* **71** 589-592.

10. Ben-Amar, M. and Pelce, P. 1989. Impurity effect on dendritic growth. *Physical Review A* **39** 4263-4269.

11. Ben-Amar, M. and Pomeau, Y. 1986. Theory of dendritic growth in a weakly undercooled melt. *Europhysics Letter* **2** 307.

12. Ben-Jacob, E., Goldenfeld, N., Langer, J. and Schon, G. 1984. Boundary layer models of pattern formation in solidification. *Physical Review A* **29** 330.

13. Bilgram, J., Firmann, M. and Hurlimann, E. 1989. Dendritic solidification of Krypton and Xenon. *Journal of Crystal Growth* **96** 175.

14. Bisang, U. and Bilgram, J. 1996. Shape of tip and the formation of sidebranches of xenon dendrites. *Physical Review E* **54** 5309-5326.

15. Bisang, U. and Bilgram, J. 1995. Shape of the tip and formation of sidebranches of xenon dendrites. *Physical Review Letters* **21** 3898-3901.

16. Brener, E. 1996. Three-dimensional dendritic growth. *Journal of Crystal Growth* **166** 339-346.

17. Brener, E. 1993. Needle-crystal solution in three-dimensional dendritic growth. *Physical Review Letters* **71** 3653-3656.

18. Brener, E. and Melnikov, V. 1995. Velocity selection and instability spectrum in 3D dendritic growth. *JEPT* **80** 341-345.

19. Brener, E. and Melnikov, V. 1991. Pattern selection in two-dimensional dendritic growth. *Advances in Physics* **40** 53-97.

20. Brener, E. and Temkin, D. 1995. Noise-induced sidebranching in the three-dimensional nonaxisymmetric dendritic growth. *Physical Review E* **51** 351-359.

21. Caginalp, G. and Xie, W. 1993. Phase-field and sharp-interface alloy model. *Physical Review E* **48** 1897-1909.

22. Chan, S., Reimer, H. and Kahlweit, M. 1978. On the growth of NH4Cl dendrites at very low saturation. *Journal of Crystal Growth* **43** 229-234.

23. Chopra, M., Glicksman, M. and Singh, N. 1988. Dendritic solidification in binary alloys. *Metallurgical and Materials Transactions A* **19A** 3087-3096.

24. Collins, J. and Levine, H. 1985. Diffuse interface model of diffusion limited crystal growth. *Physical Review B* **31** 6119.

25. Conti, M. 1997. Growth of a needle crystal from an undercooled alloy melt. *Physical Review E* **56** 3197-3202.

26. Danan, F., Chen, L., Chen, S. and Voorhees, P. 1998. Phase field formulation for modeling the Ostwald ripening in two-phase systems. *Computational Material Science* **9** 329-336.

27. Dantzig, J. and Rappaz, M. 2008. *Solidification*. CRC Press.

28. Davis, S. 2001. *Theory of solidification*. Cambridge University Press.

29. Dougherty, A. and Chen, R. 1992. Coarsening and the mean shape of three-dimensional dendritic crystals. *Physical Review A* **46** 4508-4511.

30. Dougherty, A. and Gollub, J. 1988. Steady-state dendritic growth of NH4Br from solution. *Physical Review A* **38** 3043-3053.

31. Dougherty, A. and Gunawardana, A. 1994. Mean shape of three-dimensional dendrites: A comparison of pivalic acid and ammonium chloride. *Physical Review E* **50** 1349-1352.

32. Dougherty, A., Kaplan, P. and Gollub, J. 1987. Development of sidebranching in dendritic crystal growth. *Physical Review Letters* **58** 1652-1655.

33. Dougherty, A. and Lahiri, M. 2004. Shape of ammonium cloride dendrite tips at small supersaturation. *Journal of Crystal Growth* **274** 233-240.

34. Dougherty, A. and Nunnally, T. 2006. The transient growth of ammonium chloride dendrites. *Journal of Crystal Growth* **300** 467-472.

35. Draper, N. and Smith, H. 1998. *Applied regression analysis*. John Wiley & Sons, INC.

36. Elder, K., Drolet, F., Kosterlitz, J. and Grant, M. 1994. Stochastic eutectic growth. *Physical Review Letters* **72** 677.

37. Fix, G. 1983. A Fasano & M Primicerio, eds. *Free boundary problems: theory and applications*. Piman.

38. Giummarra, C., LaCombe, J., Koss, M., Frei, J., Lupulescu, A. and Glicksman, M. 2005. Sidebranch characteristics of pivalic acid dendrites grown under convection-free and diffuso-convective conditions. *Journal of Crystal Growth* **274** 317-330.

39. Glardon, R. and Kurz, W. 1981. Solidification path and phase diagram of directionally solidified Co-Sm-Cu alloys. *Journal of Crystal Growth* **51** 283-291.

40. Glicksman, M., Koss, M. and Winsa, E. 1994. Dendritic growth velocity in microgravity. *Physical Review Letters* **73** 573-576.

41. Glicksman, M. and Lupulescu, A. 2004. Dendritic crystal growth in pure materials. *Journal of Crystal Growth* **264** 541-549.

42. Glicksman, M. and Marsh, S. 1993. The dendrite. *Handbook of crystal growth* **1** 1077.

43. Glicksman, M., Schaefer, R. and Ayers, J. 1976. Dendritic growth- A test of theory. *Metallurgical Transactions A* **7** 1747.

44. Glicksman, M. and Singh, N. 1989. Effects of crystal-melt interfacial energy anisotropy on dendritic morfology and growth kinetics. *Journal of Crystal Growth* **98** 277-284.

45. Grossmann, B., Elder, K., Grant, M. and Kosterlitz, J. 1993. Directional solidification in 2-dimensions and 3-dimensions. *Physical Review Letters* **71** 3323.

46. Haxhimali, T. 2006. Phase-field simulation study of dendritic crystal growth morphologies for cubic and hexagonal symmetries: a dissertation. Doctoral dissertation, Northeastern University.

47. Horvay, G. and Cahn, J. 1961. Dendritic and spheroidal growth. *Acta Metallurgica* **9** 695-705.

48. Hoyt, J., Asta, M., Haxhimali, T., Karma, A., Napolitano, R., Trivedi, R., Laird, B. and Morris, J. 2004. Crystal-melt interfaces and solidification morphologies in metals and alloys. *MRS Bulletin* **29** 935-939.

49. Hoyt, J., Asta, M. and Karma, A. 2003. Atomistic and continuum modeling of dendritic solidification. *Materials Science and Engineering R* **41** 121-163.

50. Huang, S. and Glicksman, M. 1981. Fundamentals of dendritic solidification II. Development of sidebranch structure. *Acta Metallurgica* **29** 717-734.

51. Huang, S. and Glicksman, M. 1981. Fundamentals of dendritic solidification I. Steady-state tip growth. *Acta Metallurgica* **29** 701-715.

52. Hurlimann, E., Trittibach, R., Bisang, U. and Bilgram, J. 1992. Integral parameter of xenon dendrites. *Physical Review A* **46** 6579-6595.

53. Ivantsov, G. 1947. Temperature field around spherical, cylindrical and needle-shaped crystals which grow in supercooled melt. *Dokl. Akad. Nauk SSSR* **58** 567.

54. Kahlweit, M. 1970. On the dendritic growth of NH4Cl crystals from aqueous solutions. *Journal of Crystal Growth* **6** 125-129.

55. Karma, A. 2001. Phase-field formulation for quantitative modeling of alloy solidification. *Physical Reviews Letters* **87** 115701/1.

56. Karma, A. 1994. Phase-field model of eutectic growth. *Physical Reviews E* **49** 2245.

57. Karma, A. and Kotliar, B. 1985. Pattern selection in a boundary layer model of dendritic growth in the presence of impurities. *Physical Review A* **31** 3266.

58. Karma, A., Lee, Y. and Plapp, M. 2000. Three-dimensional dendrite-tip morphology at low undercooling. *Physical Review E* **61** 3996-4006.

59. Karma, A. and Rappel, W. 1998. Quantitative phase-field modeling of dendritic growth in two and three dimensions. *Physical Review E* **57** 4323-4349.

60. Karma, A. and Rappel, W. 1997. Phase field simulation of three-dimensional dendrites: is microscopic solvability theory correct?. *Journal of Crystal Growth* **174** 54-64.

61. Karma, A. and Rappel, W. 1996. Phase-field method for computationally efficient modeling of solidification witn arbitrary interface kinetics. *Physical Review E* **53** R3017-R3020.

62. Kessler, D., Koplik, J. and Levine, H. 1988. Pattern selection in fingered growth phenomena. *Advances in Physics* **37** 255-399.

63. Kessler, D. and Levine, H. 1988. Pattern selection in the three dimesional dendritic growth. *Acta Metallurgica* **36** 2693.

64. Kessler, D. and Levine, H. 1986. Velocity selection in dendritic growth. *Physical Review B* **33** 7867-7870.

65. Kim, S., Kim, W. and Suzuki, T. 1999. Phase-field model for binary alloys. *Physical Review E* **60** 7186-7197.

66. Kim, Y., Provatas, N., Goldenfeld, N. and Dantzig, J. 1999. Universal dynamics of phase-field models for dendritic growth. *Physical Review E* **59** 2546-2549.

67. Kobayashi, R. 1993. Modeling and numerical simulation of dendritic growth. *Physica D* **63** 410.

68. Koss, M., Bushnell, L., LaCombe, J. and Glicksman, M. 1996. The effect of convection on dendritic growth under microgravity conditions. *Chemical Engineering Communications* **152-153** 351-363.

69. Koss, M., LaCombe, J., Tennenhouse, L., Glicksman, M. and Winsa, E. 1999. Dendritic growth tip velocities and radii of curvature in microgravity. *Metallurgical and Materials Transactions A* **30A** 3177-3190.

70. Kraft, T., Roosz, A. and Rettenmayr, M. 1996. Undercooling effects in microsegregation modelling. *Scripta materialia* **35** 77-82.

71. Kurz, W. 1989. D Fisher, eds. *Fundamentals of solidification*. Trans Tech Publications.

72. LaCombe, J., Koss, M., Corrigan, D., Lupulescu, A., Tennenhouse, L. and Glicksman, M. 1999. Implications of the interface shapeon steady-state dendritic crystal growth. *Journal of Crystal Growth* **206** 331-344.

73. LaCombe, J., Koss, M., Fradkov, V. and Glicksman, M. 1995. Three-dimensional dendrite-tip morphology. *Physical Review E* **52** 2778-2786.

74. LaCombe, J., Koss, M., Frei, J., Giummarra, C., Lupulescu, A. and Glicksman, M. 2002. Evidence for tip velocity oscillations in dendritic solidification. *Physical Review E* **65** 031604-1.

75. LaCombe, J., Koss, M. and Glicksman, M. 2007. Tip velocities and radii of curvature of pivalic acid dendrites under convection-free conditions. *Metallurgical and Materials Transactions A* **38A** 116-126.

76. Lan, C., Chang, Y. and Shih, D. 2003. Adaptative phase field phase field simulation of non-isothermal free dendritic growth of a binary alloy. *Acta Materalia* **51** 1857-1869.

77. Lan, C. and Shih, C. 2004. Phase-field simulation of non-isothermal free dendritic growth of a binary alloy in a force flow. *Journal of Crystal Growth* **264** 472-482.

78. Langer, J. 1989. Dendrites, viscous fingers and the theory of pattern formation. *Science* **243** 1150.

79. Langer, J. 1987. J Souletie, J Vannimenus & R Stora, eds. *Chance and matter*. North-Holland.

80. Langer, J. 1980. Instabilities and pattern formation in crystal growth. *Reviews of Modern Physics* **52** 1-28.

81. Langer, J. and Muller-Krumbhaar, H. 1978. Theory of dendritic growth I. Elements of stability analysis. *Acta Metallurgica* **26** 1861-1687.

82. Langer, J. and Muller-Krumbhaar, H. 1978. Theory of dendritic growth II. Instabilities in the limit of vanishing surface tension. *Acta Metallurgica* **26** 1689-1695.

83. Langer, J. and Muller-Krumbhaar, H. 1978. Theory of dendritic growth III. Effects of surface tension. *Acta Metallurgica* **26** 1697-1708.

84. Li, Q. and Beckermann, C. 2002. Modelling of free dendritic growth of succinonitrile-acetone alloys with thermosolutal melt convection. *Journal of Crystal Growth* **236** 482-498.

85. Li, Q. and Beckermann, C. 1999. Evolution of the sidebranch structure in free dendritic growth. *Acta Materalia* **47** 2345-2356.

86. Li, Q. and Beckermann, C. 1998. Scaling behavior of the three-dimensional dendrites. *Physical Review E* **57** 3176-3188.

87. Lipton, J., Glicksman, M. and Kurz, W. 1987. Equiaxed dendrite growth in alloys at small supercooling. *Metallurgical Transactions A* **18A** 341-345.

88. Lipton, J., Glicksman, M. and Kurz, W. 1984. Dendritic growth in undercooled alloys melts. *Material Science and Engineering* **65** 57-63.

89. Lipton, J., Kurz, W. and Trivedi, R. 1987. Rapid dendritic growth in undercooled alloys. *Acta Metallurgica* **35** 957-964.

90. Liu, S., Li, J., Lee, J. and Trivedi, R. 2006. Spatio-temporal microstructure evolution in directional solidification processes. *Phylosophical Magazine* **86** 3717-3738.

91. Longinova, I., Amberg, G. and Agren, J. 2001. Phase-field simulation of non-isothermal binary alloy solidification. *Acta Materalia* **49** 573-581.

92. Lu, Y., Beckermann, C. and Ramirez, J. 2005. Three-dimensional phase-field simulations of the effect of convection on free dendritic growth. *Journal of Crystal Growth* **280** 320-334.

93. Maurer, J., Perrin, B. and Tabeling, P. 1991. Three-dimensional structure of NH4Br dendrites growing within a gel. *Europhysics Letters* **14** 575-579.

94. Meiron, D. 1986. Selection of steady state in two-dimensional symmetric model of dendritic growth. *Physical Review A* **33** 2704.

95. Mullins, W. and Sekerka, R. 1964. Stability of a planar interface during solidification of a dilute binary alloy. *Journal of Applied Physics* **35** 444.

96. Muschol, M., Liu, D. and Cummins, H. 1992. Surface-tension-anisotropy measurements of succinonitrile and pivalic acid: Comparison with microscopic solvability theory. *Physical Review A* **46** 1038-1050.

97. Napolitano, R. and Liu, S. 2004. Three-dimensional crystal-melt Wulff-shape and interfacial stiffness in the Al-Sn binary system. *Physical Review B* **70** 214103.

98. Napolitano, R., Liu, S. and Trivedi, R. 2002. Experimental measurement of anisotropy in crystal-melt interfacial energy. Interface Science 10 217-232.

99. Papapetrou, A. 1935. Investigations on the dendrite growth of crystals. *ZEITSCHRIFT FUR KRISTALLOGRAPHIE* **92** 89-129.

100. Pines, W., Chait, A., Zlatkowski, M. and Beckermann, C. 1999. Equiaxed dendritic solidification in supercooled melts. *Journal of Crystal Growth* **197** 355-363.

101. Provatas, N., Goldenfeld, N., Dantzig, J., LaCombe, J., Lupulescu, A., Koss, M., Glicksman, M. and Algrem, R. 1999. Crossover scaling in dendritic evolution at low undercooling. *Physical Review Letters* **82** 4496-4499.

102. Provatas, N., Goldenfeld, N. and Dantzig, J. 1998. Efficient computation of dendritic microstructure using adaptative mesh refinement. *Physical Review Letters* **80** 3308.

103. Ramirez, J. and Beckermann, C. 2005. Examination of binary alloy free dendritic growth theories with phase field model. *Acta Materalia* **53** 1721-1736.

104. Rebow, M. and Browne, D. 2007. On dendritic tip stability parameter for aluminium alloy solidification. *Scripta Materalia* **56** 481-484.

105. Rubinstein, E. and Glicksmann, M. 1991. Dendritic grown kinetics and structure I. Pivalic acid. *Journal of Crystal Growth* **112** 84-96.

106. Saito, Y., Goldbeck-Wood, G. and Muller-Krumbhaar, H. 1988. Numerical simulation of dendritic growth. *Physical Review A* **38** 2148-2157.

107. Sekerka, R., Coriell, S. and McFadden, G. 1995. Stagnant film model of the effect of natural convection on the dendrite operation state. *Journal of Crystal Growth* **154** 370.

108. Sinha, A. 2003. *Physical metallurgy handbook*. McGraw-Hill.

109. Stefanescu, D. 1995. Methodologies for modeling of solidification microstructure and their capabilities. *ISIJ International* **35** 637-650.

110. Steinbach, I., Beckermann, C., Kauerauf, B., Li, Q. and Guo, J. 1999. Three-dimensional modeling of equiaxed dendritic growth on a mesoscopic scale. *Acta Materialia* **47** 971-982.

111. Suzuki, T., Ode, M., Kim, S. and Kim, W. 2002. Phase-field model of dendritic growth. *Journal of Crystal Growth* **237-239** 125.

112. Tennenhouse, L., Koss, M., LaCombe, J. and Glicksman, M. 1997. Use of microgavity to interpret dendritic growth kinetics at small supercoolings. *Journal of Crystal Growth* **174** 82-89.

113. Tiaden, J., Nestler, B., Diepers, H. and Steinbach, I. 1998. The multiphase-field model with integrated concept for modeling solute diffusion. *Physica D* **115** 73.

114. Tong, X. and Beckermann, C. 1998. A diffusion boundary layer model of microsegregation. *Journal of Crystal Growth* **187** 289-302.

115. Tong, X. and Beckermann, C. 1998. Integral solutions of diffusion-controlled dendrite tip growth. *International Journal of Heat and Mass Transfer* **41** 4025-4029.

116. Trivedi, R. 1970. Growth of dendritic needles from a undercooled melt. *Acta Metallurgica* **18** 287-296.

117. Trivedi, R. 1969. On the growth of dendritic plates. *Scripta Metallurgica* **3** 613-618.

118. Trivedi, R. and Kurz, W. 1994. Dendritic Growth. *International Materials Reviews* **39** 49-79.

119. Trivedi, R. and Mason, J. 1991. The effects of interface attachment kinetics on solidification morphologies. *Metallurgical Transactions A* **22** 235.

120. Udaykumar, H., Mao, L. and Mittal, R. 2002. A finite-volume sharp interface scheme for dendritic growth simulations: Comparison with microscopic solvability theory. *Numerical Heat Transfer Part B-Fundamentals* **42** 389-409.

121. Warren, J. and Boettinger, W. 1995. Prediction of dendritic growth and microsegregation patterns in a binary alloy using phase-field method. *Acta Metallurgica et Materalia* **a43** 689.

122. Wheeler, A., Boettinger, J. and McFadden, G. 1992. Phase-field model for isothermal phase transitions in binary alloys. *Physical Review A* **45** 7424-7439.

123. Wheeler, A., Boettinger, W. and McFadden, G. 1993. Phase-field model of solute trapping during solidification. *Physical Review E* **47** 1893.

124. Xu, J. and Yu, D. 2001. Futher examinations of dendritic growth theories. *Journal of Crystal Growth* **222** 399-413.

125. Yang, Y. and Udaykumar, H. 2005. Sharp interface Cartesian grid method III: Solidification of pure materials and binary solutions. *Journal of Computational Physics* **210** 55-74.